CHALMERS

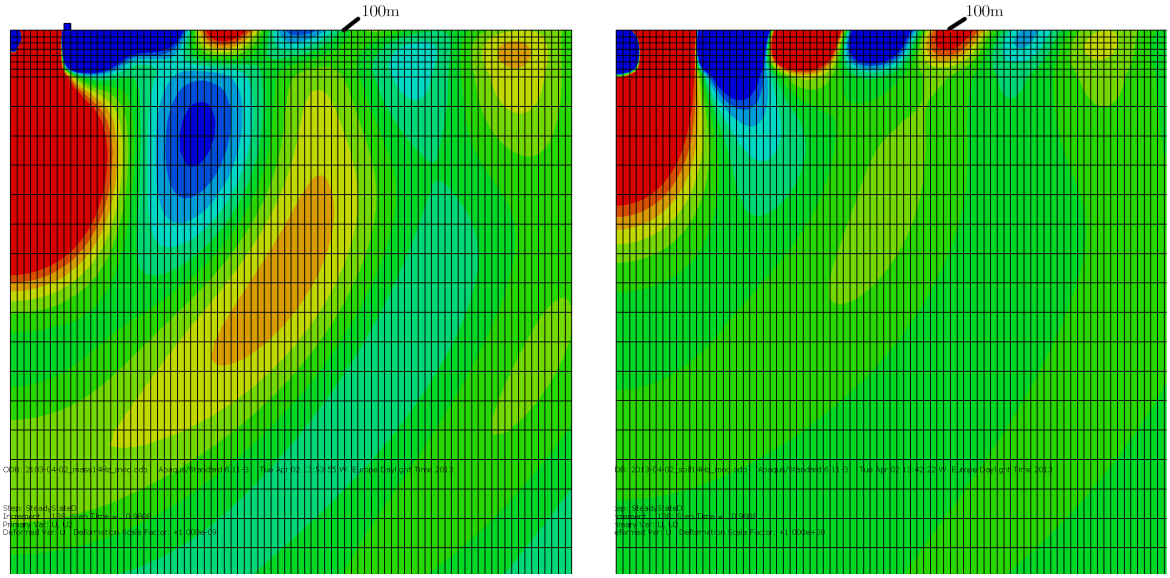

Vibration reduction in soil through the use of buildings at the synchrotron radiation facility MAX-IV

Master's thesis in Architecture and Engineering

VEDAD ALIC

Department of Applied Mechanics
Division of Dynamics
CHALMERS UNIVERSITY OF TECHNOLOGY
Göteborg, Sweden 2013
Master's thesis 2013:09

MASTER'S THESIS IN ARCHITECTURE AND ENGINEERING

Vibration reduction in soil through the use of buildings at the synchrotron radiation facility MAX-IV

VEDAD ALIC

Department of Applied Mechanics
Division of Dynamics
CHALMERS UNIVERSITY OF TECHNOLOGY

Göteborg, Sweden 2013

Vibration reduction in soil through the use of buildings at the synchrotron radiation facility MAX-IV
VEDAD ALIC

© VEDAD ALIC, 2013

Master's thesis 2013:09
ISSN 1652-8557
Department of Applied Mechanics
Division of Dynamics
Chalmers University of Technology
SE-412 96 Göteborg
Sweden
Telephone: +46 (0)31-772 1000

Cover:
Vertical displacement amplitude of (left) soil model with building(mass) $\rho = 8271\text{kg/m}^3$ and (right) model with no mass, for a prescribed harmonic load with excitation frequency 14Hz and unit amplitude applied at $t = 0$. Figure displays snapshot at $t = 0.98$s. Close up showing approximately 150 by 150 meters of the models.

Chalmers Reproservice
Göteborg, Sweden 2013

Vibration reduction in soil through the use of buildings at the synchrotron radiation facility MAX-IV
Master's thesis in Architecture and Engineering
VEDAD ALIC
Department of Applied Mechanics
Division of Dynamics
Chalmers University of Technology

Abstract

MAX-lab is a synchrotron facility operated jointly by the Swedish Research Council (VR) and Lund University. Currently the project consists of three storage rings, MAX I-III, and construction has begun on a fourth. The new facility, MAX-IV will be located northeast of Lund, at the outskirt of a new area called Brunnshög, roughly 100 meters southeast of the highway E-22. The instruments that are operating on nano-level scale at MAX-IV are extremely sensitive to vibrations. With the facility located closely to the highway and on top of very soft soil measures have had to be taken to ensure good operation of the facility. The measures include stabilization of the soil underneath the facility (stiffening), and the shaping of the ground around the facility in a way that will mitigate vibrations.

The aim of this master's thesis is to investigate if placing out masses/buildings in between the vibration source and MAX-lab can decrease ground vibrations. The idea is based on a previous master thesis in Architecture where part of the objective was to find out in an early design stage what sort of organization of buildings/masses that can work to mitigate vibrations. The work has been carried out using finite element analysis in two (axisymmetric), and three dimensions. Steady state models in the frequency range 5-30Hz have been established with main evaluation points 100 meters from the load, with masses placed in between. Soil as a material is generally treated as highly non-linear and inhomogeneous, however, with the present low magnitude loading and short wavelengths in comparison to soil particles, it is here reasonable to treat soil as a homogeneous linear viscoelastic material.

Two-dimensional results indicate that masses on the ground can be used as a means to mitigate ground vibration, but in order for them to be effective they need to be very heavy. However, due to the nature of being effective around the mass-soil systems resonance frequency they can instead lead to larger vibrations in the soil, if they are excited at frequencies close to their resonant frequencies. With insight from the 2D simulations the 3D simulations attempt to find spatial organizations for masses between vibration source and the facility. In order to carry out parameter tests in the 3D-model an effective reduction method was designed and implemented. The reduction method is based on Guyan reduction and domain decomposition. After having reduced the model from about 2.5 million degrees of freedom to about 12 thousand, different organizations of masses were assembled on top of the reduced ground model and steady state analysis was performed in the frequency range between 5-29Hz. Three-dimensional results show that locating masses in a careful manner can work for vibration mitigation, and combining masses of different densities has further effect that reduction in a wider frequency range can be reached.

Keywords: Soil vibration, Blocking masses and buildings, Vibration reduction, Multi-level dynamic reduction

Preface

The master's thesis of 30 credits has been carried out during the long winter of 2012/2013, and also marks the end of my studies in Architecture and Engineering at Chalmers University of Technology, it is the second of two theses, where the first was in Architecture. Most of the time during the work was spent at the Department of Construction Sciences, Division of Structural Mechanics, at Lund University, where I got this great opportunity.

The main supervisor was Ph.D. Kent Persson, Division of Stuctural Mechanics, Lund University. At Chalmers University of Technology Ph.D. Mikael Enelund has been the examiner for the thesis.

Acknowledgements

I would like to thank my supervisor Kent Persson and my examiner Mikael Enelund for their support during the thesis work.

Many thanks to the staff at the Division of Structual Mechanics, Lund University, who have helped me with ideas for the thesis, and with performing some initial physical model tests.

Nomenclature

Roman symbols

P	Primary(pressure) wave
R	Rayleigh wave
S	Secondary(shear) wave
$_{m,\ s}$	Subscripts for master and slave dofs
$a = \ddot{u}$	Acceleration
c	Viscous damping constant
c_{P}	P-wave phase velocity
c_{R}	R-wave phase velocity
c_{S}	S-wave phase velocity
E	Young's modulus
F	Force
F_{D}	Damping force
F_{S}	Spring force
G	Shear modulus
g	Gravity
h_{mass}	Height of mass
L	Length
m	Mass
p	External force
r, z	Axisymmetric coordinates
t	Time
u	Displacement
u_{st}	Static displacement
$v = \dot{u}$	Velocity
w_{mass}	Width of mass
x, y, z	Cartesian coordinates

Roman bold symbols

$\mathbf{C}$	Damping matrix
$\mathbf{C}_{\mathrm{r}}$	Reduced damping matrix
$\mathbf{D}$	Dynamic stiffness matrix
$\mathbf{D}_{\mathrm{r}}$	Reduced dynamic stiffness matrix
$\mathbf{f}$	Nodal force vector
$\mathbf{K}$	Stiffness matrix
$\mathbf{K}_{\mathrm{r}}$	Reduced stiffness matrix
$\mathbf{M}$	Mass matrix
$\mathbf{M}_{\mathrm{r}}$	Reduced mass matrix
$\mathbf{T}$	Transformation matrix
$\mathbf{u}$	Nodal displacement vector

Greek symbols

α, β	Rayleigh damping parameters

γ	Structural damping factor
λ	Wavelength
ν	Poisson's ratio
Ω	Excitation frequency
ω	Angular frequency
ω_n	Natural frequency
ρ	Density
ζ	Damping ratio
ζ_{eq}	Equivalent viscous damping ratio

Contents

1 Introduction

1.1 Background

MAX-lab (Mictrotron Accelerator for X-rays) is a national laboratory in Lund, which is operated jointly by the Swedish Research Council (VR) and Lund University. Currently the project consists of three storage rings, MAX I-III, and a fourth ring being built, MAX-IV. [10]

The principle of operation for a synchrotron is such that synchrotrons are unable to accelerate particles from zero kinetic energy and instead rely on pre-accelerated particles from another source, like a linear accelerator (linac) which accelerates the particles to near-light speed. Once the particles enter the synchrotron they are forced into a circular course by strong magnets. When the particles are accelerated they send out synchrotron light. The synchrotron light that is emitted is then used in research in beam lines which are installed tangentially to the synchrotron storage ring. For good results it is important to have a very intense and well-focused synchrotron light with a small radiation size, which is achieved by making sure that the beam in the storage ring has a small size and low angular proliferation, which, in turn, is achieved by making sure that the storage ring has low emittance.

Max-II is the largest of the current storage rings, with a circumference of 90 meters. Max-III was added in 2007 with the purpose to unburden Max-II for synchrotron light research in the ultraviolet area.

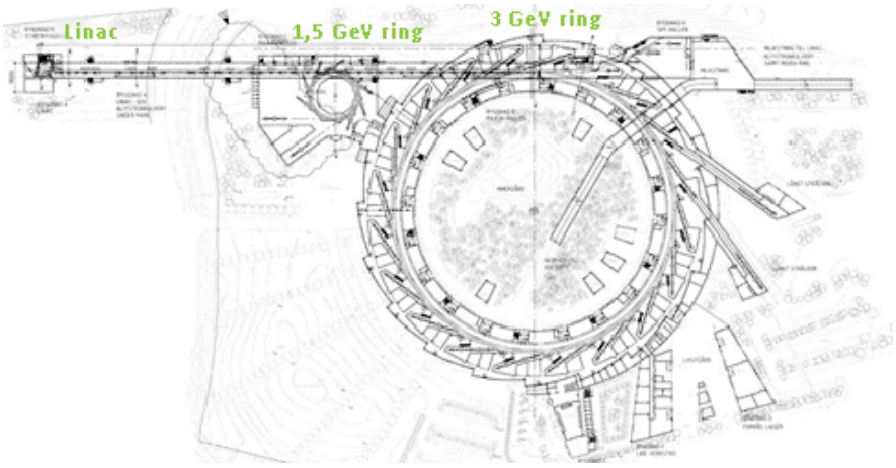

Figure 1.1: *Draft of Max-IV [10]*

There is now a need to upgrade the research abilities at MAX-lab, and a new facility, Max-IV is being built. With an electron pre-accelerator, a 250 meter long linac, two storage rings of 96 and 528 meters circumference, as seen in Figure 1.1. Max-IV will be able of a 3-GeV energy level in the largest storage ring with low emittance for the production of soft and hard x-rays as well as an expansion into the free electron laser field. It is being built at Brunnshög, part of Lund North-East, a new development area for which MAXLAB together with ESS (European Spallation Source, another material research facility planned for around 2020) act as development catalysts.

Amongst the disciplines that will benefit from research at Max-IV are material sciences, energy research, biogeochemistry, atmospheric chemistry, corrosion chemistry, nanotechnology, catalysis research, environmental sciences, cultural heritage, and basic physics and chemistry.

The location of MAX-IV is about 100 meters south-east of the highway E22, and about 100 meters north-west of Odarslövsvägen running parallel to the E22, see Figure 1.2 (a). The placement is intentional as it is both close to the new part of town as well as being able to give a good image of Lund to passers by. The highway and Odarslövsvägen might lead to vibration issues for which MAX-IV is very sensitive to (vertical displacements limit of 26nm RMS during one second, for frequencies above 5 Hz and below 100 Hz). Further on the municipality plans to build a tramway another hundred meters south-east of Odarslövsvägen, that also may increase the vibrations in the facility.

1.1.1 Architectural thesis

Prior experience has shown us that separation of functions in urban planning may not be such a great idea. Mixed use zoning has once again become popular due to benefits such as reduced distances between housing, workplaces and retail, more compact development, and a more lively urban fabric, as the office sleeps the living room is awake meaning the mixed used zone has more potential as an active place. This thesis, or set of theses consider two aspects of that idea. The first thesis was done during the spring 2012 at Chalmers University of Technology, at the department of Architecture [1]. In that thesis the area around the new research facility Max-IV, part of MAXLAB was studied and a proposal was done with the ambition to try to incorporate Max-IV closer into the city of Lund. Building a bit on the mixed use idea the citizens of Lund living nearby MAX-IV would be exposed to a pool of knowledge, but in what way could MAX-IV benefit from the proximity? One thought during the Architectural thesis was that the buildings could potentially help Max-IV perform better if they could reduce the incoming vibrations from surrounding traffic.

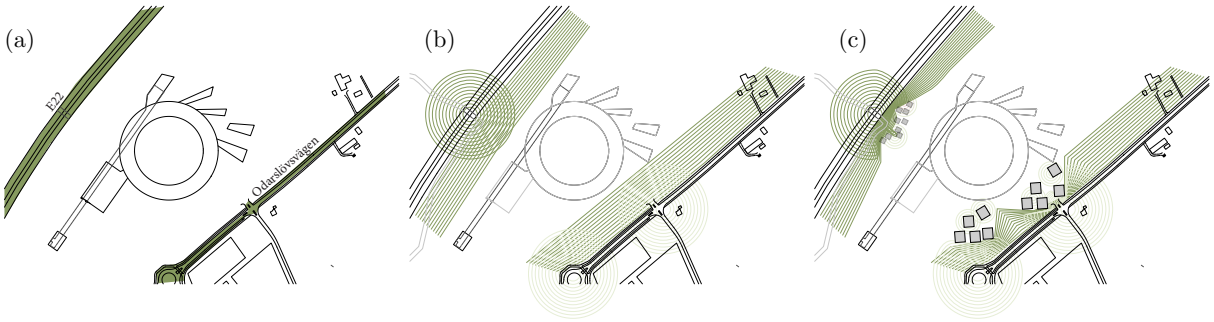

Figure 1.2: *Vibrations from roads, reduced by buildings*

The architectural thesis built up an urban design (see Figure 1.3 (c)) from solutions that worked well in a digital Ripple Tank Simulator [12] as well as some physical experiments with scale models using JELL-O as soil and placing out masses on top as buildings. Although working for its intended use the Ripple Tank experiments are not entirely true to the wave propagation trough a solid medium. This thesis will investigate if the proposed solutions from the architectural thesis might work, and if there are some solutions which work better than others, in essence create a *Ripple Tank Simulator*, but for waves in elastic media, and try out a set of different solutions.

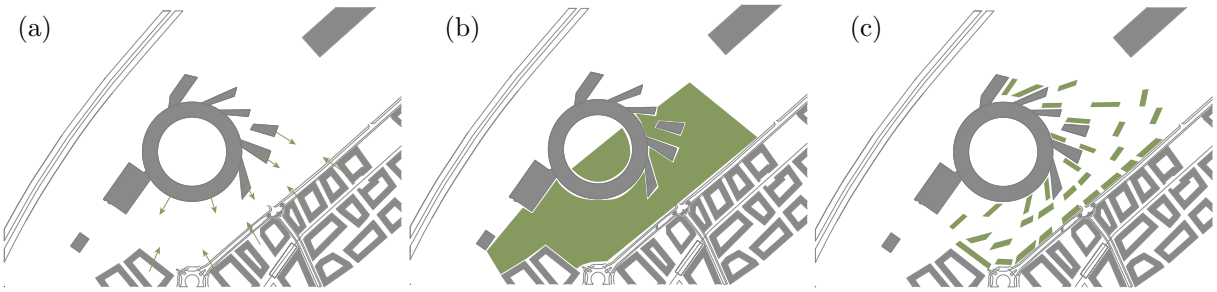

Figure 1.3: *Building closer to MAX-IV*

1.1.2 Methods for mitigating vibrations

Issues with ground vibrations are expected to rise due to predicted increases in urban populations and the following increases in traffic necessary for transportation. As cities become denser, vibrations from trains and road vehicles will have to be dealt with. Mitigation of ground vibrations is traditionally done by methods such as digging a trench between the vibration source and the facility which should be protected, or by adding barriers in the soil such as sheet piles/buried walls or some sort of stiffening of the soil, or wave impeding blocks. Other options exist, such as shaping the ground terrain, which has been done at Max-IV. There is ongoing theoretical research about mechanical invisibility cloaks [7], which may potentially be used to guide

surface waves around sensitive objects.

Resonant mass scatterers, though at the time not referred as such, have been considered as a viable method of mitigation both theoretically [8] [13] [4], and numerically [5]. Petyt and Jones [5] consider at an evaluation point 25 meters from the load, in between which they place different sets of heavy masses and come to the conclusion that the effectiveness varies critically on the location of the masses relative to the load and evaluation points, on the size of the masses and on the most sensitive frequency range of the system. In general a heavy mass close to the load works best for their situation. Krylov [8] shows (for a 2D model) analytically that only 10% of the incoming wave energy is transmitted past a lumped mass around its resonant frequency, the rest of it is either reflected back or propagated as body waves trough the half-space medium. The solution should be taken as a very rough estimate as it is derived for a lumped mass and does not take into account the mass moment of inertia. Most importantly for the MAX-lab site is, that it needs a *mass - soil - infinite bedrock* model and not just *mass - infinite soil* model, where in the former reflections may occur between different soil layers or between the soil and bedrock layer, drastically complicating the solution.

1.2 Objective and method

The objective of this thesis is to study the effects of placing masses or buildings in between a vibration source and an evaluation point at which the vibration levels were evaluated.

The study has been performed numerically using the finite element method (FEM) both in 2D and in 3D. Specifics for material data and distances have been based on values from the Max-IV site. The 2D studies have focused primarily on the effects of a few parameters such as the density, size, and position of the mass/building. The 3D studies have based the material parameters on the results of the 2D studies, and further looked into the effect of different spatial organizations of masses/buildings. Focus has been on studying relative improvements instead of absolute values. Parts of the architectural thesis plan were evaluated in the study as well.

Physical models were investigated as an option to 3D FEM simulations, but were disregarded due to inability to find suitable scale materials.

In essence, advanced simulation and physical experiments were used as sketching tools for preliminary architectural design, where architecture and engineering inform each other.

1.3 Outline of the report

- The first chapter is an introduction to the report. It covers MAXLAB as a site for investigation, the architectural master thesis that was done in a previous study, some previous work about the potential use of masses as Rayleigh wave scatterers and other methods of wave mitigation.
- Chapter 2 briefly covers vibration theory, the finite element method, wave propagation in semi-infinite spaces, and soil materials.
- Chapter 3 describes the 2D-axisymmetric and 3D finite element models, as well as the physical scale model.
- Chapter 4 presents the results of the different studies.
- Chapter 5 covers discussion, final conclusions and suggestions for further work.

2 Theory

2.1 Vibration theory

2.1.1 Introduction

The analysis and design of structures subject to time dependent forces constitute the field of structural dynamics. For example a bridge oscillating to forces from the wind or passing traffic, or as another case a building being disturbed by an earthquake are examples of where one must consider the dynamics. Many phenomena associated

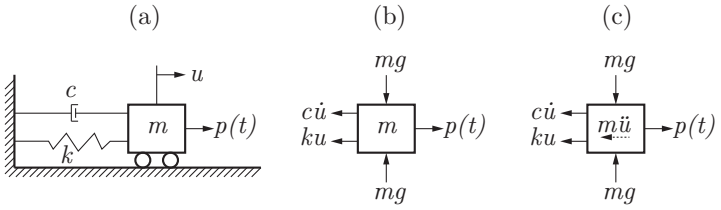

Figure 2.1: *Single degree of freedom (SDOF) model*

with complicated systems can be understood by studying more simple systems. The simplest of such systems is a single degree of freedom (SDOF) model, meaning that only one independent quantity must be specified in order to uniquely define the position of the system, this quantity may be a Cartesian co-ordinate (x, y, z). The model consists of a single lumped mass m, a spring with stiffness k, and a dashpot with damping c. Consider the system shown in Figure 2.1, Newton's second law for a constant mass system states that

$$\sum F = ma = m\ddot{u} \tag{2.1}$$

In the considered case from the free-body diagram three forces are identified which are acting on the mass, the external force $p(t)$, the spring force F_S positive towards the static equilibrium position (where the spring is neither extended nor compressed) and the damping force F_D acting opposite the direction of movement.

$$\sum F = p(t) - F_{\mathrm{S}} - F_{\mathrm{D}} \tag{2.2}$$

using Hooke's law for the spring

$$F_{\mathrm{S}} = k\Delta L \tag{2.3}$$

and for the dashpot with damping proportional to the velocity

$$F_{\mathrm{D}} = c\Delta\dot{L} \tag{2.4}$$

where

$$\Delta L = u_2 - u_1 \tag{2.5}$$

using

$$u_1 = 0, u_2 = u \tag{2.6}$$

and Newton's second law in Equation 2.2 we finally get the second order ordinary differential equation

$$m\ddot{u}(t) + c\dot{u}(t) + ku(t) = p(t) \tag{2.7}$$

which is known as the equation of motion for a single degree of freedom system, describing the vibrations of the mass-dashpot-spring system around its equilibrium position under the load $p(t)$.

2.1.2 MDOF systems

In order to describe more complicated systems and additional phenomena it is necessary to extend the theory to multiple degree of freedom (MDOF) systems. The simplest of such systems is one with two degrees of freedom, seen in Figure 2.2 with degree of freedom u_1 and u_2. Using Newton's second law for each mass we get a system

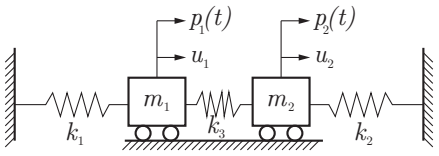

Figure 2.2: *Two degree of freedom (2DOF) model*

with two coupled equations of motion

$$\begin{array}{rcl} m_1\ddot{u}_1 & = & p_1(t) + F_{\mathrm{S1}-1} + F_{\mathrm{S3}-1} \\ m_2\ddot{u}_2 & = & p_2(t) + F_{\mathrm{S2}-2} + F_{\mathrm{S3}-2} \end{array} \tag{2.8}$$

in which the spring forces first index denotes the spring and the second index denotes the mass which the spring-force is imposed on. Using Hooke's law and substituting into 2.8 we get

$$\begin{array}{rcl} m_1\ddot{u}_1 + k_1u_1 + k_3(u_1 - u_2) & = & p_1 \\ m_2\ddot{u}_2 + k_2u_2 + k_3(u_2 - u_1) & = & p_2 \end{array} \tag{2.9}$$

which may be written in matrix form

$$\mathbf{M}\ddot{\mathbf{u}} + \mathbf{K}\mathbf{u} = \mathbf{F} \tag{2.10}$$

where $\mathbf{u} = (u_1, u_2)^T$ and $\mathbf{F} = (p_1, p_2)^T$ are the displacement and force vectors and

$$\mathbf{M} = \begin{bmatrix} m_1 & 0 \\ 0 & m_2 \end{bmatrix}, \mathbf{K} = \begin{bmatrix} k_1 + k_3 & -k_3 \\ -k_3 & k_2 + k_3 \end{bmatrix} \tag{2.11}$$

are the mass and stiffness matrix. If damping is present the $\mathbf{C}$ matrix is derived in a similar way and Equation 2.10 would get a $\mathbf{C}\dot{\mathbf{u}}$ term on the left hand side, becoming

$$\mathbf{M}\ddot{\mathbf{u}} + \mathbf{C}\dot{\mathbf{u}} + \mathbf{K}\mathbf{u} = \mathbf{F} \tag{2.12}$$

The derivation of more than two degrees of freedom system is analogous, but setting up the equations for all parts and keeping track of positive directions can easily lead to human induced errors. Instead it is preferable to use Lagrange's equations with generalized coordinates, see [3].

2.1.3 Resonance

Consider the undamped version of the equation of motion for a single degree of freedom model, as in Equation 2.7, subject to forced motion. The total response of a linear system consists of a forced motion and a natural motion, and in the case of harmonic excitations the forced motion is referred to as the *steady-state response*. The equation of motion is

$$m\ddot{u} + ku = p_0 \cos \Omega t \tag{2.13}$$

From the fact that only even-order derivatives appear on the left hand side of Equation 2.13 it is possible to assume a solution of the following form for the steady state response

$$u_p = U \cos \Omega t \tag{2.14}$$

substituting Equation 2.14 into 2.13 and solving for the amplitude U of the steady state response we get

$$U = \frac{p_0}{k - m\Omega^2} \tag{2.15}$$

using the static displacement

$$U_0 = \frac{p_0}{k} \tag{2.16}$$

one may write Equation 2.15 as the nondimensionalized frequency-response function

$$\frac{U}{U_0} = \frac{1}{1 - (\frac{\Omega}{\omega_n})^2} \tag{2.17}$$

where $\omega_n = \sqrt{\frac{k}{m}}$ is the natural frequency of the SDOF system and Equation 2.15 holds as long as $k - m\Omega \neq 0$, or when $\Omega \neq \omega_n$ in Equation 2.17. As can be seen in Figure 2.3 when the excitation frequency Ω is close to the natural frequency ω_n the frequency-response magnitude tends to infinity for the undamped mechanical system. The phenomena is known as *resonance* and is a condition which one usually strives to avoid, as it leads to large-amplitude motions. For further information the reader is referred to [3]

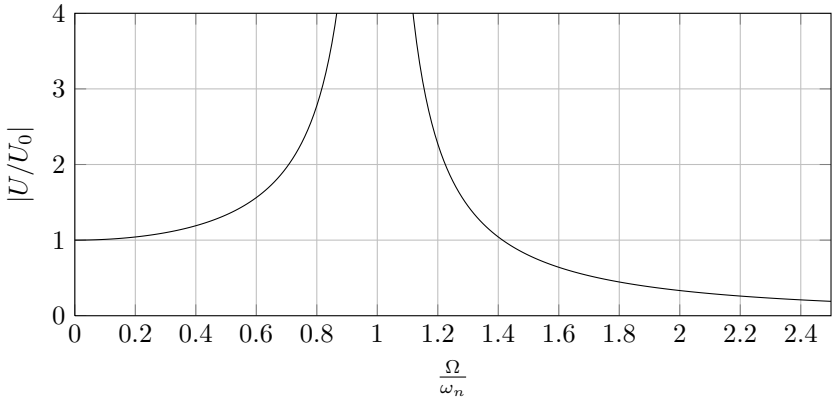

Figure 2.3: *Magnification factor of an undamped SDOF system, Ω is the excitation frequency and ω_n is the natural frequency.*

2.1.4 Steady-state dynamics

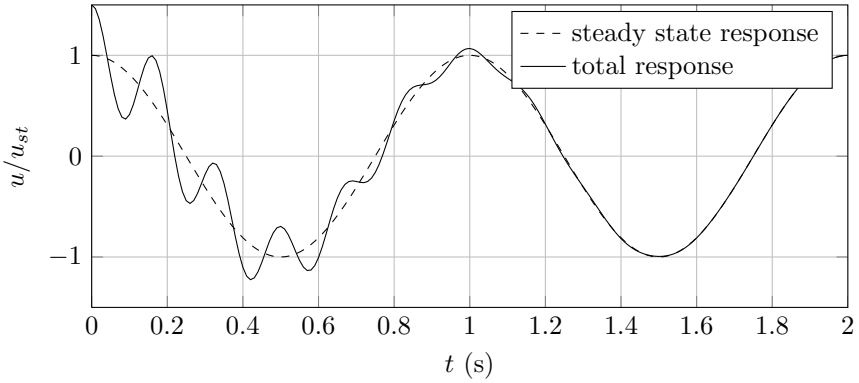

Figure 2.4: *Total and steady state response of a mechanical system under harmonic loading*

When a mechanical system is subject to a harmonic force it will typically reach a steady state after some transient behaviour has been dampened out. Assuming steady state harmonic behaviour with common time factor $e^{i\omega t}$, the equation of motion for a discretized MDOF system can be written using complex arithmetic

$$\mathbf{M}\ddot{\bar{\mathbf{u}}} + \mathbf{C}\dot{\bar{\mathbf{u}}} + \mathbf{K}\bar{\mathbf{u}} = \bar{\mathbf{p}} = \mathbf{p}_0 e^{\mathrm{i}\omega t}; \qquad \bar{\mathbf{u}}(t) = \bar{\mathbf{U}} e^{\mathrm{i}\omega t} \tag{2.18}$$

with the complex response

$$\bar{\mathbf{u}} = \mathbf{u}_{\Re} + \mathbf{u}_{\Im} \tag{2.19}$$

where it is understood that the actual steady-state motion is given by either the real or imaginary part depending on the nature of the excitation (i.e. sin or cos). Differentiating Equation 2.18 with respect to time and omitting the common time factor we get

$$(-\omega^2\mathbf{M} + \mathrm{i}\omega\mathbf{C} + \mathbf{K})\bar{\mathbf{U}} = \mathbf{p}_0 \tag{2.20}$$

or

$$\mathbf{D}(\omega)\bar{\mathbf{U}} = \mathbf{p}_0 \tag{2.21}$$

where $\mathbf{D}(\omega)$ is the dynamic stiffness matrix, dependent on the angular frequency ω

$$\mathbf{D}(\omega) = -\omega^2\mathbf{M} + \mathrm{i}\omega\mathbf{C} + \mathbf{K} \tag{2.22}$$

which may be used to calculate the complex amplitude $\bar{\mathbf{U}}$, which in turn can be used to determine the amplitude and phase of the steady-state response. Note that in later chapters the overbar and uppercase are dropped and the complex amplitude is simply referred to as $\mathbf{u}$. For more information the reader is referred to [3].

2.1.5 Damping

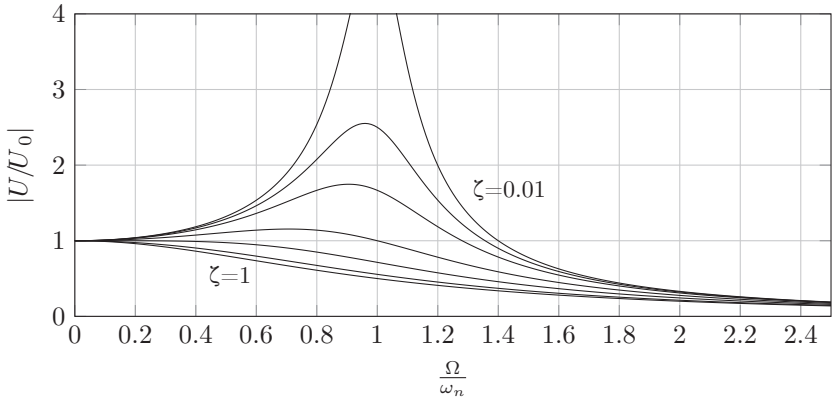

Figure 2.5: *Magnification factor of damped SDOF system, Ω is the excitation frequency and ω_n is the natural frequency.*

Where as the stiffness and mass properties of a system are well understood and can be calculated the exact nature of the damping in a structure is many times impossible to determine. Damping is usually measured on site (or similar structure) and afterwards mathematically modelled. There have been many different damping models proposed, and two which are often used are Rayleigh damping, and structural damping. Structural damping lends itself well to, and can only be used for the complex-frequency-response steady state dynamics. For a single degree of freedom system it is usually introduced as

$$m\ddot{\bar{u}} + k(1 + \mathrm{i}\gamma)\bar{u} = p_0 e^{i\omega t} \tag{2.23}$$

where γ is the structural damping factor. In [3] it is shown that structural damping under harmonic excitation conditions at resonance for a SDOF system relates to viscous damping as

$$\zeta_{\mathrm{eq}} = \gamma/2 \tag{2.24}$$

Rayleigh damping, also known as proportional damping is proportional to a combination of the mass and stiffness matrices. It is defined by

$$\mathbf{C} = \alpha\mathbf{M} + \beta\mathbf{K} \tag{2.25}$$

where the constants α and β can be chosen to specify modal damping factors for two select angular frequencies

$$\zeta_r = \frac{1}{2}\left(\frac{\alpha}{\omega_r} + \beta\omega_r\right) \tag{2.26}$$

where the mass contribution to ζ_r is inversely proportional to ω_r and the stiffness term increases linearly with ω_r.

2.1.6 Root Mean Square

Since the scope of the project work is to compare a large number of dynamic responses a method for comparing them to each other is necessary, as presenting hundreds of them can be time consuming and difficult to read. An efficient way is by looking at the Root Mean Square (RMS) value, as it provides an *efficient average value.*

$$\mathrm{RMS}(\mathbf{u}) = \sqrt{\frac{1}{n}\sum_n \mathbf{u}^2} \tag{2.27}$$

2.2 The Finite Element Method

The finite element method is a technique to find approximate solutions to boundary value problems (BVP), that is, a set of differential equations with additional boundary conditions which are known *a priori*. It is applicable to many fields of engineering, physics and mathematics, since many of the underlying physical problems may be expressed as differential equations.

The method is based on dividing a region governed by a physical phenomena into a set of of smaller regions, or finite elements. Simpler approximations are assumed over the elements which approximate the original complex equations, the solutions are usually allowed to vary linearly or quadratically over the element, even though the physical phenomena may vary in a highly non-linear fashion over the whole region the linear or quadratic approximation may hold over the element, provided the element is small enough. The approximations are some kind of interpolation over the element where it is assumed that the values are known at some certain *nodal* points, which are usually located at the boundary of each element. The second step consists of generating a global set of equations from the local by a co-ordinate transformation from the sub-domains local co-ordinate system and nodes to the domains global co-ordinate system and nodes.

The finite element method is numerically stable, meaning that errors from input and intermediate calculations do not grow and cause inaccuracies which make the results meaningless. To minimize the errors from the approximations (or increase precision) a finer mesh with smaller elements or elements with a higher order of basis functions (e.g. going from linear to quadratic elements) may be used, at of course the expense of computational cost.

2.2.1 FE formulation in 3D

The finite element discretization technique reduces the soil modelling problem to a system of second order, linear, ordinary differential equations:

$$\mathbf{M}\ddot{\mathbf{u}} + \mathbf{C}\dot{\mathbf{u}} + \mathbf{K}\mathbf{u} = \mathbf{f} \qquad \forall t \in (0, T) \tag{2.28}$$

with $\mathbf{u}(t=0) = \mathbf{u}_0$ and $\dot{\mathbf{u}}(t=0) = \dot{\mathbf{u}}_0$, where $\mathbf{M}$ is the mass matrix, $\mathbf{C}$ is the damping matrix, $\mathbf{K}$ is the stiffness matrix, $\mathbf{u}$ is the nodal displacements vector and $\mathbf{f}$ is the force vector. $\mathbf{M}$, $\mathbf{C}$, and $\mathbf{K}$ are sparse, symmetric and positive-definite matrices.

For a full derivation of the FE formulation the reader is referred to [11].

2.2.2 Dynamic model reduction with damping

Model reduction methods within engineering are used to lessen computational costs of an analysis. One of the most common reduction method is referred to as Guyan reduction. A set of active "master" coordinates, and a set of dependent "slave" coordinates which may be reduced are chosen. The $\mathbf{K}$ and $\mathbf{M}$ matrices are then re-ordered and partitioned into separate parts relating to the master and slave degrees of freedom. If no forces are applied to the slave degrees of freedom and the damping is neglectable the equation of motion for the system can be written as (with subscripts m and s for master and slave degrees of freedom)

$$\begin{bmatrix} \mathbf{M}_{mm} & \mathbf{M}_{ms} \\ \mathbf{M}_{sm} & \mathbf{M}_{ss} \end{bmatrix} \begin{Bmatrix} \ddot{\mathbf{u}}_m \\ \ddot{\mathbf{u}}_s \end{Bmatrix} + \begin{bmatrix} \mathbf{K}_{mm} & \mathbf{K}_{ms} \\ \mathbf{K}_{sm} & \mathbf{K}_{ss} \end{bmatrix} \begin{Bmatrix} \mathbf{u}_m \\ \mathbf{u}_s \end{Bmatrix} = \begin{Bmatrix} \mathbf{f}_m \\ 0 \end{Bmatrix} \tag{2.29}$$

by neglecting the inertia terms in Equation 2.29 the transformation matrix T may be written as

$$\begin{Bmatrix} \mathbf{u}_m \\ \mathbf{u}_s \end{Bmatrix} = \begin{bmatrix} \mathbf{I} \\ -\mathbf{K}_{ss}^{-1}\mathbf{K}_{sm} \end{bmatrix} \mathbf{u}_m = \mathbf{T}\mathbf{u}_m \tag{2.30}$$

the reduced mass and stiffness matrices can then be given as

$$\begin{aligned} \mathbf{K}_r &= \mathbf{T}^{\mathrm{T}}\mathbf{K}\mathbf{T} \\ \mathbf{M}_r &= \mathbf{T}^{\mathrm{T}}\mathbf{M}\mathbf{T} \end{aligned} \tag{2.31}$$

The method is exact at frequency zero and approximate at all other frequencies as the inertia terms have been neglected. Guyan reduction may be extended to Dynamic reduction at steady state harmonic conditions by using the dynamic stiffness matrix

$$(\mathbf{K} - \omega^2\mathbf{M})\mathbf{u} = \mathbf{f} \tag{2.32}$$

or expressed in terms of re-ordered master and slave degrees of freedom

$$\begin{bmatrix} \mathbf{K}_{mm} - \omega^2\mathbf{M}_{mm} & \mathbf{K}_{ms} - \omega^2\mathbf{K}_{ms} \\ \mathbf{K}_{sm} - \omega^2\mathbf{M}_{sm} & \mathbf{K}_{ss} - \omega^2\mathbf{K}_{ss} \end{bmatrix} \begin{Bmatrix} \mathbf{u}_m \\ \mathbf{u}_s \end{Bmatrix} = \begin{Bmatrix} \mathbf{f}_m \\ 0 \end{Bmatrix} \tag{2.33}$$

from which we get the transformation matrix $\mathbf{T}$

$$\begin{Bmatrix} \mathbf{u}_m \\ \mathbf{u}_s \end{Bmatrix} = \begin{bmatrix} \mathbf{I} \\ -(\mathbf{K}_{ss} - \omega^2\mathbf{M}_{ss})^{-1}(\mathbf{K}_{sm} - \omega^2\mathbf{M}_{sm}) \end{bmatrix} \mathbf{u}_m = \mathbf{T}\mathbf{u}_m \tag{2.34}$$

which can once again be used in Equation 2.31 to get the reduced system matrices. This method is exact at frequency ω for undamped systems and works well for systems with low damping. If there is significant damping in the system one needs to use the full dynamic matrix

$$(\mathbf{K} + i\omega\mathbf{C} - \omega^2\mathbf{M})\mathbf{u} = \mathbf{f} \tag{2.35}$$

and using Equation 2.35 one gets the transformation matrix

$$\begin{Bmatrix} \mathbf{u}_m \\ \mathbf{u}_s \end{Bmatrix} = \begin{bmatrix} \mathbf{I} \\ -(\mathbf{K}_{ss} + \mathrm{i}\omega\mathbf{C}_{ss} - \omega^2\mathbf{M}_{ss})^{-1}(\mathbf{K}_{sm} + \mathrm{i}\omega\mathbf{C}_{sm} - \omega^2\mathbf{M}_{sm}) \end{bmatrix} \mathbf{u}_m = \mathbf{T}\mathbf{u}_m \tag{2.36}$$

which once again can be used in Equation 2.31 to get the reduced system matrices, where $\mathbf{C}_r$ follows in the same procedure. As no error is introduced in the transformation matrix this method is exact at frequency ω but the resulting reduced system matrices $\mathbf{M}_r$, $\mathbf{C}_r$ and $\mathbf{K}_r$ are complex [14]. It should be noted that the reduced system matrices produced by these methods are no longer sparse and require a rather large reduction of degrees of freedom in order to be of computational benefit.

2.2.3 Multi-level Sub-structuring

Substructuring methods, or domain decomposition methods solve a BVP by dividing it up in smaller BVPs on subdomains. The methods work well for parallel computing, as the problems on the subdomains are independent of each other and can be solved independently. The continuity of the solution over the subdomains is ensured by representing the values of the neighbouring interfaces (where the subdomain boundaries meet) by the same unknowns. Finite element analysis with models of large size (millions of degrees of freedom) typically require hours to solve for each time-step (or frequency), making parallel calculations invaluable for minimizing the calculation time.

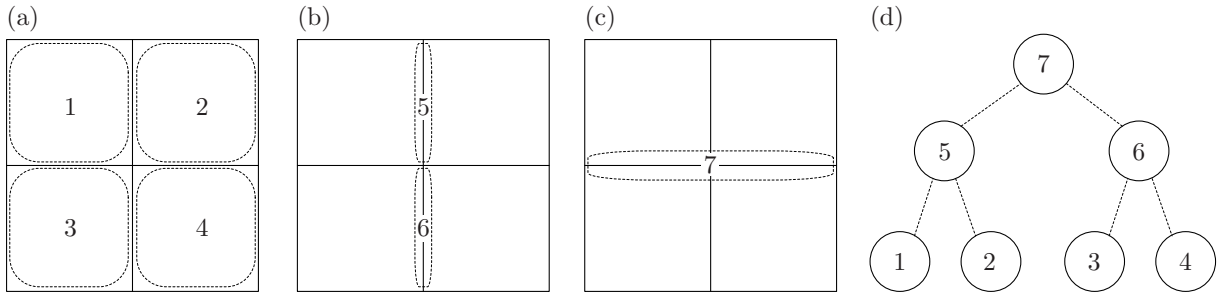

Figure 2.6: *(a) bottom level substructures and internal dofs. (b) higher level substructures and interface dofs for the bottom level substructures (dashed area). (c) highest level substructure with interface dofs between substructures 5 and 6. (d) substructure tree*

To illustrate a method of sub-structuring Figure 2.6 is showing a domain divided into four sub-domains. Each domain has a set of internal degrees of freedom (Figure 2.6 (a)), and interface degrees of freedom (Figure 2.6 (b)) which are used to connect it to the next substructure level, which again has sets of internal and interface degrees of freedom used to connect it to the final level seen in Figure 2.6 (c).

In this study the substructuring method has been used to decrease the computational cost and time of the dynamic reduction, where the dynamic reduction has been applied to each substructure level starting at the bottom of the substructure tree (Figure 2.6 (d)) and only keeping the interface and master degrees of freedom.

2.3 Wave propagation in semi-infinite spaces

2.3.1 Wave types in semi-infinite spaces

Wave propagation in viscoelastic mediums usually consists of three types of waves, Rayleigh-wave (R-wave) which propagates close to the surface of the semi-infinite space, also known as a surface wave. The other two waves are body waves propagating trough the semi-infinite space, one is a pressure wave (P-wave) and the other is a shear wave (S-wave). Measuring at a point a distance away from the source one can see that the pressure wave arrives first, then the shear wave and a little bit later the Rayleigh wave, as illustrated in Figure 2.7. The figure also shows that the Rayleigh wave usually has a larger amplitude than the body waves.

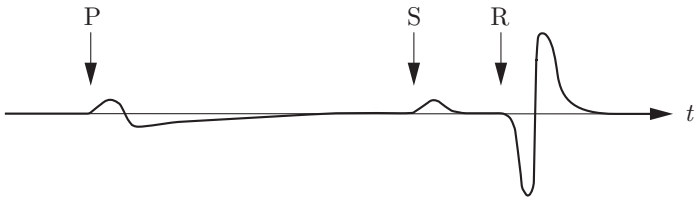

Figure 2.7: *Amplitude and time of arrival of the three different wave types at an observation point some distance away from the vibration source*

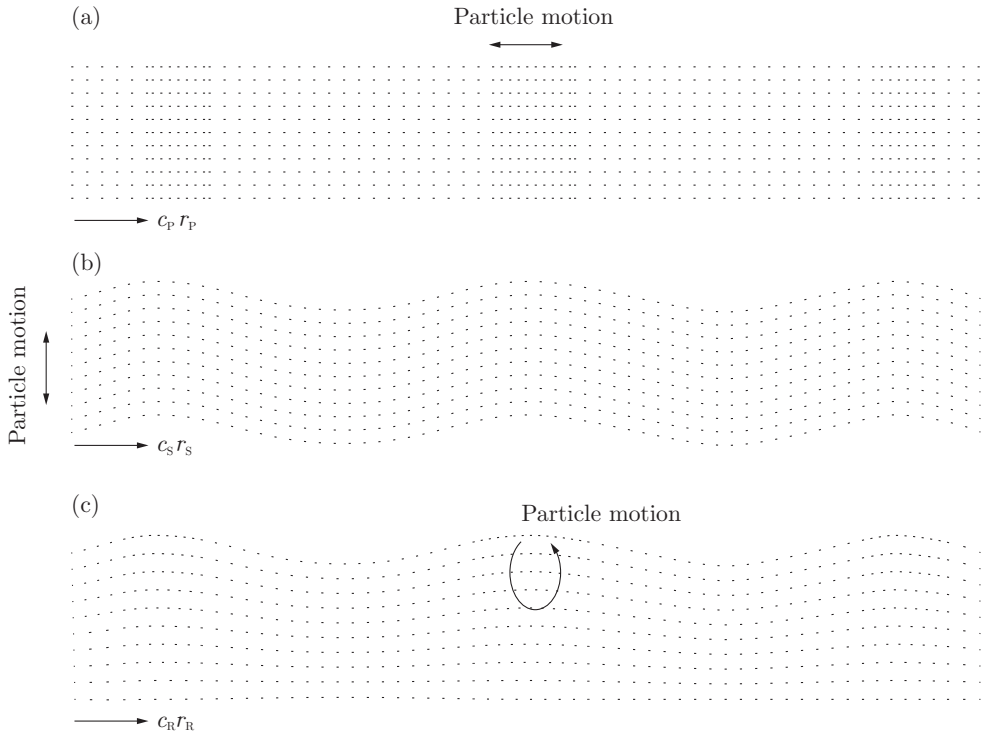

Figure 2.8: *Illustrating the particle motion of (a) pressure waves with phase speed c_P, (b) shear waves with phase speed c_S and (c) Rayleigh waves with phase speed c_R*

Unlike P- and S- waves the Rayleigh wave consists of both pressure and shear. The particle motion from a Rayleigh wave follows an elliptical path, as illustrated by Figure 2.8 (c). Rayleigh waves typically move at a phase speed of around $c_R \approx 0.9c_S$. A Rayleigh waves penetration depth is dependent on its wavelength.

2.3.2 Geometrical attenuation

As pressure and shear waves spread trough the volume they form spherical wave fronts spreading the wave energy over a larger area than the Rayleigh waves which are bound to the surface and spread in a similar fashion to rings on water, as illustrated in Figure 2.9. The effect is sometimes improperly denoted as geometrical damping (improper as there is no energy loss related to the effect), and somewhat explains why Rayleigh waves are observed to have larger magnitudes than body waves far from the vibration source. Another explanation is that vibrations caused by sources on the ground primarily lead to the generation of Rayleigh waves.

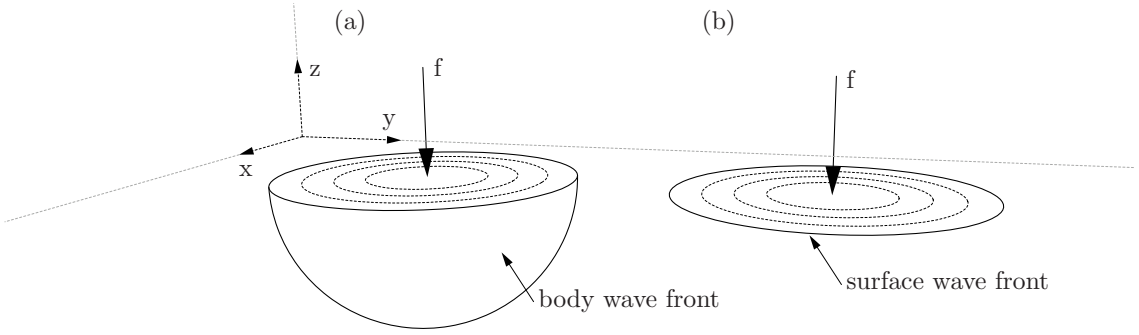

Figure 2.9: *Illustrating the wave fronts of (a) body waves, and (b) surface waves*

2.4 Materials

2.4.1 Soil

It is claimed that Lund has the largest height difference of all the cities in Sweden, but it is not true. The whole city lays on a slope though, with the lowest point of 8 meters above sea level in the south of Lund, and the highest point of 86 meters above sea level in the north-east part, where MAX-ab is located. Most of the bedrock consisting of shale, limestone and sandstone is at the location for MAX-lab covered by 14-16 meters of clay.

The clay layers are glacial sediments from the from the moraines of the retreating ice from the last ice age. There are two layers, the upper one is Low Baltic clay till and the lower one is North-east clay till. Boulder clays are usually water saturated, since water is incompressible this leads to the clay having a poisson's ratio which is close to 0.5. The density of boulder clay is usually close to 2000kg/m^3. The damping ratio is strain dependent and varies between 1% to 20%.

The pressure from the ice of the last ice age has lead to over-consolidation of the soil, meaning that the response is assumed to be elastic in shearing when exposed to loads with amplitude smaller than the pre-consolidation pressure.

2.4.2 Soil as a homogeneous and visco-elastic material

The stresses from dynamic loads due to human activity (e.g. traffic) are often within the linear range of the soil material, and as such a visco-elastic material model may be used for the soil. The inclusion of damping in the model complicates the computations of the response for dynamic analysis but usually provides a much better description.

Soil is a inhomogeneous material with large variations of size, shape and density to the particles which it consists of. The Rayleigh wave-speed for most soils is usually above 100 m/s, and for a frequency of 100 Hz the wavelength is 1 meter, which is significantly larger than the soil grains which are around 1 mm in size. Because of this the soil may be treated as a homogeneous material when it is used for dynamic analysis of low frequencies which are the case for most human induced loads. One does need to consider the different soil depth layers which may have different properties in relation to each other.

The elastic properties of deeper layers are usually stiffer due to pre-stressing from layers above. It is usually sufficient with three layers to get a good description of the wave propagation in soil [2].

3 Experimental Models

The finite element software *ABAQUS*[18] was used for the FE calculations. Work was mainly within the CAE (Complete Abaqus Environment), but a few things were done manually as *ABAQUS/CAE* lacks support for infinite elements. These have to be added manually to the input (*.inp*) file before the job is submitted to the solver.

A 2D axisymmetric model was used to study the effects of a single mass, and the effects of two masses. Afterwards a 3D model was set up to study the effects of different organizations of masses. Eventually the 3D-model was exported into *MATLAB* (Matrix Laboratory) where a dynamic model reduction was performed in order to speed up the steady-state simulations.

Some tests with physical scale models were attempted, but in the end disregarded as no suitable materials were found.

3.1 2D Axisymmetric FE-Model

An axisymmetric model was used for preliminary analysis. The computational cost for an axisymmetric model is much lower then for a full 3D model, while it can still take geometric attenuation into account. Figure 3.1 shows the axisymmetric model.

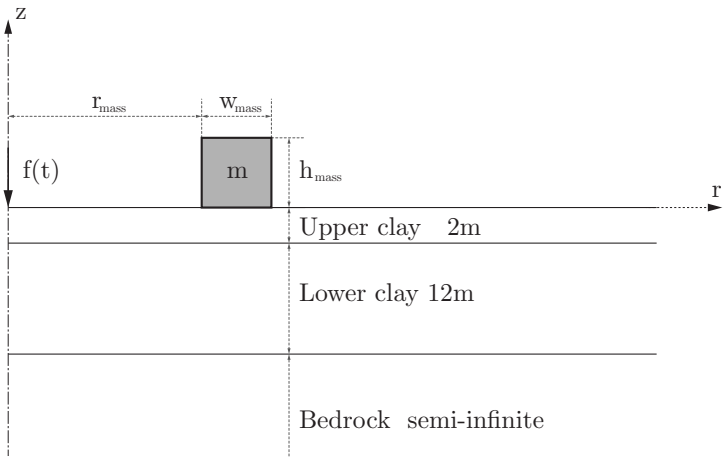

Figure 3.1: *Axisymmetric model*

3.1.1 Materials

Due to the strict requirements for vibrations at MAXLAB the site has been subject to many geotechnical studies by LTH, Tyréns, NGI and PEAB (amongst others) [15]. The material properties for the part of the site between the synchrotron and town can be seen in Figure 3.1 and Table 3.1. The soil is highly water saturated and as such has a Poisson's ratio close to 0.5. Damping is given as a loss factor, and is 0.14 for the soil, and 0.04 for the bedrock.

The largest amplitudes occur in the frequency range 5-30 Hz, for which the smallest wavelength in the soil can be found:

$$\lambda_{\text{Upperclay}} = c_{\text{S}}/f = 185/30 = 6.16\text{m} \tag{3.1}$$

and the largest wavelength in the bedrock:

$$\lambda_{\text{Bedrock}} = c_{\text{P}}/f = 2694/5 = 538.8\text{m} \tag{3.2}$$

Material properties for the mass are explained in each analysis.

Table 3.1: Soil and bedrock viscoelastic properties by loss factor

Layer	c_S [m/s]	ν	ρ [Kg/m^3]	loss factor γ [%]	E [MPa]	G [MPa]	c_P [m/s]
Upper clay	185	0.48	2125	14	215	73	943
Lower clay	425	0.48	2125	14	1136	384	2167
Bedrock	1100	0.40	2600	4	8800	3146	2694

3.1.2 Mesh, element types and boundary conditions

When working with semi-infinite spaces such as soil one is typically interested in the results from a small region but must model a larger part in order to avoid reflections of waves. The reflections may further be reduced by incorporating a non-reflective boundary. In *ABAQUS*[18] that boundary may be done with the use of infinite elements, which in this case were *CINAX5R*, 5-noded with quadratic interpolation. Even when these elements are used at the boundary one still needs to include a large enough part in the FE-model to avoid reflections. Together with requirements for a dense mesh (in order to accurately model the smallest wavelengths) this can quickly lead to high computational costs.

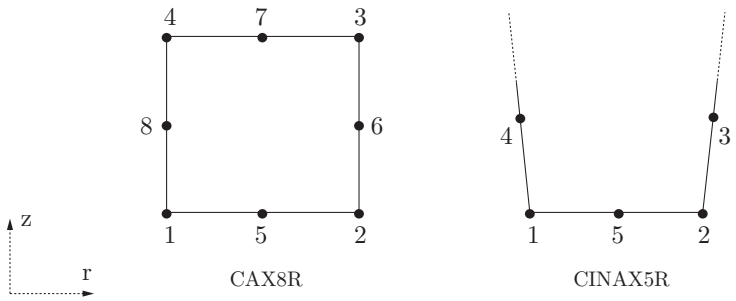

Figure 3.2: *Axisymmetric elements and node numbering*

As most of the boundary conditions are handled with the infinite elements the only constraint necessary in the model is that of horizontal displacements along the z-axis where $r = 0$, a condition which must hold for the axisymmetric model.

In [16], it is concluded that to correctly model a wave using the finite element method it is necessary to use atleast 10 nodes per wavelength. If using quadratic elements, *CAX8R* it means that one needs 4.5 elements per wavelength. The smallest wavelength in the model is about 6.16m (top soil layer) Eq 3.1. Following the guidelines from [16] that would require a element size of about 1.37 by 1.37 meters, however, from mesh convergence plots (see Section 4.1.1) it was concluded that a 2x2 meter mesh for the soil layers was accurate enough for all frequencies in the range 5-30 Hz, computational times for a mesh with 2x2 meter elements (600x600 meters total dimensions) in an axisymmetric model are not a big issue. For the bedrock which is stiffer and has a larger smallest wavelength a mesh with longer elements (8.8 meters) in z-direction was used.

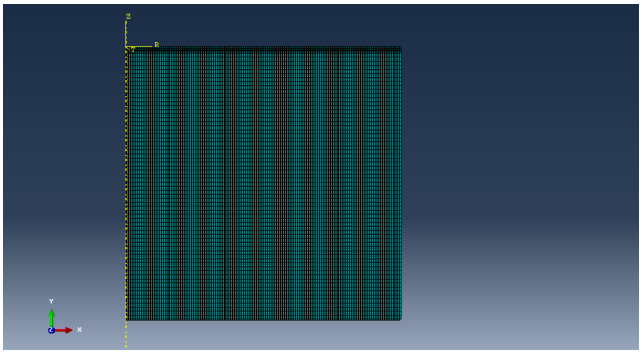

Figure 3.3: *The complete mesh, 602 meters wide, and 596 meters deep.*

In order for the infinite elements, *CINAX5R* to be effective and provide a *quiet* boundary they should be perpendicular to the direction of the incoming wave [18], as the model is rectangular in design it means that this is only true for parts of the model straight below, or to the right of the load. Increasing the dimensions of the model leads to a larger part of the incoming wave front to be closer to a perpendicular direction.

The final soil 2-D mesh consisted of 373 CINAX5R elements and 21900 CAX8R elements for a total of 67570 nodes and 135140 degrees of freedom.

3.1.3 Model with a single mass

For the first test the mass used on the soil had the width $w_{\text{mass}} = 2\text{m}$ and height $h_{\text{mass}} = 2\text{m}$ and was located $r_{\text{mass}} = 16\text{m}$ from the load. All other properties for the mass were identical to the upper soil layer, except for the mass density, as it was varied between $0 - 4.5 \cdot 10^4 \text{kg/m}^3$. The upper bound for the density is larger than traditionally used materials, but the idea is to find a functioning *mass per unit area*, meaning that even if the mass density is unachievable simply increasing the hight of the mass could have similar effect. Krylov [8] goes so far as to describe the resonance frequency of the mass-soil system (for a 2-dimensional analytical model) as a function of stiffness, density, and *height*, where the resonance frequency is inversely proportional to the square root of h. Naturally this was another simulation that was performed in the model with a single mass. The height h was varied between 2-12 meters in steps of 2 meters, while the density was reduced in order to keep the *mass per unit area* constant. For this test Young's modulus was $\text{E} = 50\text{GPa}$. Variations of Young's modulus (from 215MPa to 210Gpa) and Poisson's ratio (0.2 - 0.48) were also studied.

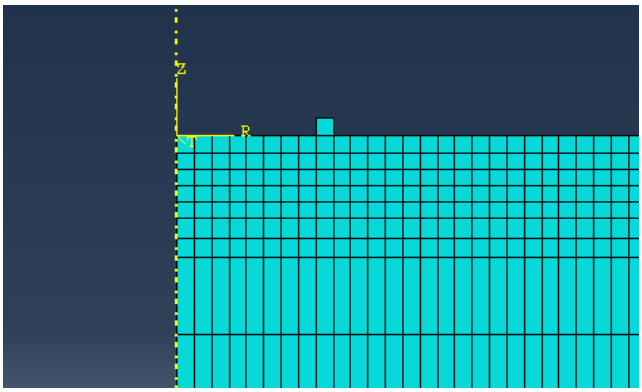

Figure 3.4: *Part of mesh with a mass on top, longer elements are bedrock.*

Petyt and Jones [5] conclude that the position of the mass in relation to the load and response point is critical for its effectiveness (in general a heavy mass close to the load worked well for their tests), as such it was necessary to study the effect of the position of the mass in this thesis as well. The mass position from the load r_{mass} was varied between 0m to 60m in 4m steps. The mass density was initially set to $\rho_{\text{mass}} = 8271\text{kg/m}^3$. All other properties were the same as for the upper clay described in Table 3.1. For all simulations a a steady-state analysis in the frequency range 5-30Hz with a unit load and 0.25Hz steps was done.

To conclude the parameters that were studied in the model with one mass can be seen in Figure 3.1 and were:

- Density of the mass, ρ_{mass}
- Young's modulus of the mass, E
- Poisson's ratio of the mass, ν
- Position of the mass, r_{mass}
- Height of the mass, h_{mass} with modified mass density to keep the total mass constant

3.1.4 Model with two masses

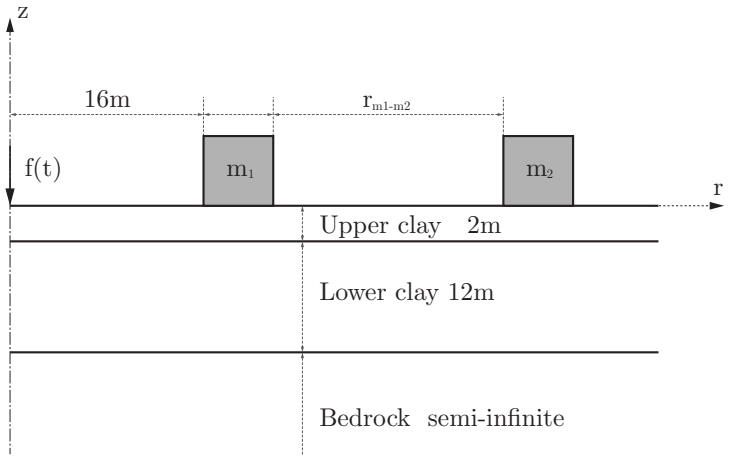

Figure 3.5: *Axisymmetric model with two masses*

To investigate if there are any benefits of using two or more masses a model with two masses was used. Having found an effective weight and position for the first mass, it made sense to start with using the same weight for the second mass, and varying its position relative to the first mass, $r_{\mathrm{m1-m2}}$. Analyses were done with two masses of same initial density $\rho = 8271\mathrm{kg/m^3}$, with the first mass located at 16 meters from load and the distance between the two masses varied between 0 - 40 meters, in steps of 4 meters.

Once a suitable position was found for the second mass, the density of the second mass was varied between $0\mathrm{kg/m^3}$ to $8271\mathrm{kg/m^3}$.

All other parameters for the masses were taken from those of the upper soil layer in Table 3.1, except the damping which was neglected.

In conclusion only two parameters were studied in the model with two masses:

- The position of the second mass in relation to the first, $r_{\mathrm{m1-m2}}$
- The density of the second mass, after having found the position for the second mass with best reduction in RMS($|u_z|$)

3.1.5 Model with a simple building

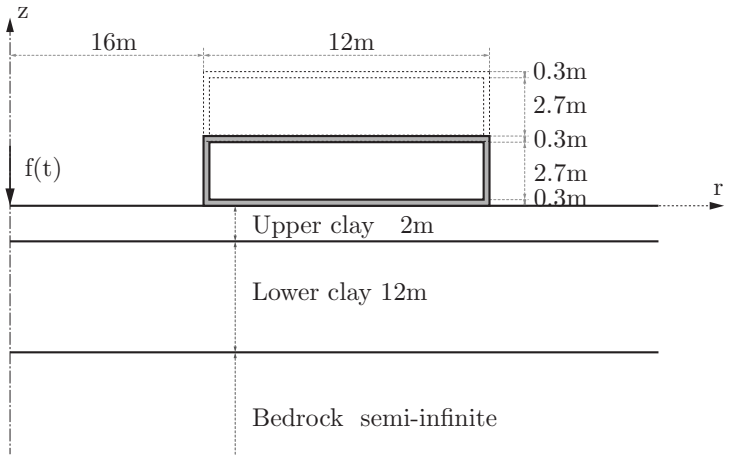

Figure 3.6: *Axisymmetric model with building*

Simple building models according to Figure 3.6 were tested to study if a building might be used as vibration mitigation. The properties for the building material were taken as $\rho = 2400\text{kg/m}^3$ and $E = 30\text{GPa}$, $\nu = 0.2$. The number of floors was varied between 1-10, and a steady state analysis was done for each model between 5-30Hz.

3.2 3D FE-Model

A full 3-D model was set up to study the effects of masses in 3-D. Pre-processing was carried out in *ABAQUS* and the global system matrices **K**, **C**, and **M** were exported into *MATLAB* where a dynamic model reduction was performed in order to reduce the number of degrees of freedom and speed up the analysis. The dynamic reduction was too computationally intensive on the full 3D model which was solved by dividing the model into substructures and performing the reduction in several iterations. Having performed the reduction different organizations of masses were finally assembled on the green area seen in Figure 3.7 and steady state analysis in the range 5-29Hz with 2Hz steps and unit loading was run.

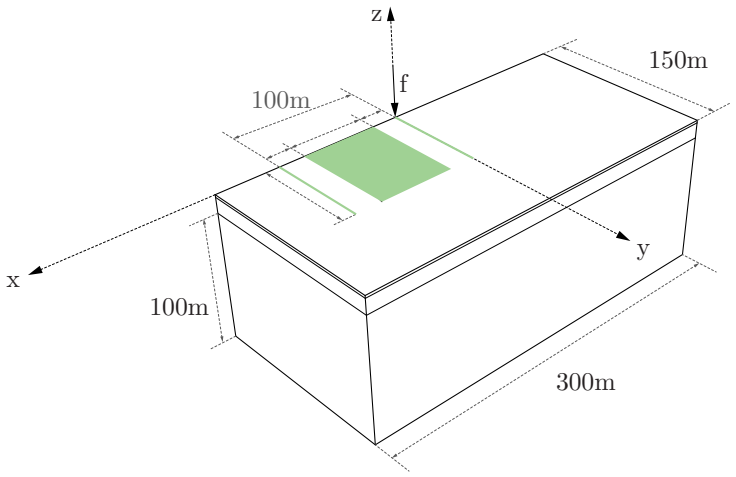

Figure 3.7: *3D model with the parts that were kept in the reduced model marked in green*

3.2.1 Materials

For the 3D model Rayleigh damping was used as the system matrices **K**, **C**, and **M** were exported in to *MATLAB* in order to perform a model reduction. It would have been possible to use structural damping, but the way *ABAQUS* exported the infinite elements was as a set of viscous dampers giving contributions to the damping matrix **C**, which if one would use structural damping would mean that 4 matrices instead of 3 would have to be dealt with which would end up costing more memory. Materials were identical to those in Section 3.1.1. The Rayleigh damping parameters are listed in Table 3.2, they were the ones that gave to closest match to the response with structural damping. In Figure 3.8 the Rayleigh and equivalent structural damping (ζ_{eq}) ratios are shown.

Table 3.2: Soil and bedrock Rayleigh damping parameters

Layer	α (1/s)	β (s)
Upper clay	6.8157	6.4585e-4
Lower clay	6.8157	6.4584e-4
Bedrock	1.9473	1.8453e-4

3.2.2 Geometry, mesh, element types and boundary conditions

The 3D mesh used in *ABAQUS* had the smallest possible dimensions which still gave acceptable values 100m from load application point. The dimensions were selected from 2D-axisymmetric simulations, as doing convergence tests for 3D model would take far too much computational time. In the end the 3D model results were compared to those of the axisymmetric one to make sure that the model was accurate enough. To further reduce computational time a symmetry plane perpendicular to the y-axis at $y = 0$ was used. The model dimensions were $300 \cdot 150 \cdot 114$ meters ($x \cdot y \cdot z$), as seen in Figure 3.7. An increase in x and y to 400 and 200

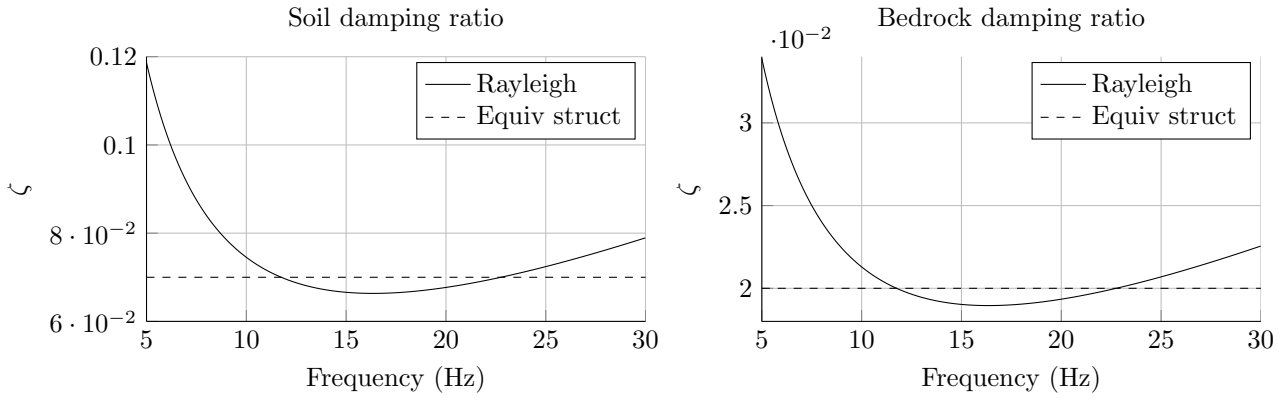

Figure 3.8: *Rayleigh and equivalent structural damping ratios for (left) soil and (right) bedrock.*

meters would give slightly more accurate results but would mean an increase of number of elements by around 1.8.

The 3D mesh was made out of *C3D20R* and *CIN3D12R*. The elements were 2x2x2m, except for the bedrock z-direction which was set to 8.8m. *C3D20R* are 20-node 3D quadratic brick elements with reduced integration. Reduced integration is used instead of full integration in order to avoid too stiff solutions, and according to the *ABAQUS* manual [18] second-order reduced-integration elements generally yield more accurate results than the corresponding elements with full integration while also having a 3.5 times less costly element assembly (8 vs 27 inegration points for *C3D20R*). A single *C3D20R* element has 60 degrees of freedom, with three translational DOFs per node.

The node-numbering for the *CIN3D12R* infinite elements is crucial for the elements to work properly. Figure 3.9 shows both *C3D20R* and *CIN3D12R*, and as can be seen for the infinite element the face with nodes 1 to 8 is the one that should be connected to the finite elements. As *ABAQUS/CAE 6.11-3* lacked support for infinite elements they were first meshed as *C3D20RH* and the output was ran trough a *MATLAB* script which changed them to *CIN3D12R* with the correct topology.

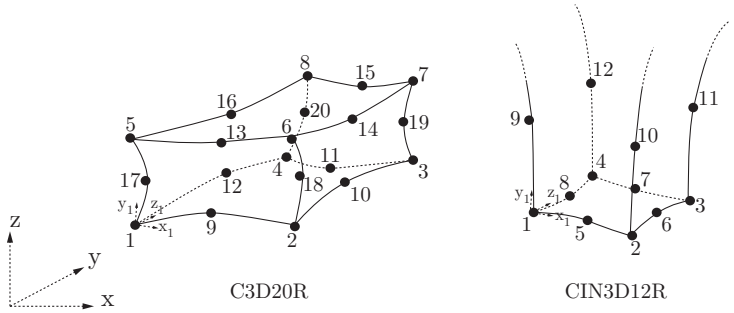

Figure 3.9: *3D elements and node numbering*

The final model had 202 500 *C3D20R* elements, 16 650 *CIN3D12R* elements and 2 620 860 degrees of freedom.

Measurements were done as close as possible to the E-22, just on the other side of the shoulder to which a curve fitting seen in Figure 3.10 was done and the results were regarded as the *frequency content of the traffic*. These were used as loading for both the flat 3D model without any masses, and to the 3D models with masses applied, meaning it could be used to check for relative improvements in results, and not absolute values.

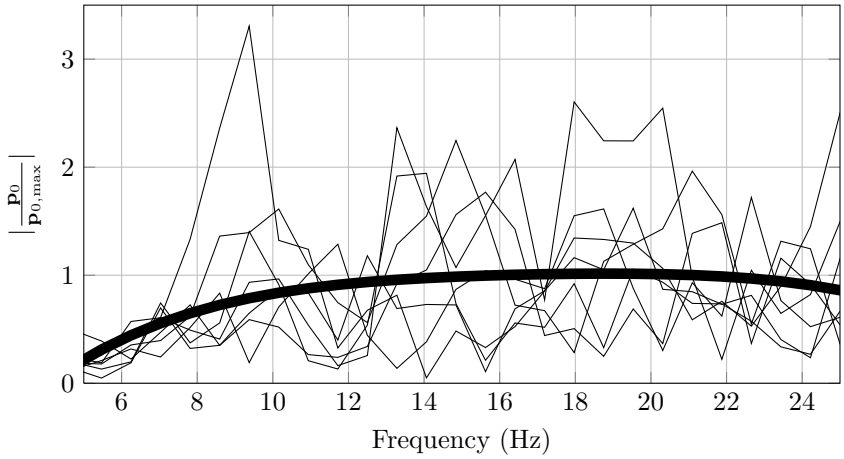

Figure 3.10: *Load amplitude adjusted to the frequency content of the traffic and normalized to the highest value, 7 worst traffic samples plus curve-fitted load amplitude.*

3.2.3 Substructuring and Dynamic reduction of soil model

Figure 3.7 shows the final dimensions of the model and the master degrees of freedom from the soil model which were the only ones kept after reduction of the system. The reduced system matrices from the dynamic reduction method are frequency dependent and only give exact solutions at a certain frequency meaning that a reduced system had to be made for each frequency that was part of the steady state analysis. As the largest displacements are in the 5-30Hz range and the amount of samples was needed to be kept low the frequencies ranged from 5-29Hz with steps of 2Hz.

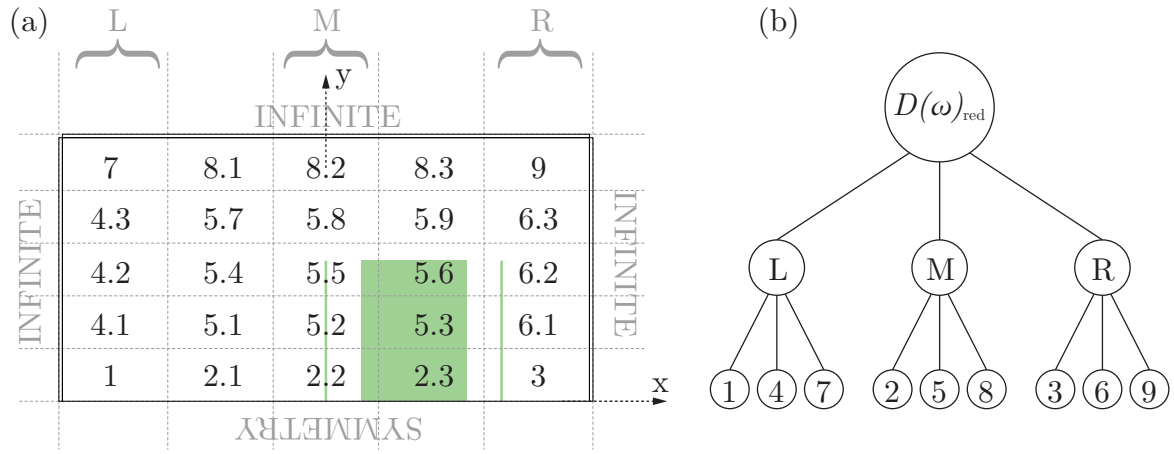

Figure 3.11: *(a) Top view of model with substructures (b) Substructure assembly order*

Since the whole model had 2 620 860 degrees of freedom, performing a dynamic reduction directly proved to be computationally difficult. The structure was then divided into 25 substructures by simply slicing the model into pieces from the top view as indicated by Figure 3.11 (a). The top view was used because it offered simplicity to sub-structuring script plus the fact that the bedrock elements were much longer in z-direction meant that the number of nodes in all three directions of the substructure would be fairly even providing a favourable ratio between internal and interface degrees of freedom. Each substructure ended up including around 100 000 degrees of freedom. Out of the 25 substructures nine were identified as unique and the others simply as copies of those nine but with other co-ordinates, meaning that only nine of the substructures were needed to build the final model. Figure 3.12 shows the mesh and layers of substructure 1.

For each substructure the degrees of freedom to be kept, to be reduced out and to be used as interfaces between structures were identified and in the first sub-structuring level shown in the bottom of Figure 3.11

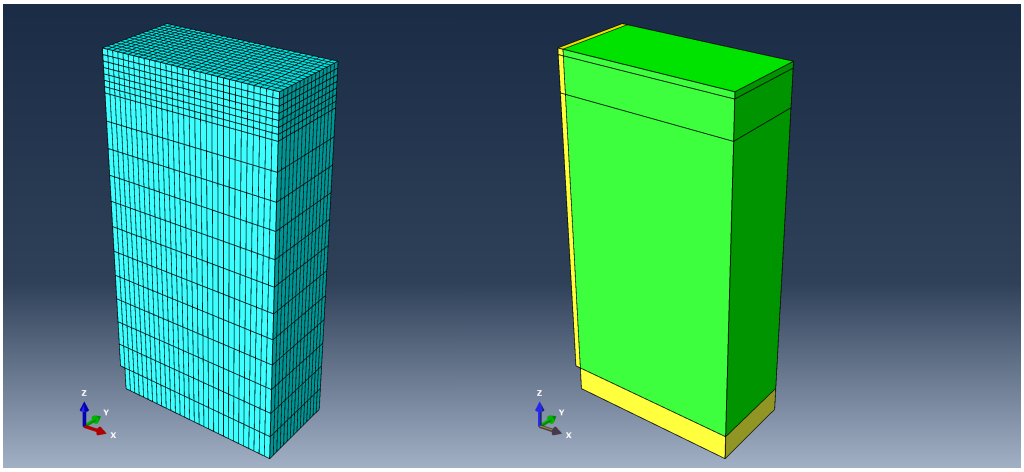

Figure 3.12: *(left) Mesh of substructure 1 (right) Material layers of substructure 1, infinite layers are marked in yellow*

(b), the degrees of freedom the be reduced out were reduced in all nine substructures. In step two the *Left*, *Middle* and *Right* parts consisting of (1 - 4.1 - 4.2 - 4.3 - 7), (2.2 - 5.2 - 5.5 - 5.8 - 8.2) and (3 - 6.1 - 6.2 - 6.3 - 9) respectively were assembled together using primal assembly and a new sets of degrees of freedom could be identified to be kept and to be reduced at the next substructure level. Finally the *Left*, 3 *Middle*, and *Right* parts were connected together and reduced to form the final reduced matrix $\mathbf{D}(\omega)_{\text{red}}$ for each ω.

The reduced system was assembled together with different patterns of masses in the area marked in Figure 3.7. Initially it was planned to use the whole soil area between the load and evaluation point for placement of masses, but since the reduced soil system consisted of full and complex matrices it was important to keep down the number of degrees of freedom as much as possible. The final reduced soil model consisted of 11646 degrees of freedom, taking up about 2.5Gb of memory per matrix. To further keep down the memory use only the dynamic matrices $\mathbf{D}(\omega) = \mathbf{K} + i\omega\mathbf{C} - \omega^2\mathbf{M}$ were kept as the $\mathbf{K}$, $\mathbf{C}$ and $\mathbf{M}$ matrices were already frequency dependent and of no further interest.

3.2.4 Patterns

The possible area to place masses on was between $x \in [20 : 80]$, $y \in [0 : 80]$, with a mesh size of two by two meters the total number of possible positions for placing a mass was $30 \cdot 40 = 1200$. Built in functions in MATLAB were used to read gray-scale images of 30x40 pixels, where each pixel was a possible position for a mass and the value of the pixel was used for the mass density, white meant no density (no mass assembled at the position) and black meant the largest density, $\rho = 8271\text{kg/m}^3$ unless otherwise stated. The same type of 20-node quadratic brick elements *C3D20R* were used for the masses as for the soil. No material damping was applied to the masses, and Young's modulus was set to E = 215MPa, and poissions' ratio $\nu = 0.48$, that is the same as the properties for the upper soil layer seen in Table 3.1. In the case of the building patterns, and some others (mentioned next to the results) a Young's modulus of E = 30GPa was used.

Initial 3D simulations were done with a mass at the point closest to the load to study the effect of a single mass, and another test with a line mass, Figure 3.13 (a) was done in order to compare to 2D tests, as it was deemed the closest possible match to the axisymmetric test with a single mass, the only things different about them being the geometry (line vs. circle), position from load (16 meters for axisymmetric, 20 meters for 3D) and damping model(Structural damping in axisymmetrix, Rayleigh damping in 3D).

The model allowed for any configuration of masses to be investigated, and most of the patterns that were used were classified into the following types:

Walls were made of a line, or a set of lines that were parallel to the y-axis, that is perpendicular to the main wave-propagation direction from the source to the evaluation points, like a barrier.

Lines were similar to the walls, but did not span the whole distance along the y-axis, and if there were more rows of them they were allowed to be shifted in relation to each other.

Perpedicular lines were lines that were ordered to go in the main direction of the wave propagation.

Dots and checkered patterns were tried out both with individual masses (dots) placed in an ordered fashion, and also with larger sets of masses order in a checkered pattern.

Diagonals with many masses of varying density were tested.

Free form patterns were painted out in some different manners to see if anything out of the ordinary might happen.

Buildings. Some organizations of masses that were more in the scale of buildings were also tried out, for all of these the Young's modulus was set to E = 30GPa. Some parts of the buildings of the architectural thesis proposal were also tried as patterns.

Figure 3.13 shows some examples of the different types of patterns.

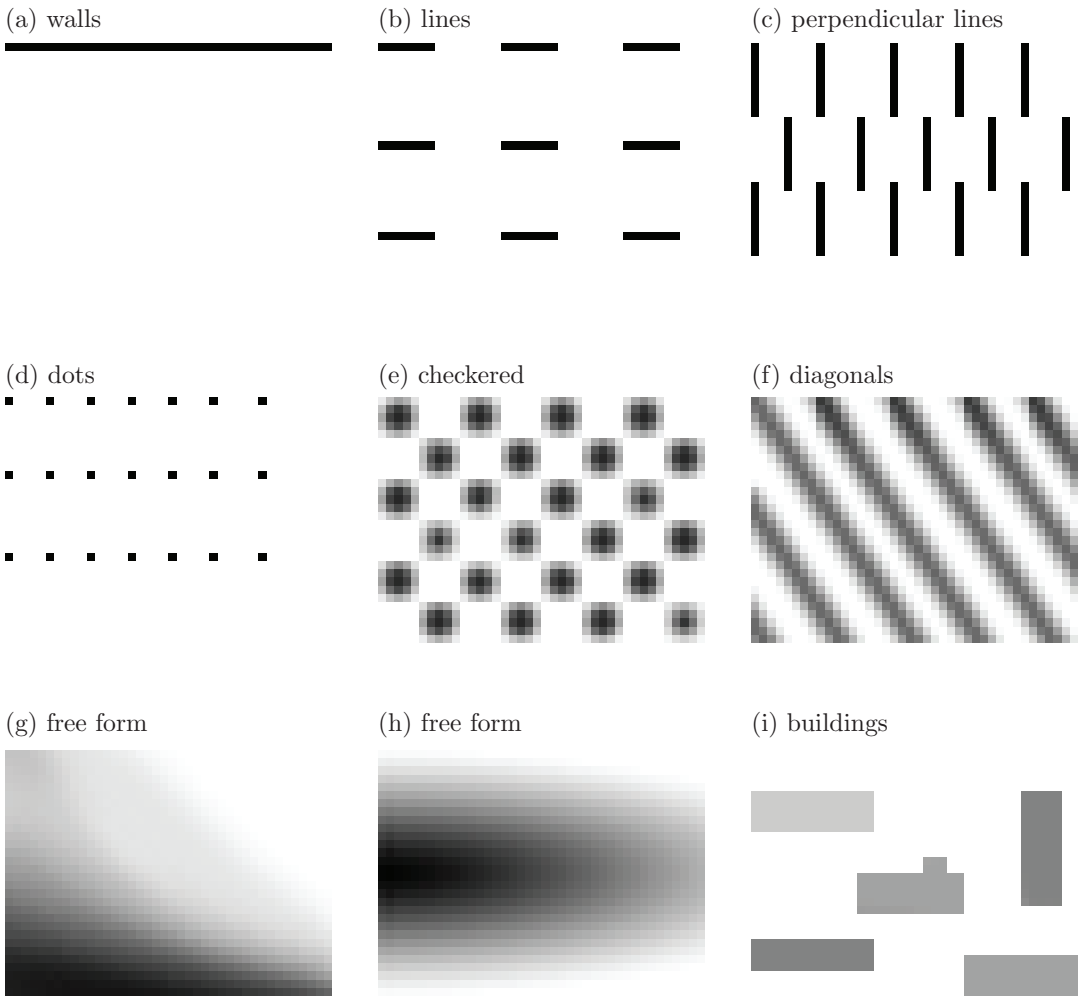

Figure 3.13: *Different types of patterns used in 3D simulations.*

3.3 Scale model

The approach to the scale model was to as accurately as possible model the scale of the masses/blocks in relation to the wavelengths at the excited frequencies in the scale model soil material(JELL-O), and to then search for mass densities for the blocks/masses which would show a visible reduction of the wave propagation in the JELL-O. Once working blocks were found the plan was to organize them into different patterns in order to see the effect. Trying to model a scaled down version of the bedrock as well was deemed far to complicated and fell outside of the scope of this thesis.

3.3.1 Materials

Two types of gelatin powder was used for the JELL-O, one JELL-O mixture, and the other was pure gelatin that was tried in different concentrations. Both were also tried with an added concentration of salt as an attempt to improve the mechanical properties so that the JELL-O wouldn't break as easily. As an alternative to JELL-O some very soft mixtures of bentonite-clay were also tried out with the aim to get similar properties to those of JELL-O.

Figure 3.14: *(Left) the two powders. (Right) the physical model.*

4 Results

All of the results in this chapter that are comparing many responses are presented as the amplification $\mathrm{AMP}_{\mathrm{RMS}}(|u_z|)$ values, which consist the RMS vertical displacement magnitude response for the tested model with masses normalized to the RMS vertical displacement magnitude response for the model with the soil only and no masses,

$$\mathrm{AMP}_{\mathrm{RMS}}(|u_z|) = \frac{\mathrm{RMS}(|u_z|)_{\mathrm{testedmodel}}}{\mathrm{RMS}(|u_z|)_{\mathrm{soilonlymodel}}} \tag{4.1}$$

meaning that a value of over one is a larger value in RMS vertical displacement magnitude response compared to the soil only model at the same degree of freedom, and a value less than one is smaller.

4.1 Axisymmetric FE-Model results

4.1.1 Convergence of axisymmetric soil model

Different widths of the model, and depths of the bedrock were tried together with the quiet boundary conditions in order to minimize the necessary size of the FE-model. As shown in Figure 4.1, with increasing depth of the bedrock results for the magnitude of vertical displacements converge. Smaller bedrock depths mainly affect lower frequencies, if the depth is only 100 meters results diverge for frequencies lower than 5 Hz, but provide similar results as the other tests up until about 100Hz.

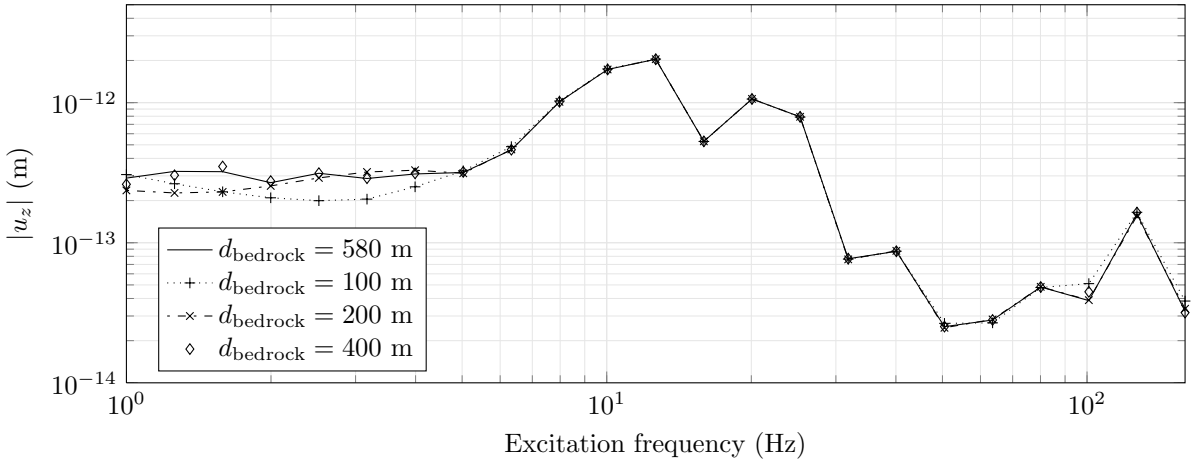

Figure 4.1: *Vertical displacement magnitude response with different bedrock depths, evaluated at 100 meters from the load application point.*

A mesh convergence was tried with meshes of 4x4, 2x2, 1.5x1.5 and 1x1 meters. A mesh of 4x4 meters diverges significantly from the finer meshes for frequencies higher than 30Hz. At 50 Hz the 2x2m mesh starts to diverge from the finer meshes. The largest amplitudes occur in the range 5-30Hz, and for a mesh of 2x2 meters a steady-state analysis in the frequency range 5-50 Hz (0.25Hz steps) takes around 30 minutes on an Intel E5400 with 4GB of RAM.

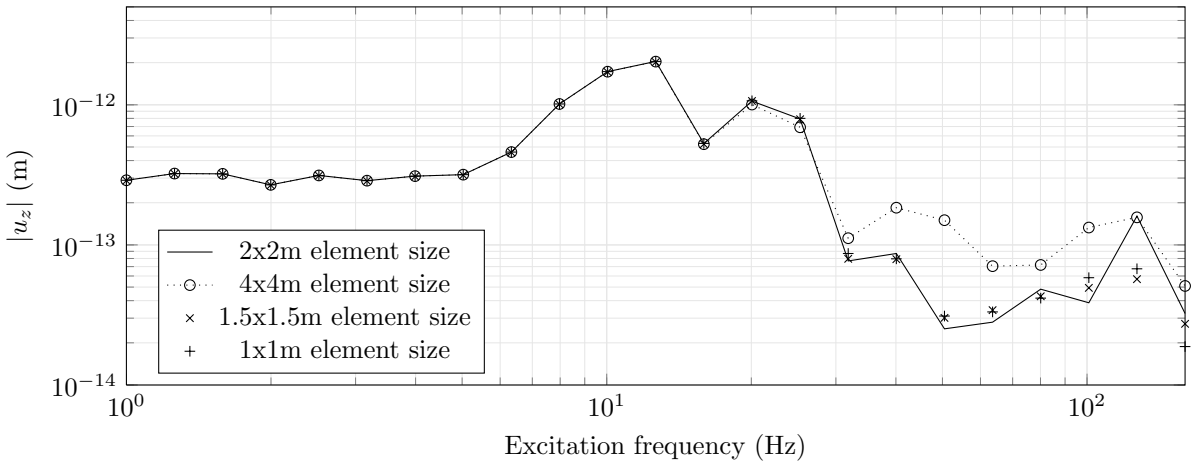

Figure 4.2: *Vertical displacement magnitude response with different mesh resolutions, evaluated at 100 meters from the load application point.*

Due to the bedrock being much stiffer than the soil, wavelengths in the bedrock are generally larger, and as such the mesh may be coarser in the bedrock (but only in z-direction, as r-dimension of elements needs to match those of the soil). Figure 4.3 shows the influence of increasing the size of the bedrock mesh.

Figure 4.4 shows the impact of the width of the model. The model with 150 meters width shows slight

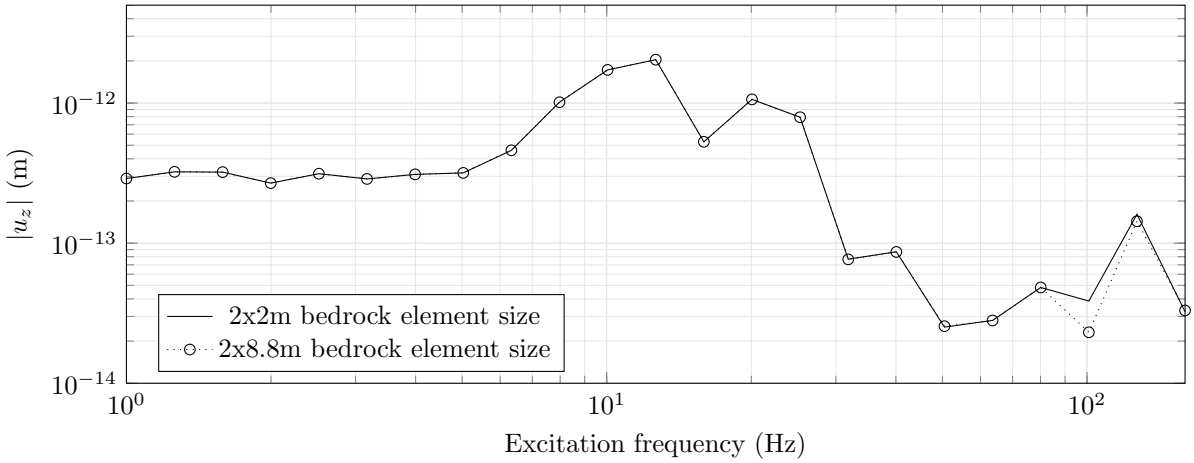

Figure 4.3: *Vertical displacement magnitude response with different bedrock mesh resolutions, evaluated at 100 meters from the load application point.*

deviation from the wider models in the range from 7-15Hz.

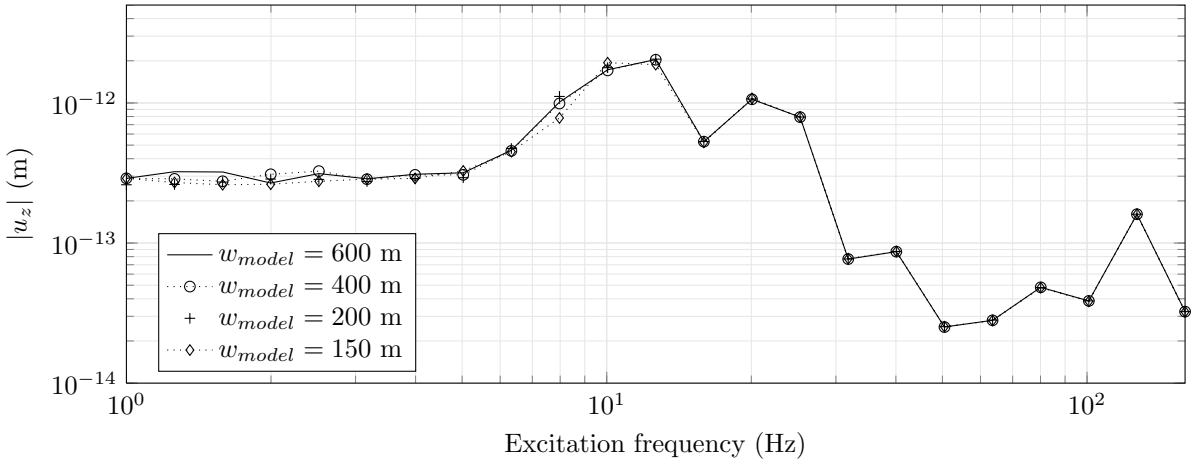

Figure 4.4: *Vertical displacement magnitude response with different model widths, evaluated at 100 meters from the load application point.*

4.1.2 Soil response

Figure 4.5 shows the magnitude of vertical displacements in the soil at different distances from the load application point. At 100 meters most of the content above 30Hz has been dampened out. Two broad peaks can be seen, one between 5-15Hz and one between 17-30Hz. Horizontal displacement response shown in Figure 4.6 is of similar magnitude as the vertical response, 100 meters from the load application point. In Figure 4.7 the vertical displacements from a harmonic load with unit loading at 14Hz is shown. The load is applied at $t = 0$s and the snapshot is taken at $t = 1$s. The largest displacements can be seen close to the surface of the soil, and at point (a) the interaction between the displacements in the soil and those in the bedrock are clearly visible. A video is avaliable at `https://dl.dropbox.com/u/2091759/2013-04-02_soil14Hz.avi`.

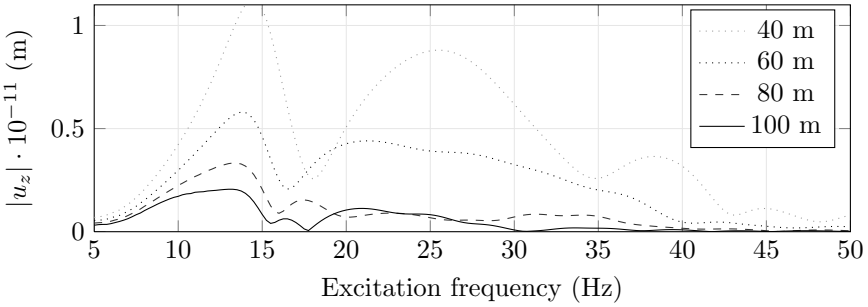

Figure 4.5: *Vertical displacement magnitude response for soil model at different distances from the load application point.*

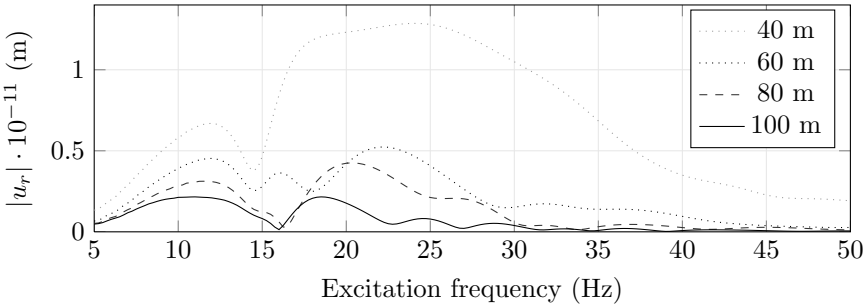

Figure 4.6: *Horizontal displacement magnitude response for soil model at different distances from the load application point.*

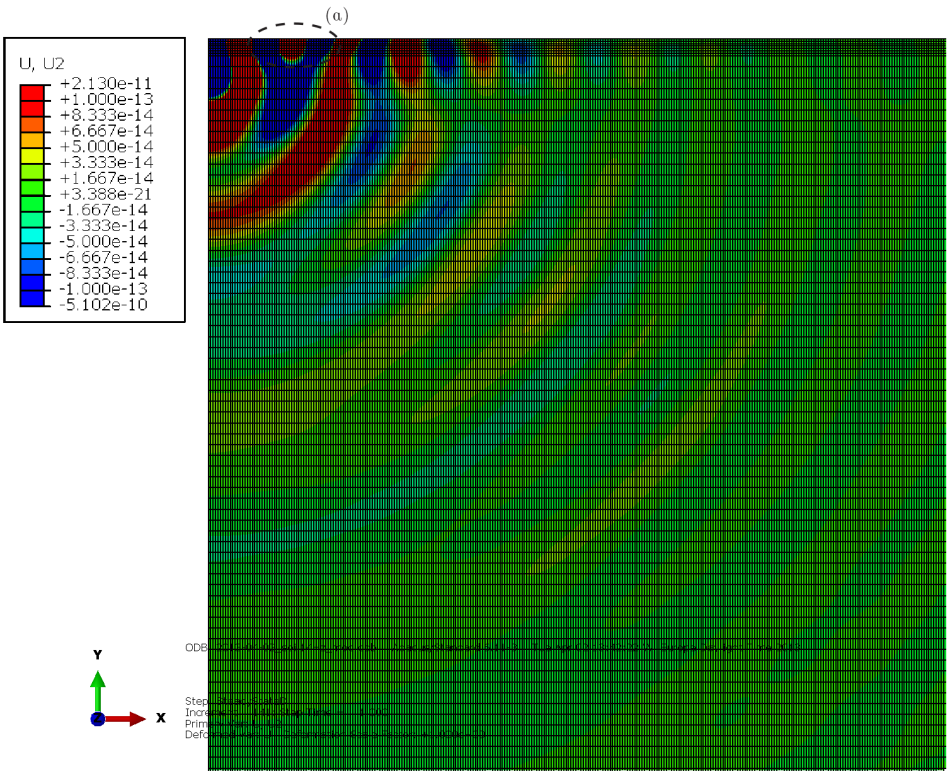

Figure 4.7: *Vertical displacement amplitude of soil model, for a prescribed harmonic load with excitation frequency 14Hz and unit amplitude applied at* $t = 0$. *Picture displays a snapshot at* $t = 1s$. *Contour cut-off limits at* $\pm 1 \cdot 10^{-13} m$.

4.1.3 Model with a single mass

Figure 4.8 shows the AMP_{RMS} values of the vertical displacement magnitude versus density 100 meters from the load application point for a model with a single mass placed 16 meters from the load. Somewhere around 8000-9000kg/m^3 is a local minima for which the RMS value is at 74% of the RMS value for the case with no mass, meaning that there is a 26% improvement in RMS value. For reference the mass density of steel ranges between 7750-8050kg/m^3.

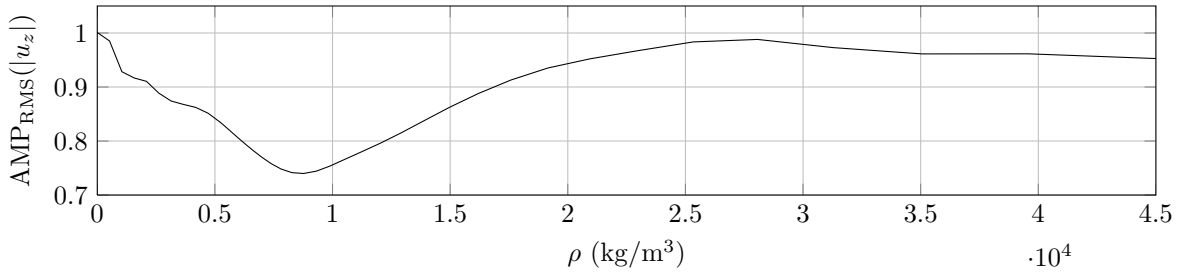

Figure 4.8: AMP_{RMS} *of vertical displacement magnitude response versus density, evaluated 100m from the load application point.*

Figure 4.9 shows the vertical displacement magnitude response 100 meters from the load application point for the soil only model, and for a few models with different mass densities. The model with the mass density $\rho = 8271\text{kg/m}^3$ shows the largest decrease in the frequency range 11-15Hz (compared to the model with no masses), and it doesn't show a increase compared to the soil only model for any part of the frequency range 5-30Hz, however, for larger masses that is not always the case.

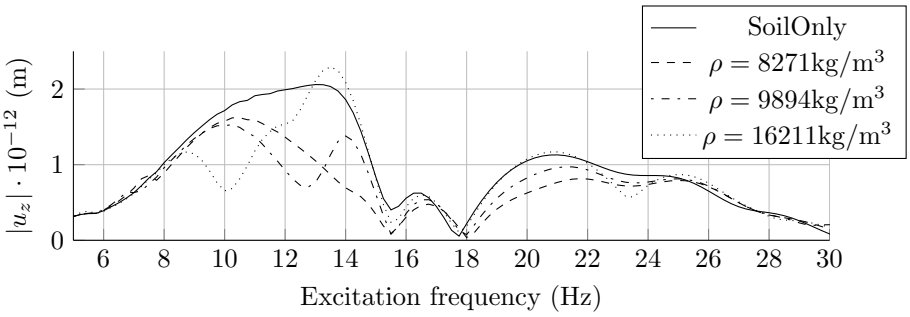

Figure 4.9: *Vertical displacement magnitude response with 3 different densities, evaluated 100m from the load application point.*

Figure 4.10 shows the AMP_{RMS} values of the vertical displacement magnitude along the *r-axis* for a model with mass density 8764 kg/m^3. The mass position is shown with the vertical dotted lines. In front of the mass the RMS values show an increase, and for all positions behind the mass are improvements, however for some higher mass densities RMS values over 1 can be seen for distances greater than 150 meters from the load.

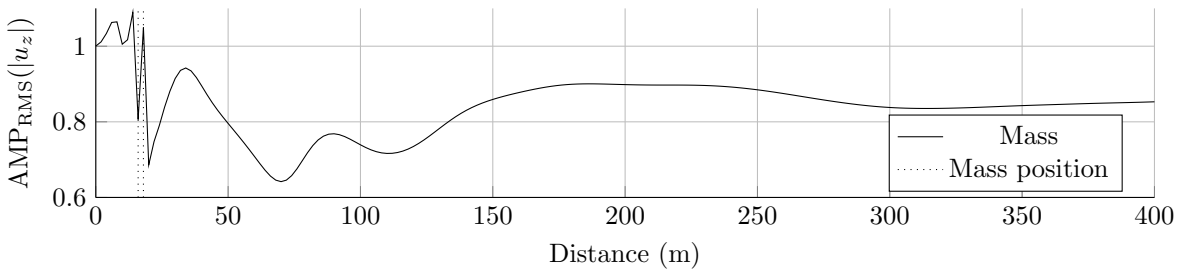

Figure 4.10: AMP_{RMS} *of vertical displacement magnitude response with mass density 8764*kg/m^3*, evaluated along the distance from the load application point.*

Figures 4.11 and 4.12 are the horizontal counterparts to Figures 4.8 and 4.10. The same mass density (around 8000-9000 kg/m^3) shows a reduction of 25% in RMS of horizontal displacement magnitude-. For distances over 140 meters and at 60-70 meters an increase in RMS value is shown for a mass with density 8764kg/m^3. Further on, very light masses show a increase in the RMS value of the horizontal displacement magnitude 100 meters from the load.

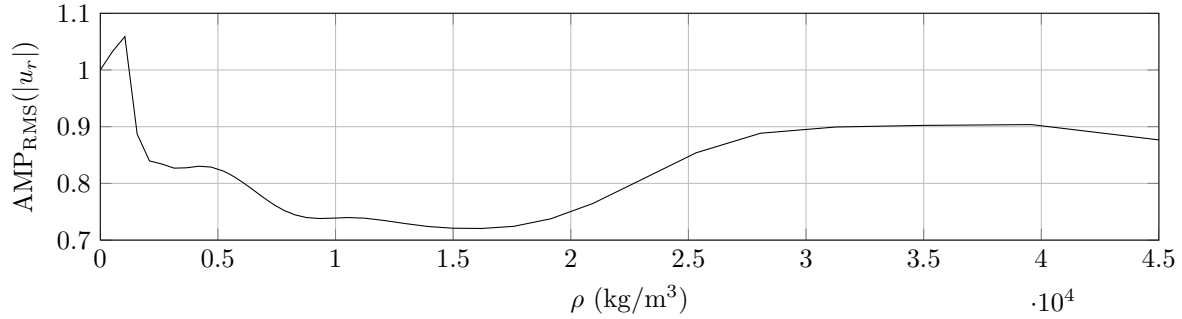

Figure 4.11: $\mathrm{AMP}_{\mathrm{RMS}}$ *of horizontal displacement magnitude response with versus density evaluated 100m from the load application point.*

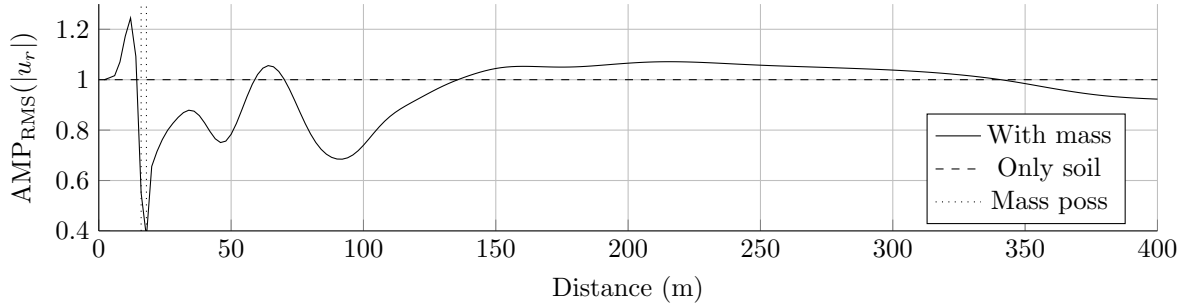

Figure 4.12: $\mathrm{AMP}_{\mathrm{RMS}}$ *of horizontal displacement magnitude response with mass density 8764*kg/m^3*, evaluated along the distance from the load application point.*

Figure 4.13 shows the vertical displacement amplitudes of the soil-mass system with a mass density $\rho = 8271$kg/m^3 positioned 16m from the load application point. The model has been loaded with a unit harmonic load with excitation frequency 14Hz applied at $t = 0$s, with a snapshot at $t = 1$s. The limits on the contour plot are the same as in Figure 4.7 which was for the soil only. Larger displacements can be observed in the bedrock, as predicted in [8] the mass seems to scatter vibrations down into the bedrock. A video is avaliable at `https://dl.dropbox.com/u/2091759/2013-04-02_mass14Hz.avi`.

Figure 4.14 is a close up showing about 150 by 150 meters of both a model with a mass with density $\rho = 8271$kg/m^3 (left) and a model with no mass (right). In the model with the mass larger vertical displacements are observed in the bedrock, and another wave is generated in the soil-bedrock boundary a bit further than 100 meters from the load application point. A video of the close up is available at `https://dl.dropbox.com/u/2091759/Closeup.avi`.

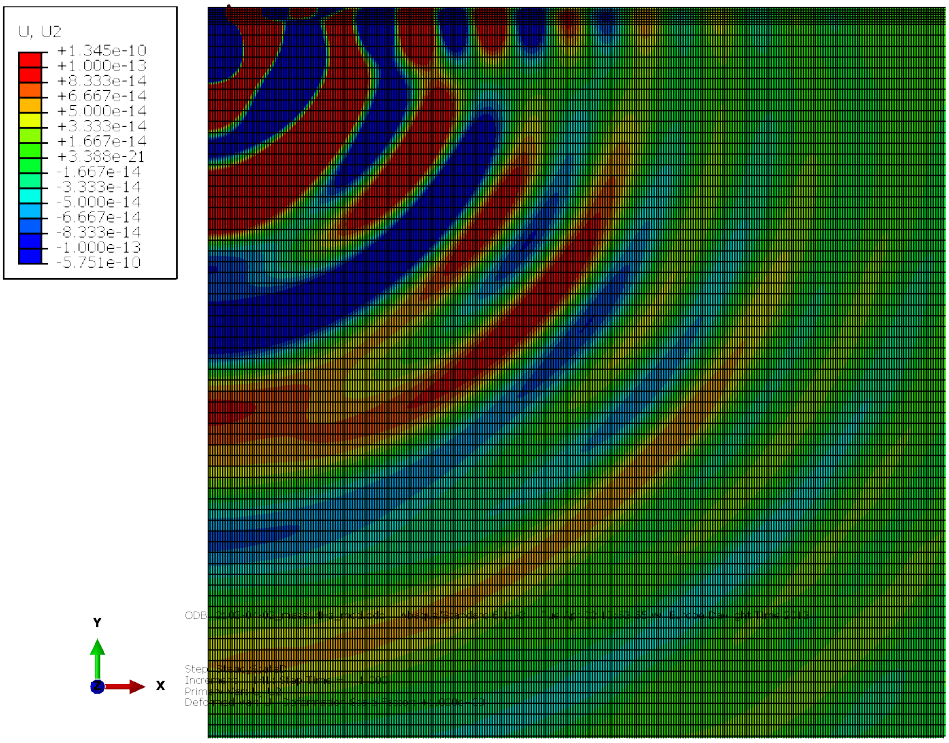

Figure 4.13: *Vertical displacement amplitude of soil model with mass* $\rho = 8271\text{kg/m}^3$*, for a prescribed harmonic load with excitation frequency 14Hz and unit amplitude applied at* $t = 0$*. Picture displays a snapshot at* $t = 1s$*. Contour cut-off limits at* $\pm 1 \cdot 10^{-13} m$*.*

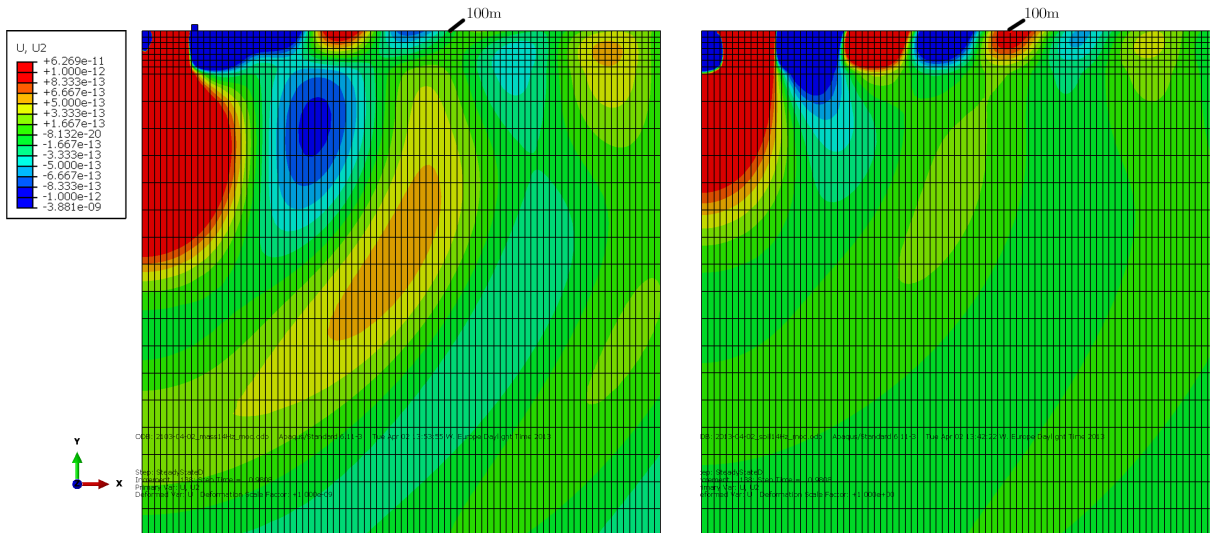

Figure 4.14: *Vertical displacement amplitude of (left) soil model with mass* $\rho = 8271\text{kg/m}^3$ *and (right) model with no mass, for a prescribed harmonic load with excitation frequency 14Hz and unit amplitude applied at* $t = 0$*. Picture displays a snapshot at* $t = 0.98s$*. Contour cut-off limits at* $\pm 1 \cdot 10^{-12} m$*. Close up showing approximately 150 by 150 meters of the models.*

The Young modulus of the mass was varied between that of the upper soil layer (215MPa) to that of steel (210GPa) in 15 steps. The largest improvement in RMS vertical displacement magnitude is for a mass with lowest Young's modulus, as shown in Figure 4.15. Figure 4.16 shows the vertical displacement magnitude response for a mass with density $\rho = 8271\text{kg/m}^3$, plotted for a few different values of the Young modulus. Masses with density $\rho = 8271\text{kg/m}^3$ and higher values for Young's modulus show little effect in the frequency range 17-30Hz.

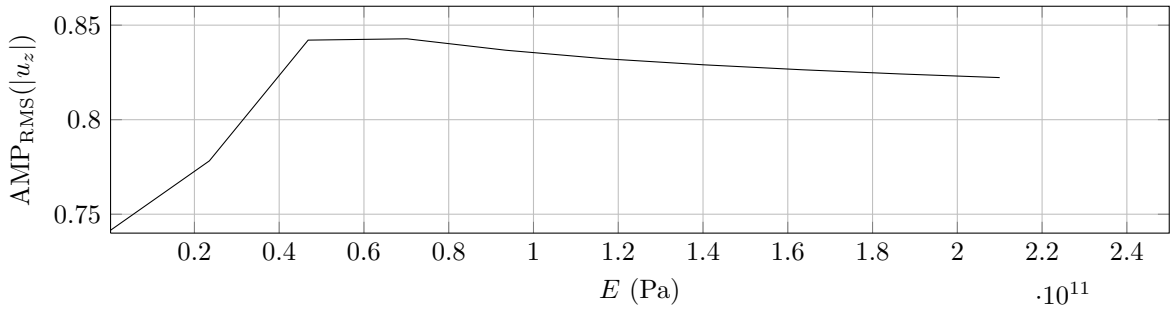

Figure 4.15: AMP_{RMS} *of vertical displacement magnitude response versus Young's modulus, evaluated 100m from the load application point.*

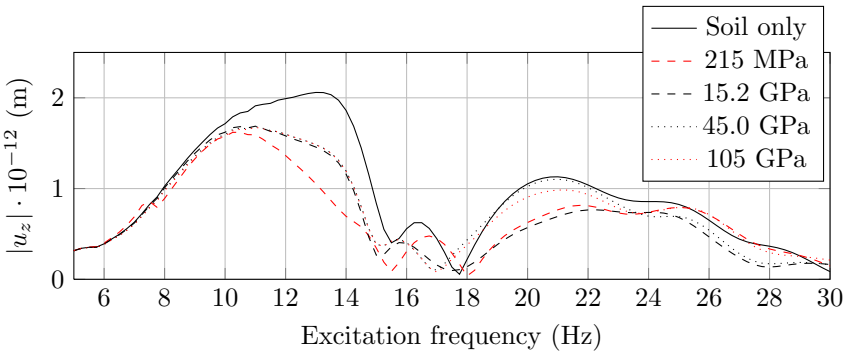

Figure 4.16: *Vertical displacement magnitude response for soil only model, for model with one mass* $\rho_{\text{mass1}} = 8271\text{kg/m}^3$*, and different Young's modulus, evaluated 100m from the load application point.*

The impact of the Poisson's ratio is small, as the largest difference is only 0.5% in RMS value of the vertical displacement magnitude, the AMP_{RMS} of vertical magnitude response is shown in Figure 4.17.

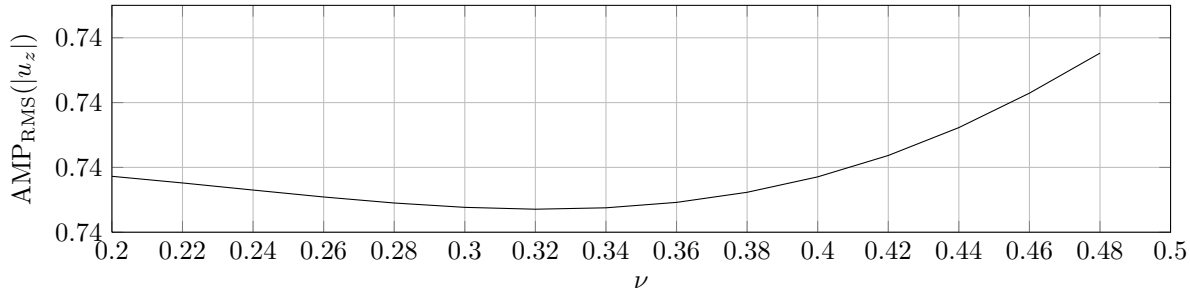

Figure 4.17: AMP_{RMS} *of vertical displacement magnitude response versus Poisson's ratio, evaluated 100m from the load application point.*

Figures 4.18 and 4.19 show the AMP_{RMS} values for vertical displacement magnitude versus position of the mass (r_{mass}), evaluated 100 meters from the load application point and mass density $\rho = 8271\text{kg/m}^3$. The figures are essentially the same except that in Figure 4.18 all values below 8 meters have been cut off in order to better show the differences for larger distances from the load. When the mass is to close the the load an increase in RMS values can be seen, for the case when the mass is right next to the load ($r_{\text{mass}} = 0\text{m}$) the RMS vertical displacement magnitude is almost three times higher. However, further away from the load the results only show improvements, with ideal locations somewhere between 14-32 meters. Figure 4.20 shows the vertical displacement magnitude response for a mass placed 0m from the load application point. At 13Hz the displacements are almost 5 times larger.

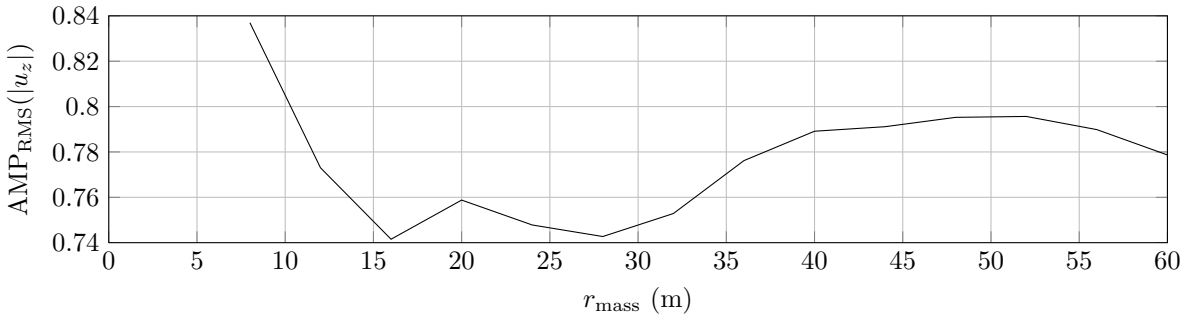

Figure 4.18: AMP_{RMS} *of vertical displacement magnitude response with different mass positions, evaluated 100m from the load application point.*

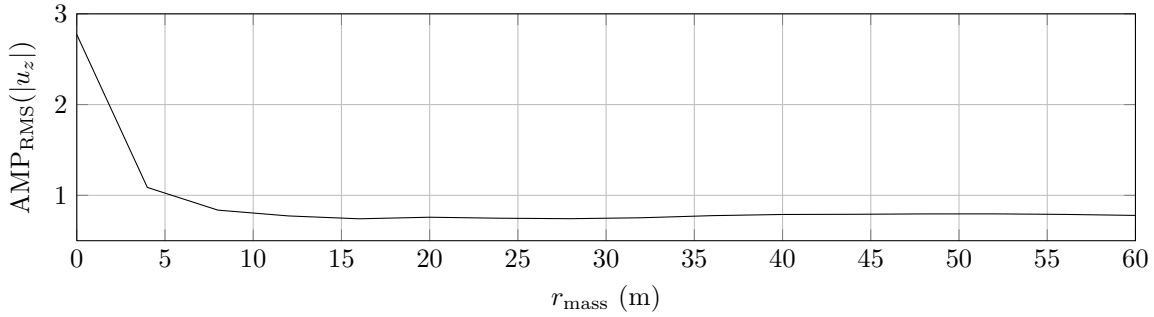

Figure 4.19: AMP_{RMS} *of vertical displacement magnitude response with different mass positions, evaluated 100m from the load application point.*

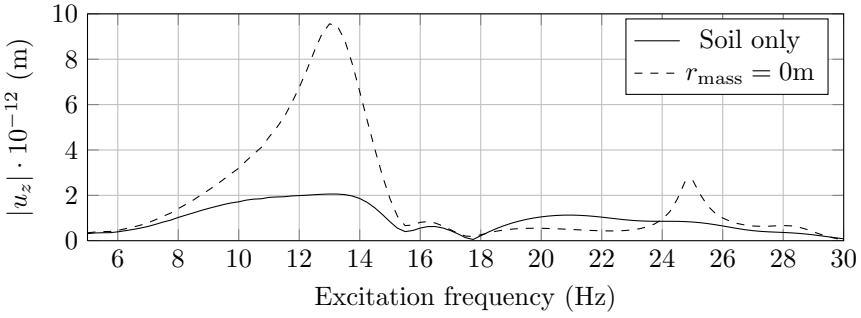

Figure 4.20: *Vertical displacement magnitude response for soil only model, for model with one mass* $\rho_{\text{mass1}} = 8271\text{kg/m}^3$*, and position* $r_{\text{mass}} = 0m$*, evaluated 100m from the load application point.*

The height of the mass was increased in steps of two meters, while the density was adjusted to keep the mass constant, e.g. when the height was doubled from 2m to 4m the density was divided by to going from $\rho = 8271\text{kg/m}^3$ to $\rho = 4135.5\text{kg/m}^3$ and so on. Only a variation of 2% can be seen in the normalized RMS of vertical displacement magnitude.

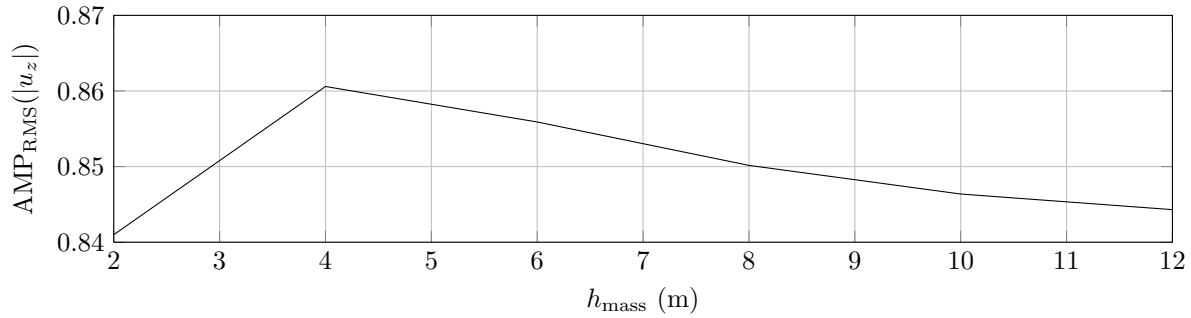

Figure 4.21: AMP_{RMS} *of vertical displacement magnitude response versus height. Density adjusted to keep constant mass* $m \approx 33084\text{kg}$*,* $E = 50\text{GPa}$*, evaluated 100m from the load application point.*

4.1.4 Model with two masses

Two identical masses show a reduction of 36% in RMS vertical displacement magnitude compared to RMS vertical displacement magnitude of the soil only model, if the first is located 16 meters from the load and the second mass is 36 meters away from the first mass, as shown in Figure 4.22.

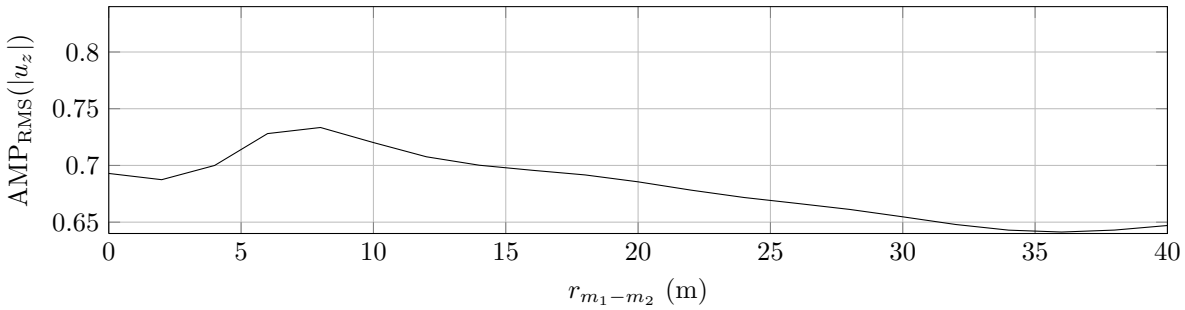

Figure 4.22: $\mathrm{AMP}_{\mathrm{RMS}}$ *of vertical displacement magnitude response with 2 masses both having the density* $\rho = 8271\mathrm{kg/m}^3$*, evaluated 100m from the load application point.*

As shown in Figure 4.23, varying the density of the 2nd mass while keeping the first fixed to $8271\mathrm{kg/m}^3$ can bring the RMS of vertical displacement magnitude further down to 59%. The density for the second mass is ideally in the area between 3000-4000$\mathrm{kg/m}^3$. The lower mass affects the 2nd peak in the 18-30Hz range as seen in Figure 4.24, which shows the vertical displacement magnitude response for a model with one mass positioned 16 meters from the load with density $\rho = 8271\mathrm{kg/m}^3$ and for a model with two masses with the first mass being the same as in the previous model and the second mass positioned $r_{\mathrm{m1-m2}} = 36\mathrm{m}$ and density $\rho = 3333\mathrm{kg/m}^3$.

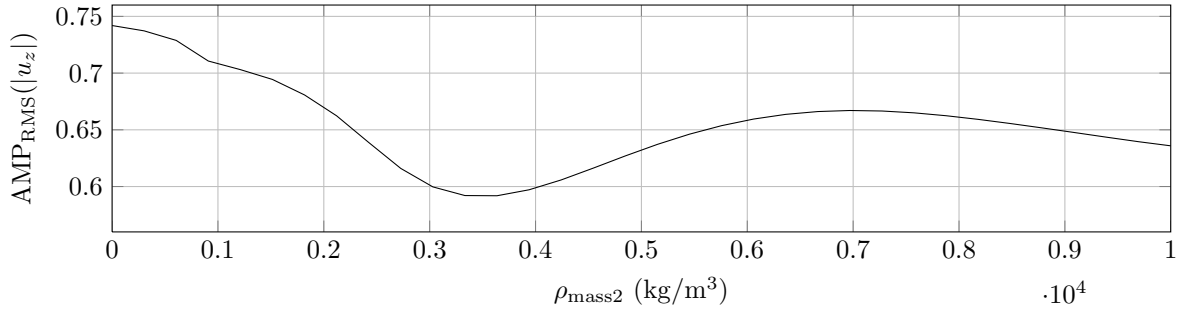

Figure 4.23: $\mathrm{AMP}_{\mathrm{RMS}}$ *of vertical displacement magnitude response versus density of second mass, first mass density* $\rho_{mass1} = 8271\mathrm{kg/m}^3$*, distance between masses* $r_{\mathrm{m1-m2}} = 36\mathrm{m}$*, evaluated 100m from the load application point.*

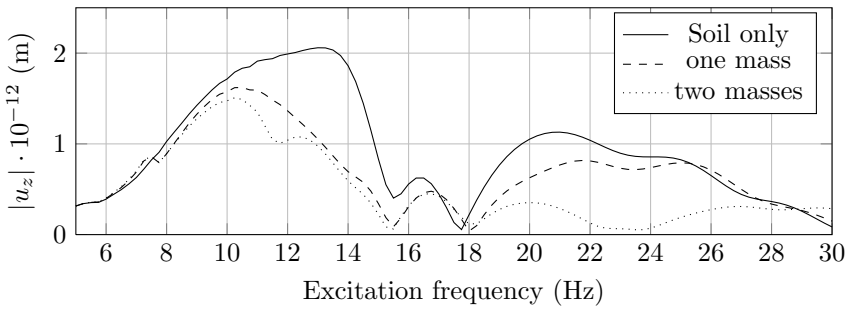

Figure 4.24: *Vertical displacement magnitude response for soil only model, for model with one mass* $\rho_{\mathrm{mass1}} = 8271\mathrm{kg/m}^3$*,* $r_{\mathrm{mass1}} = 16\mathrm{m}$*, for model with two masses where the first mass* $\rho_{\mathrm{mass1}} = 8271\mathrm{kg/m}^3$*,* $r_{\mathrm{mass1}} = 16\mathrm{m}$*, and second mass* $\rho_{\mathrm{m_2}} = 3333\mathrm{kg/m}^3$*,* $r_{\mathrm{m1-m2}} = 36\mathrm{m}$*, evaluated 100m from the load application point.*

4.1.5 Model with a simple building

In Figure 4.25 it is shown that a simple building with 5 floors shows the most decrease in $\mathrm{AMP}_{\mathrm{RMS}}$ of vertical displacement magnitude. From figures 4.26 and 4.27 one can see that the frequency response shows a large reduction around 14Hz compared to the model with no building. From the snapshot taken at $t = 1$s in Figure 4.28 and time history in Figure 4.29 it is seen that the vertical motion of the two sides of the building is out of phase with each other, the model has in this case been loaded with a harmonic load with excitation frequency 14Hz and unit loading.

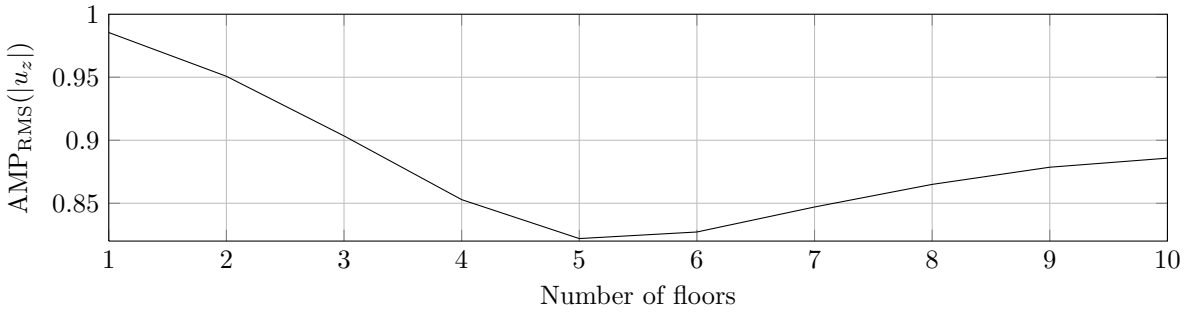

Figure 4.25: $\mathrm{AMP}_{\mathrm{RMS}}$ *of vertical displacement magnitude response versus number of floors, evaluated 100m from the load application point.*

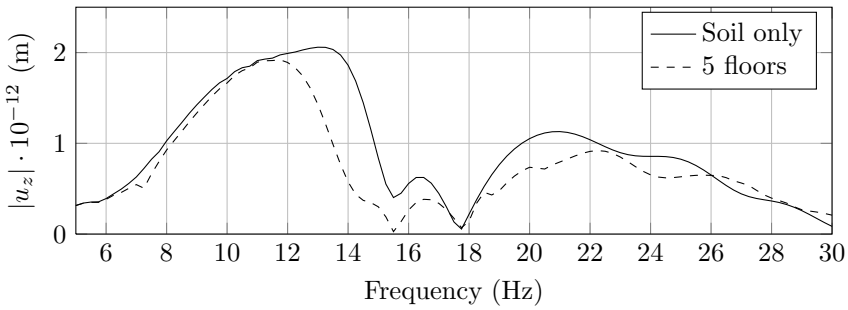

Figure 4.26: *Vertical displacement magnitude response for model with 5 floors, evaluated 100m from the load application point.*

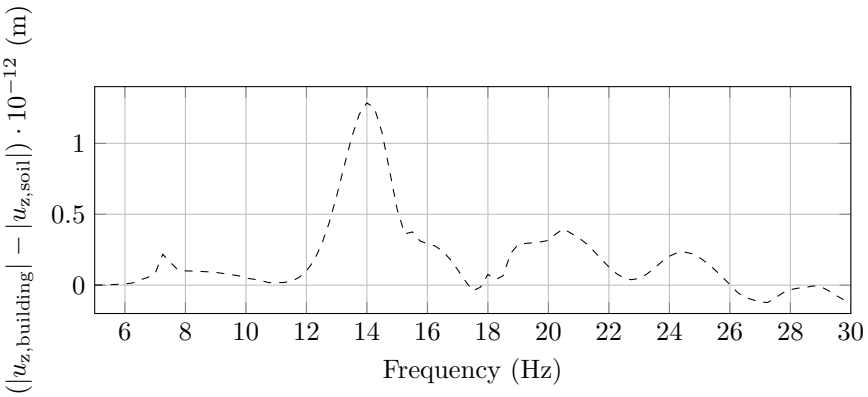

Figure 4.27: *Difference in vertical displacement magnitude response between soil only and model with 5 floors from Figure 4.26, evaluated 100 m from load.*

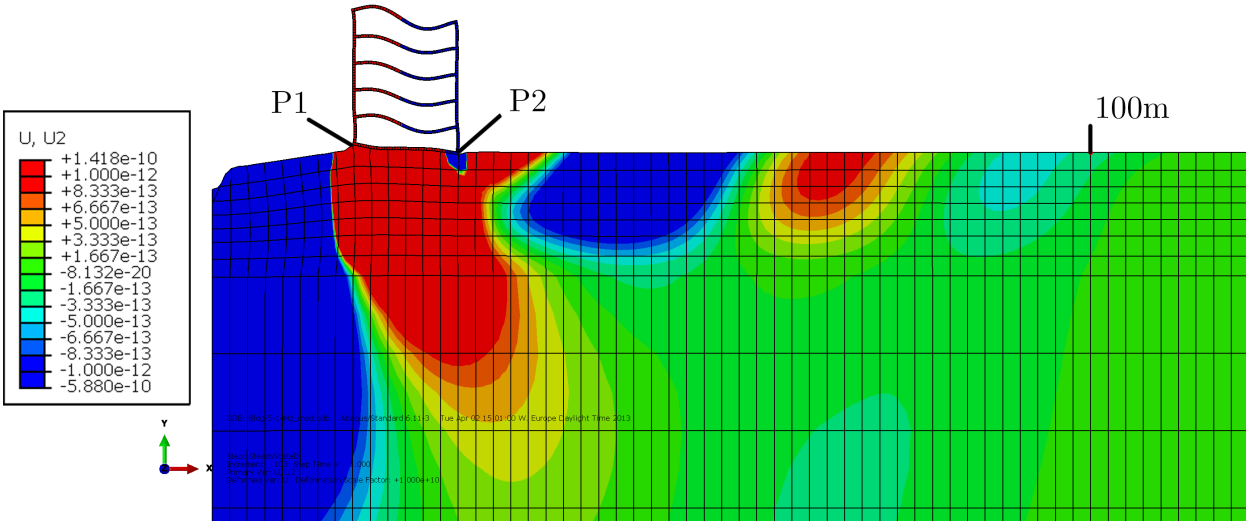

Figure 4.28: *Vertical displacements of soil model with 5 floor building, for a prescribed harmonic load with excitation frequency 14Hz and unit amplitude applied at* $t = 0$. *Picture displays a snapshot at* $t = 1s$. *Contour cut-off limits at* $\pm 1 \cdot 10^{-12} m$.

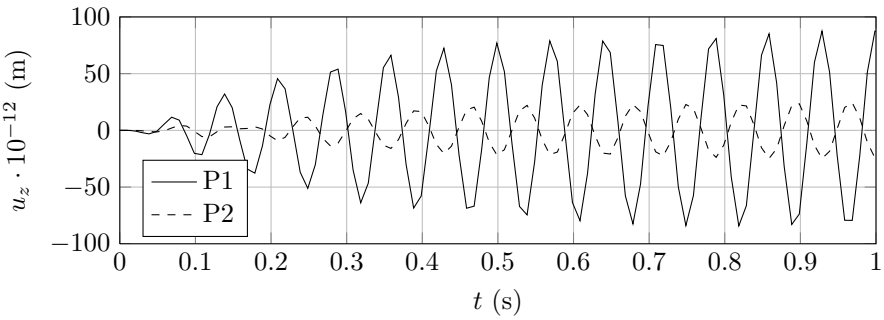

Figure 4.29: *Vertical displacement time history for model with 5 floors, for a prescribed harmonic load with excitation frequency 14Hz and unit amplitude applied at* $t = 0s$, *evaluated at soil contact positions shown in Figure 4.28.*

4.1.6 Soil freezing

It was of interest to find out how the freezing of the soil would effect the vibration reduction of the masses. The frost line in the south of Sweden is at 1.1m, which is how deep the soil freezes due to seasonal variations in temperature. To model this the first meter (in z-direction) of the upper soil layer Young's modulus was doubled to 430MPa. Figure 4.30 shows the vertical displacement magnitude response of the normal and the frozen soil models, 100 meters from the load application point. The penetration depth of a Rayleigh wave is dependent on its wavelength [2], and in Figure 4.30 it is seen that change in response is observed at frequencies over 15Hz, where wavelengths and penetration depths are smaller, allowing the frozen layer to have more effect. Figure 4.31 shows the vertical magnitude displacement response of the frozen soil, and of the frozen soil with a mass at distance 16 meters from the load application point and density 8271kg/m^3, evaluated 100 meters from the load application point. $\mathrm{AMP}_{\mathrm{RMS}}(|u_z|)$ for the specific example is 73.1%.

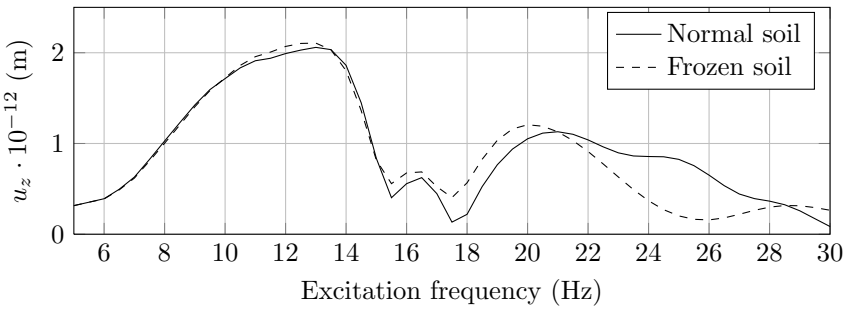

Figure 4.30: *Vertical displacement magnitude response with soil only model, and with frozen soil only model, evaluated 100m from the load application point.*

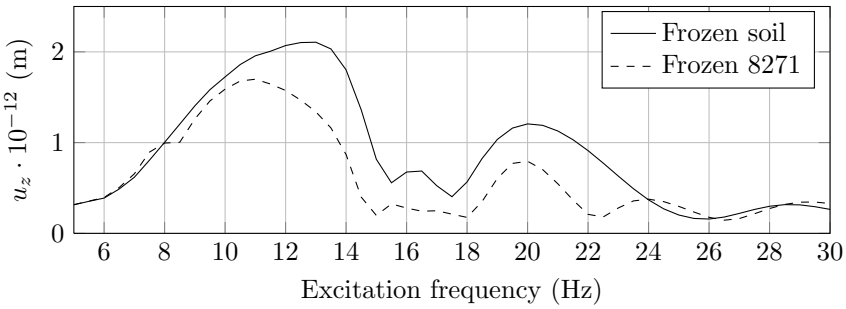

Figure 4.31: *Vertical displacement magnitude response with frozen soil only model, and with a mass* $\rho = 8271\mathrm{kg/m}^3$ $r_{mass} = 16\mathrm{m}$*, evaluated 100m from the load application point.*

4.2 3D FE-Model results

4.2.1 Comparison of soil-only results to 2D-axisymmetric case

Since 3D models quickly grow in size and computational costs a smallest possible model was based on the convergence results of the 2D studies. Figure 4.32 shows the vertical displacement magnitude results 100 meters from the load application point for the 2D, and 3D models with only the soil model and no added masses. The highest peak in the 3D results is slightly lower than that of the 2D result. The frequency steps of 2Hz don't manage to capture the small peak in the 15-17Hz area.

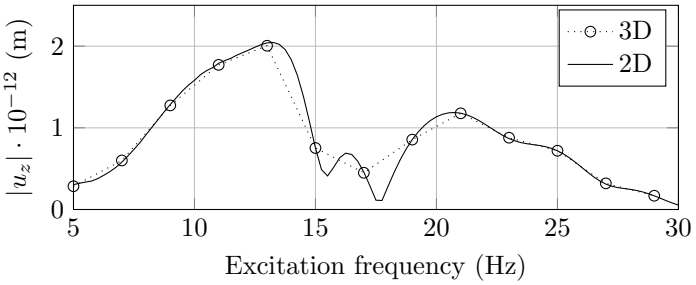

Figure 4.32: *Vertical displacement magnitude response for 2D and 3D models, evaluated 100m from the load application point.*

A few different sets of the Rayleigh damping parameters were considered, Figure 4.33 shows the results from the best fit. The Rayleigh and structural damping models differed 3.7% in RMS vertical displacement magnitude response, but the general behaviour was the same and considered good enough for the study.

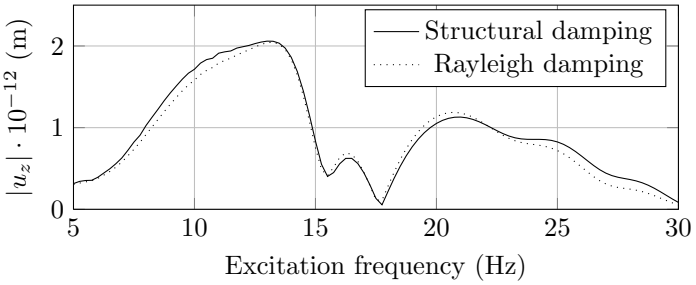

Figure 4.33: *Vertical displacement magnitude response for 2D model with structural and Rayleigh damping, evaluated 100 meters from the load application point.*

4.2.2 Traffic load

Figure 4.34 shows the results of the 3D soil model with no masses in place and a unit load, and a version with results with load scaling, which can be seen to mainly have an effect on frequencies lower than 13Hz.

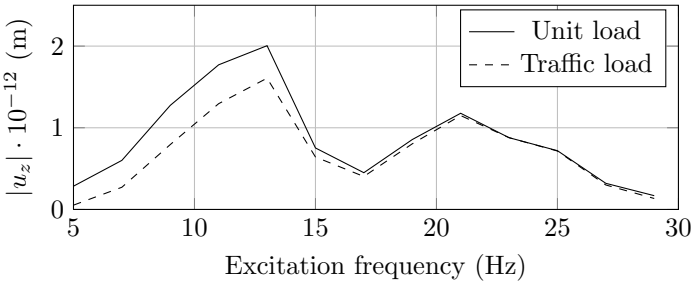

Figure 4.34: *Vertical displacement magnitude response for 3D model with unit load and normalized traffic load, evaluated 100 meters from the load application point.*

4.2.3 3D Results

The 3D results are presented in Appendix A, and a few figures of particular interest are presented along with the text. In general most results provide a decrease in RMS-values of the vertical displacement magnitude 100 meters from the load compared to those of the model with soil only, except for in a few cases for the pattern groups referred to as *diagonals* and *free form*. The ones that lead to increases in RMS of vertical displacement magnitude had the property of being continuous in either 1 or 2 dimensions and all of these lead to decreases once the free form patterns had been divided into smaller discontinuous masses. Figure 4.35 shows the categories of the different types of patterns for which the results are presented in this chapter.

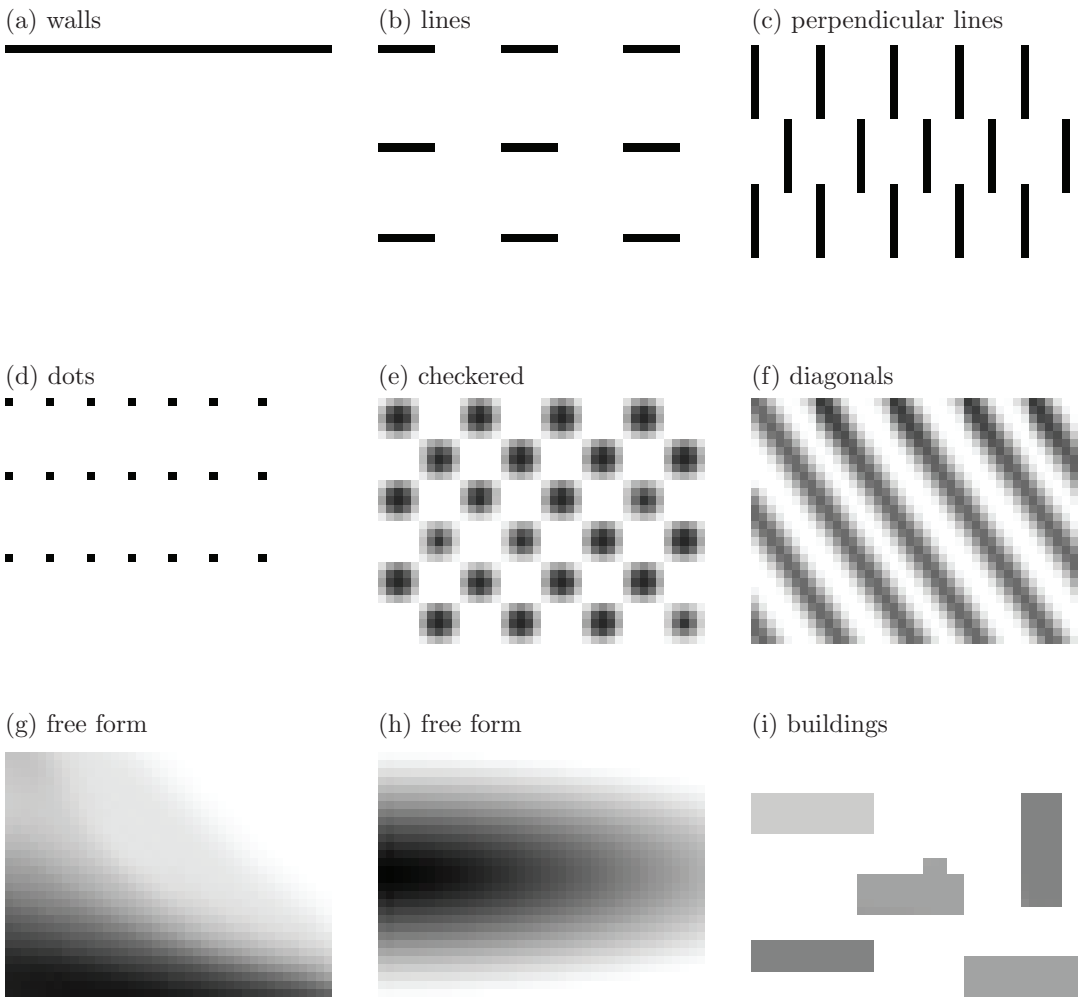

Figure 4.35: *Different types of patterns used in 3D simulations.*

As all of the 3D results are presented in the same manner with a two by three grid a brief explanation will follow, based on Figure 4.36. The upper left plot shows the configuration of the masses, with 100% black meaning a mass with density $\rho_{\max} = 8271\text{kg/m}^3$ and 0% black meaning no mass, with densities varied linearly between the two values. If two masses are placed next to each other they are assembled together and considered as one (though their densities may be different). The orientation of the plot is such that x points downwards and y points to the right, meaning that the load application point is slightly above the plot, and the main evaluation points at $x = 100\text{m}$ are at the bottom. The upper middle plot shows the AMP_{RMS} values for the vertical displacement magnitude response, and the lower left plot shows the AMP_{RMS} values for the vertical displacement magnitude response along the x-axis going from the load application point to the main evaluation point (note that information is missing for $x \in (0:20)(80:100)$). These two plots have mainly been used

for verification purposes of the 3D-model. The upper right grid element shows the material properties of the used masses. The bottom middle plot shows the AMP_{RMS} values of the vertical displacement magnitude response along the y-axis at $x = 100$m, which is the main area of interest. The lower right plot is the vertical displacement magnitude response at $x = 100$m, $y = 0$m, the point which is 100 meters away from the load application point.

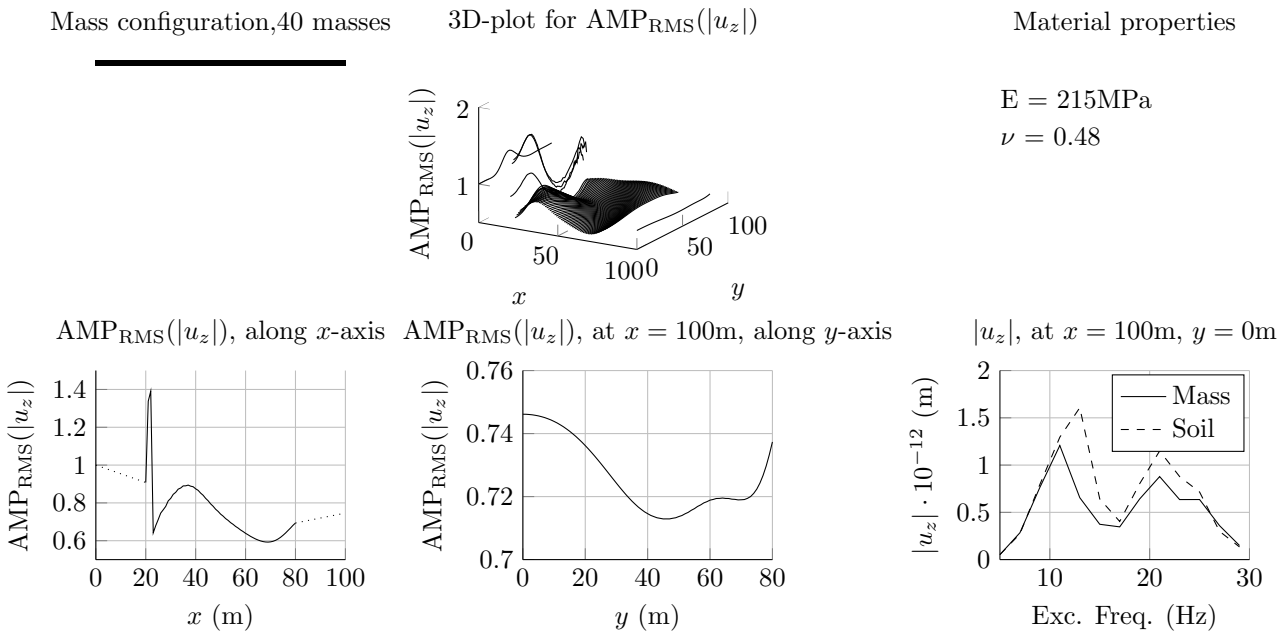

Figure 4.36: *3D results for wall-1, the case which is most similar to the 2D axisymmetric simulations. (Top left) Organization of masses. (Top middle) 3D-plot of RMS amplification of vertical displacement magnitude. (Top right) Mass properties. (Bottom left) RMS amplificiation of vertical displacement magnitude along x-axis. (Bottom middle) RMS amplificiation of vertical displacement magnitude along y-axis, 100 meters from the load application point. (Bottom right) Vertical displacement magnitude response at $x = 100m$, $y = 0m$.*

A model with a line of masses along y-direction placed as close to the load as possible (20 meters away) was the first test that was done. It is the closest match to the 2D axisymmetric model with a single mass and the AMP_{RMS}-value of vertical displacement magnitude at $x = 100$m, $y = 0$ for the 3D test with no load scaling is 76.5%, whereas the 2D is 76%, note also that the vertical displacement magnitude response in Figure 4.36 (bottom right) is similar to that of the 2D case in Figure 4.9. The AMP_{RMS} vertical displacement magnitude plot along the x-axis shows the same sinusoidal behaviour behind the mass as the 2D case in Figure 4.10, and in the 3D-plot of the AMP_{RMS} vertical displacement magnitude it is visible that the pattern is circular with the centre located somewhere near where the load is, suggesting that it is a result of how the vertical displacement magnitude response in the soil only model is changing with the distance from the load, making the applied masses more effective for some distances and less for others. In Figure 4.36 (bottom middle) we can see that the improvement in $\text{AMP}_{\text{RMS}}(|u_z|)$ is relatively even along the y-axis, showing only a difference of 0.04.

As the locations of the load and main evaluation point in the model are well known it is possible to reduce over 20% in RMS of the vertical displacement magnitude at $x = 100$m, $y = 0$ by placing a smaller object close to the load application point, as in Figure A.1, however, going to the extreme by trying out a single two by two meter mass (Figure A.9) has very little effect, as up to 96% in RMS of vertical displacements remains 100 meters from the load. Both of these attempts with fewer masses are a bit less effective than the model with a whole line, however, they use a fifth of the material.

Figures A.2 to A.5 are simulations with walls that are four times as thick as the one in Figure 4.36, meaning a width of eight meters instead of two. They vary in density by 100%, 75%, 50% and 25% of $\rho_{max} = 8271\text{kg/m}^3$. The test with 100% density has slightly less reduction of RMS vertical displacements 100 meters from the load application point than that of Figure 4.36, even though it is four times as thick. Using slightly lighter masses (75% of ρ_{max}) the RMS vertical displacement is brought down to 63% of that for the model with soil only.

Figures A.7 and A.8 show four walls placed 16 meters apart from each other and varying density in the first case per wall, and in the second as sinusoidal functions. They show similar performance in RMS vertical displacement 100 meters from the load, and in the vertical displacement magnitude response for most of the frequency range.

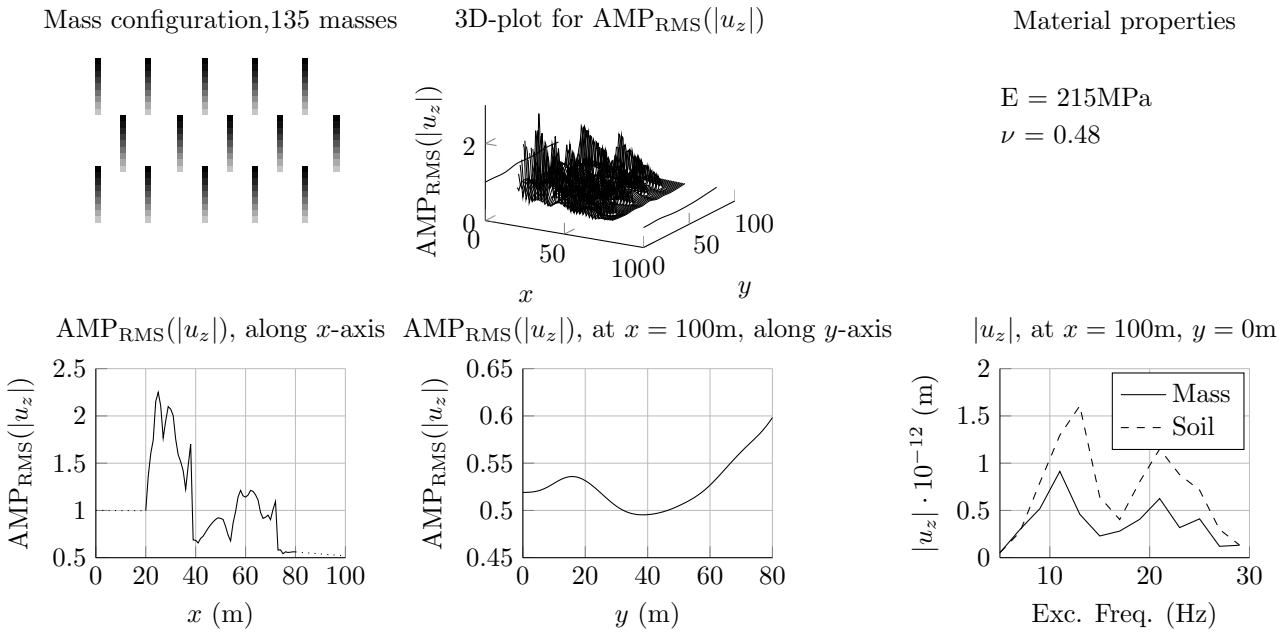

Figure 4.37: *3D results for perpendicular-3, with linear gradients applied to the masses. (Top left) Organization of masses. (Top middle) 3D-plot of RMS amplification of vertical displacement magnitude. (Top right) Mass properties. (Bottom left) RMS amplificiation of vertical displacement magnitude along x-axis. (Bottom middle) RMS amplificiation of vertical displacement magnitude along y-axis, 100 meters from the load application point. (Bottom right) Vertical displacement magnitude response at $x = 100m$, $y = 0m$.*

Figures A.14 to A.16 are of perpendicular walls. Figure A.15 has densities 100%, 66% and 33% of $\rho_{max} = 8271\mathrm{kg/m}^3$ applied, and shows three distinct peaks in the vertical displacement magnitude response plot (Figure A.15 Bottom right). Figure 4.37, with a smooth gradient applied to each line shows a more even reduction in the vertical displacement magnitude response at $x = 100$m, $y = 0$m and almost 50% reduction in RMS of vertical displacement magnitude compared to the soil only model, 100 meters from the load application point. Increasing the stiffness leads to less reduction in RMS and has little or negative effect in vertical displacement magnitude response for frequencies lower than 17Hz, as shown in Figure A.16.

Lines as seen in Figures A.10 to A.12 almost perform as well as walls for some parts of the RMS of vertical displacement magnitude along the y-axis 100 meters from the load. The RMS reduction is largest for $y < 10$m, and less reduction is seen for increasing distances in y. Comparing Figure A.10 to Figure A.11 is one of the few cases where the varied density (Figure A.11) does not lead to larger reduction in RMS of vertical displacement magnitude. The versions with lines are sensitive to the load location, Figure A.13 shows the same pattern as Figure A.10, but offset eight meters in y-direction so that there are no masses straight in front of the load, there is only 5% reduction in RMS vertical displacement magnitude at $x = 100$, $y = 0$m, unlike figure A.10 which has a reduction of 45% at the same point.

Figures A.17 to A.19 show the effect of arrays of masses. Any substantial reduction in RMS of vertical displacement magnitude is first seen when the dimensions are increased from two by two meters to four by four meters for the individual masses, as shown in Figure A.19. The two by two meter arrays show a reduction of about 10% 100 meters from the load application point, while the four by four meter arrays show a reduction of about 30% at that distance.

Figures A.20 to A.22 are for checkered patterns, and depending on density show very high reductions in RMS of vertical displacement magnitude 100 meters from the load application point. Unless using heavy masses the performance is similar in RMS of vertical displacement magnitude to other solutions which use

fewer masses, e.g. Figure A.21 versus Figure 4.37 which use 135 and 600 two by two masses respectively, but show similar values of reduction in RMS along the y-axis 100 meters from the load.

Some peculiar effects can be seen when all of the masses are connected in either one (when one direction it has to be different from the y-axis) or both directions, namely that the masses may act in ways which could potentially amplify the RMS of vertical displacements at some locations. Fig A.24 shows a set of diagonals consisting of connected masses with different densities which at show an increase in RMS-value at the end of the AMP_{RMS} along the y-axis, the point which the line-masses are "pointing" at. Figure A.29 shows almost a doubling of RMS-value while the same pattern (Figure A.30) divided into smaller masses instead gives an improvement of 36%. The patterns in these test have a density distribution which effectively guides the incoming waves towards the evaluation point, as shown in Figure 4.38 which is a snatpshot of the organization from Figure A.26. For the snapshot a unit harmonic load with excitation frequency 14Hz was applied at $t = 0$s, and the snapshot is taken at $t = 0.35$s.

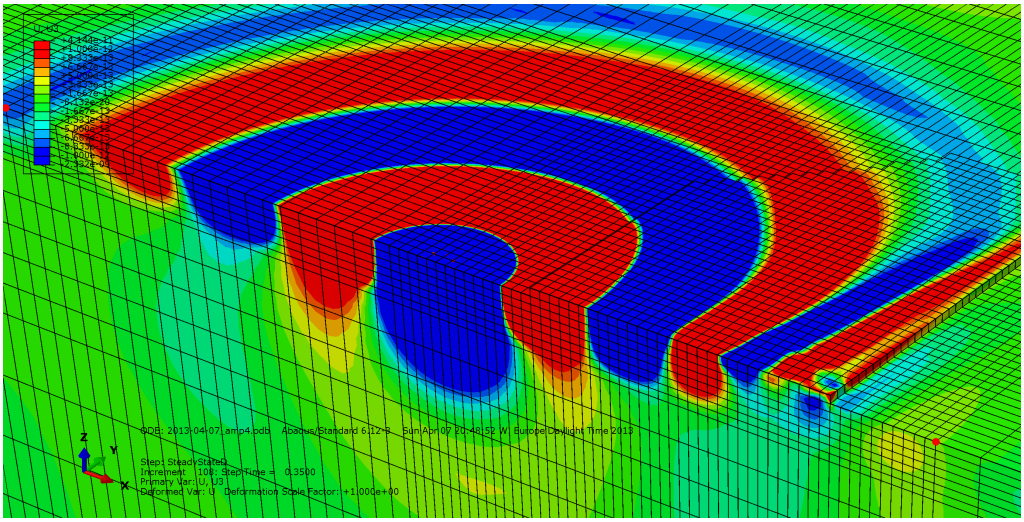

Figure 4.38: *Vertical displacements of soil model with with the mass pattern from Figure A.26, waves are guided towards evaluation point. Transient analysis with a prescribed harmonic load with excitation frequency 14Hz and unit amplitude applied at $t = 0s$, snapshot at $t = 0.35s$. Contour cut-off limits at $\pm 1 \cdot 10^{-12} m$.*

Figures A.33 to A.37 are of masses in patterns which are similar in dimensions as the footprint of buildings. They were run with a higher value for the Young modulus and showed reductions in RMS of vertical displacement magnitude with lighter masses as well, as seen in Figure A.34. Of note is Figure A.37 where the masses are organized in a direction along the load application point to the main evaluation point, that is, along the x-axis. Such an organization shows an increase in RMS of vertical displacement magnitude of 50% at $x = 100$m $y = 0$m, which seems to suggest that the masses in this pattern are guiding the waves along the direction of their long side, in a similar fashion to Figure A.24.

Figures A.35 to A.36 are simulations with a part of the building plan from the architectural thesis, marked in Figure 4.39. A few different parts were tried, but the 3D steady-state model was too small to try the whole plan at once. No parts of those that were tried showed an increase in RMS of vertical displacement magnitude.

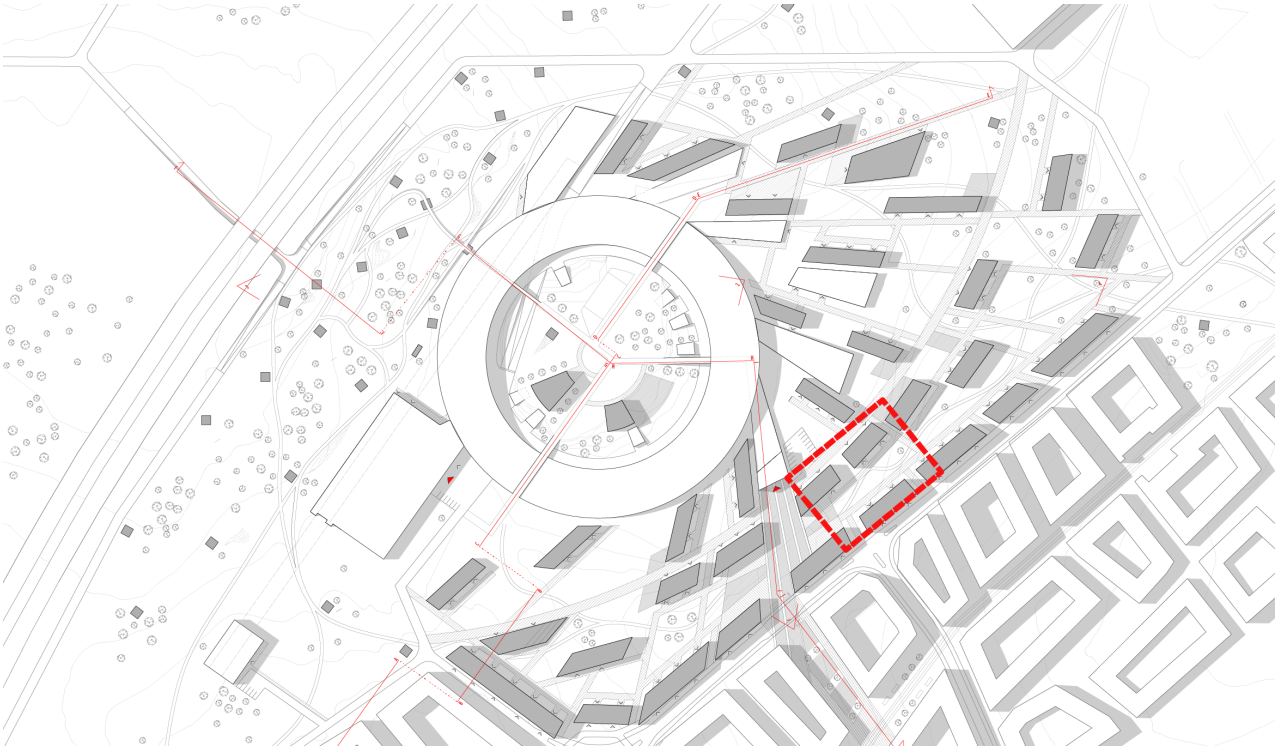

Figure 4.39: *Plan from architectural master's thesis, 80 by 60 meter part that was used in Figure A.35 marked in red. [1]*

4.3 Scale model results

Some preliminary tests with the scale material had good scale on wavelengths, as can be seen in Video 1 `https://dl.dropbox.com/u/2091759/VibrationJello.mp4`. The problem was that the JELL-O materials were to weak and could not support any heavier objects on top while being vibrated. Figure 4.40 shows the sunken masses in the JELL-O. Because of this limitation in the material the scale model was abandoned. Substitute materials were searched for but they were either to stiff (attempts were done with bentonite-clay), or as in some very promising dual-network hydrogels contained hazardous ingredients and complicated methods for preparation [17], and were in the end disregarded.

Figure 4.40: *The sunken masses in the physical model*

5 Discussion

5.1 Conclusions and discussion

5.1.1 2D

From the 2D axisymmetric simulations we can reach the following conclusions:

- The density of the mass is the most important factor for its effectiveness in mitigating vibrations. Masses needed in the case studied in this thesis are very heavy.
- Horizontal vibrations have not been studied in detail, but the included parts show that all masses except very light ones show an improvement 100 meters from the load.
- The mass seems to increase the amplitude of the vibrations in the bedrock, considering that the bedrock has much less damping than the soil this could lead to vibrations which can propagate for longer distances, and is observed in Figure 4.12
- Increasing the Young modulus of the masses/buildings has negative effect on the vibration reduction, a clear relationship as to why is not explained but it could possibly be a increase in resonant frequencies of the mass-soil system, removing secondary effects within the 5-30Hz frequency range, as in Figure 4.16.
- The Poisson's ratio seems to have a small impact.
- The height of the mass has little impact on the performance, meaning that density and height can be played with to achieve the necessary mass per unit ground area. However, the analysis was taken in steps of two meters and there may exist possibilities of other vibration modes of the mass being missed in the analysis. The analysis was carried out for stiffer masses as larger geometries would require a construction material which is stiffer than the soil.
- The position of the mass can be seen as the second most important factor simply because having it too close to the load can, in the case of this thesis, increase RMS vibrations by three times. The same issue may arise if the mass is for some other reason excited at a frequency close to the mass-soil systems resonant frequency. Ideal position for the mass is somewhere between 14-36 meters, which is still relatively close to the load.
- Working with two masses can further improve vibration mitigation, with the second mass being lighter and preferably providing reduction in the 18-30 Hz frequency range.
- When the soil freezes the masses are still able to reduce vibrations. The main change in response is in higher frequencies where the Rayleigh wave penetration depth is smaller meaning the influence of the frozen upper layer is larger. The frost depth of one meter can be considered conservative, as measurements on site have shown that it is only about 0.3 meter, which in effect should leave little to no change in response. Of more concern would be how the frozen soil would affect the traffic load, but it is not something that has been treated in this thesis.
- Although the most effective building shows similar response in the vertical displacement magnitude response as the most effective masses it does not behave in the same manner. While the mass moves in a rigid body mode the two main walls of the building are moving out of phase of each other, and if buildings are to be used they need to be studied much more in detail.

In general the results from the 2D simulations show that masses on the ground may be used for vibration mitigation, as long as they are not in vicinity to the load, and there is no other source of excitation which may cause the mass-soil system to vibrate. The masses are however very heavy. In the case of using buildings issues may arise if the building gets excited by the wind in such a way that the excitation may cause vibrations in the ground. The same care must be taken for the intended use of the building as any kind of heavy machinery with harmonic motions could induce vibrations in the ground. As some of the studies show even lighter buildings have some positive effect and could be designed in a way so that their resonant frequencies are not the same as those for the soil, but this has not been part of the study.

In the Figure 4.14 it is seen that the masses lead to more vibrations in the bedrock, which together with the fact that the bedrock has less damping than the soil could be an explanation for why for distances of more than a 100 meters from the load sometimes show an increase in AMP_{RMS} of vertical displacement magnitude.

Some assumptions have been made in the study to simplify analysis, full contact has been assumed between the mass and the soil, the soil and bedrock layers have been assumed to be entirely flat, and no damping has been used in the added masses. As there have been geological measurements on many places at the site which show similar dimensions to the soil and bedrock the first assumption seems plausible. No attempts have been made to verify the other two assumptions.

5.1.2 3D

From the 3D simulations it is more difficult to draw general conclusions but the following can be concluded:

- Different organizations of masses have different effectiveness on mitigating vibrations, however all *discrete* organizations of masses show improvements in vertical displacement magnitude, but may show increases in vertical displacement magnitude response for some frequencies and reductions for others.
- A variation in mass densities generally leads to a more even reduction of vertical displacement magnitude response, however, it is difficult to improve the response for excitations at frequencies lower than 11Hz.
- Since the position of the load and main evaluation points are well known it is possible to reduce vibrations with very little means, for example Figure A.1 shows 20% reduction 100 meters from the load application point by using just seven masses. This, however, is of little use in general, since the vibrations may come from any part of the road, but if the case is such that there is some part of the road which is worse than the rest it is possible to do something about it locally.
- In the cases where the masses are connected in either one, or two dimensions they may lead to amplifications. It is possible to focus vibrations to a point by organizing masses as a lens, however discretizing the masses so that they are not continuous over the whole area leads to solutions which only show improvements in vibration levels.
- Using lenses which deflect the waves away from the evaluation points has been tested, but is of little practical value since it works well for a stationary harmonic load, but in reality there is a whole line (the road) along which vibrations may propagate from.
- In the cases where the masses are only connected in one dimension the vibrations are focused along with the direction of them masses, meaning a direction for the masses which is perpendicular to the direction of the load and evaluation point may be used as a solution.

For the tests that were done to compare the 3D model to the 2D model the results were agreeable between the models. Switching method of damping from structural to Rayleigh was something which could have been avoided but it simplified the work and the results were still good enough for a comparison study between different organizations of masses. The same could be concluded about using a smaller model in the 3D case, and in hindsight it would have been good to seen exactly where a 4x4 meter mesh size diverges from a 2x2 meter as such a change in the model would have made it a much smaller computational load and allowed for staying within *ABAQUS*. The benefit from switching to *MATLAB* was not only the dynamic model reduction, but the built in routines allowed for a simple way to sketch out masses on a graphical file and simply import it and use it to assemble masses *MATLAB*. Similar scripting was later done in *ABAQUS* but each mass required own definitions for part, material, section, and so on, which worked but was a bit inconvenient.

What is a bit more of a concern of the 3D model is the 2Hz steps, as can be seen in Figure 4.27 is that the main area of effect for the mass (building in this specific case) is only 2-3Hz wide, meaning that the resolution may be a bit too course and potentially miss some peaks. Going to 1Hz would mean a doubling of computational costs and in most cases the model seemed to work well, atleast for conceptual research.

The simulations with the checkered organizations show remarkably good reduction of RMS values, but are on the other hand very heavy and would consume a lot of material, which may require some sort of foundation to rest on if the soil is not strong enough.

The architectural thesis started in an environment where some sort of wave propagation studies could be done, and this thesis ends at the same place, though with a constraint in size of the model which does not allow for the testing of the whole architectural plan at once, or for that matter any sophisticated mechanical

models of the buildings as it is so far limited to variation of stiffness and density of two by two meter masses. However, with the use of the 3D model, and some insights from the studies in 2D (mainly what to look out for) we may conclude that the architectural proposal could at the very least be feasible.

5.1.3 Comment on sustainability

Sustainability hasn't been explicitly treated in this thesis, however, vibration studies from traffic and other sources which affect buildings and liveable areas are directly linked to questions of sustainability as they effect the quality of life. As record breaking number of the worlds population is moving to urban areas there is a need to densify cities in order to sustain this influx of population which in turn brings in more traffic and creates areas where this type of study can be applied in order to make sure that the city is developed in a way that creates minimal environmental pollution in terms of disturbances from vibrations (including secondary effects such as noise created by the vibrations). As an example the same type of method could be applied on say researching the effects of a new road with heavy traffic next to some older buildings which are sensitive to vibrations, where placing masses in between could potentially bring the vibrations down to acceptable levels.

5.2 Further work

The simulations in the project have been concluded for steady-state harmonic conditions, which may not be the best way to model the load from moving vehicles. Transient analysis with a moving load could maybe bring more insight into the effectiveness of the method proposed.

The study has mainly been limited to vertical vibrations, but parts of the MAX-lab facility are equally sensitive to horizontal displacement as they are to vertical. The little which is shown of horizontal vibrations in the thesis seems to suggest that they have a similar effect on horizontal vibrations (as do some sources, see [4] [13]), but it is not enough to conclude.

It was planned to develop constraints in the 3D model in MATLAB with the use of Lagrange multipliers to make it possible to use more sophisticated building models for which the nodes don't match up perfectly with those of the soil model, but the dynamic reduction took more time than expected so this part had to be skipped.

Besides road traffic on both sides of MAX-lab, there exist plans for a tramway going past MAX-lab on a few hundred meters distance. The vibrations from the trams are at higher frequencies (100-200Hz) and have not been studied in this thesis. One would have to check for the effectiveness of buildings/masses for these vibrations as well.

A generalization of the method as a tool for early design studies would be a valuable development to have for future days when vibrations between different types of vehicles and old and new buildings will due to densification become larger issues.

References

[1] V. Alic. *Good vibrations*. Chalmers University of Technology, 2012.

[2] L. Andersen. *Linear Elastodynamic Analysis*. 3. Aalborg University, 2006.

[3] R. Craig and A. Kurdila. *Fundamentals of structural dynamics*. Wiley, 2006.

[4] R. Ford. "Inhibiting the transmission of ground-borne vibrations by placing masses on the surface of the ground". *Australian Vibration and Noise Conference 1990: Vibration and Noise-measurement Prediction and Control; Preprints of Papers*. Institution of Engineers, Australia. 1990, p. 227.

[5] D. Jones and M. Petyt. *Ground borne vibrations from passing trains: the effect of masses placed on the ground's surface*. ISVR Technical Memorandum, 1986.

[6] D. Jones and M. Petyt. Ground vibration in the vicinity of a rectangular load on a half-space. *Journal of sound and vibration* **166**.1 (1993), 141–159.

[7] A. Khlopotin and S. Razanica. *Designing materials for mechanical invisibility cloaks*. Chalmers University of Technology, 2012.

[8] V. Krylov. Control of Traffic-Induced Ground Vibrations by Placing Heavy Masses on the Ground Surface. *Low Frequency Noise, Vibration and Active Control* **26**.4 (2007), 311–320.

[9] *MATLAB manual. Ordinary Differential Equations*. Version 7.8. Mathworks, 2008. URL: `http://www.mathworks.com/access/helpdesk/help/techdoc/ref/ode45.html`.

[10] Maxlab. *MAX-lab*. Mar. 2013. URL: `https://www.maxlab.lu.se/`.

[11] N. S. Ottosen and H. Petersson. *Introduction to the finite element method*. Prentice hall, 1992.

[12] F. Paul. *Ripple Tank Java Applet*. Mar. 2012. URL: `http://www.falstad.com/ripple/`.

[13] V. Plessky and A. Simonian. Rayleigh wave reflection and scattering on a resonator. *Physics Letters A* **155**.4 (1991), 281–284.

[14] Z. Qu. *Model order reduction techniques: with applications in finite element analysis*. Springer, 2004.

[15] Rydén et al. *MaxLab IV - Geodynamic parameters for the ground*. Technical report. Norwegian Geotechnical Institute, 2011.

[16] F. Seron et al. Finite-element method for elastic wave propagation. *Communications in applied numerical methods* **6**.5 (1990), 359–368.

[17] J. Sun et al. Highly stretchable and tough hydrogels. *Nature* **489**.7414 (2012), 133–136.

[18] D. Systèmes. ABAQUS analysis user's manual (2007).

A Plots for 3D results

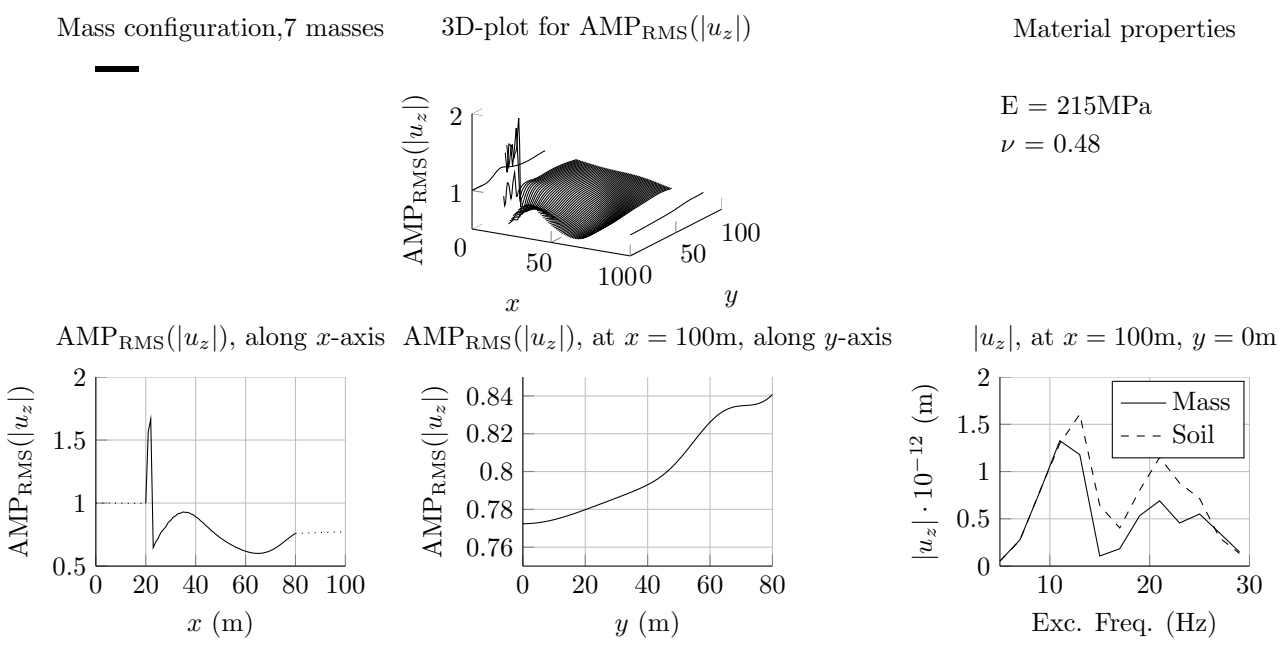

Figure A.1: *3D results for wall-3, consisting of only seven masses close to the load. (Top left) Organization of masses. (Top middle) 3D-plot of RMS amplification of vertical displacement magnitude. (Top right) Mass properties. (Bottom left) RMS amplificiation of vertical displacement magnitude along x-axis. (Bottom middle) RMS amplificiation of vertical displacement magnitude along y-axis, 100 meters from the load application point. (Bottom right) Vertical displacement magnitude response at $x = 100m$, $y = 0m$.*

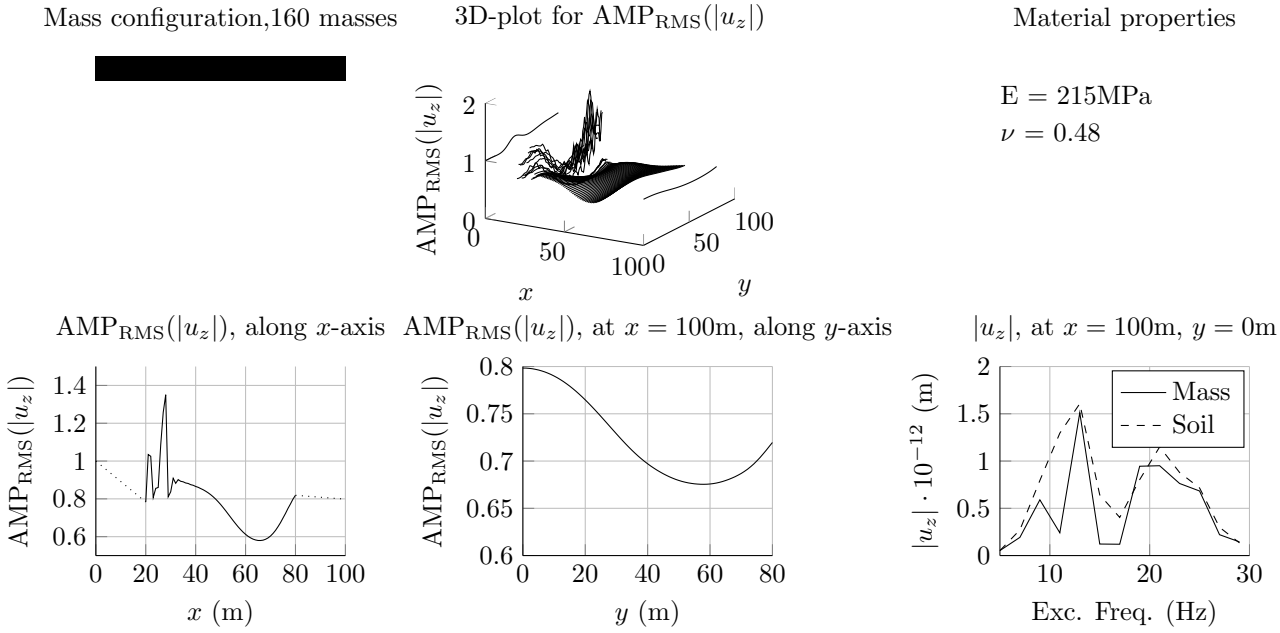

Figure A.2: *3D results for wall-4, four times thicker than wall-1. (Top left) Organization of masses. (Top middle) 3D-plot of RMS amplification of vertical displacement magnitude. (Top right) Mass properties. (Bottom left) RMS amplificiation of vertical displacement magnitude along x-axis. (Bottom middle) RMS amplificiation of vertical displacement magnitude along y-axis, 100 meters from the load application point. (Bottom right) Vertical displacement magnitude response at $x = 100m$, $y = 0m$.*

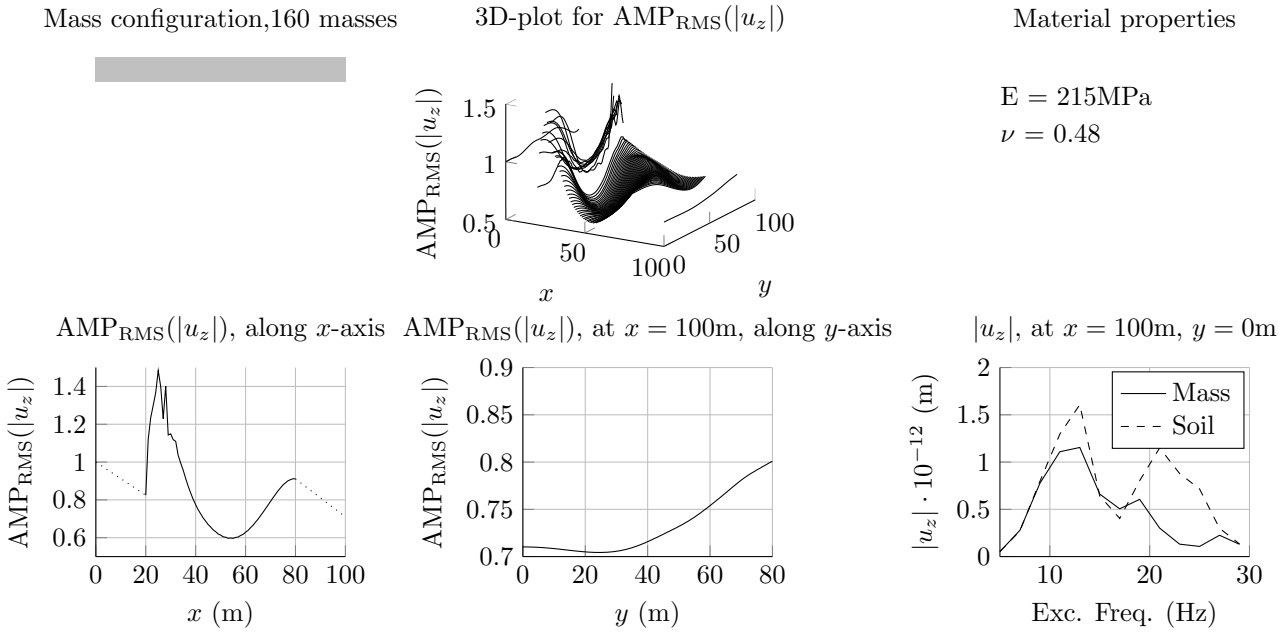

Figure A.3: *3D results for wall-5, four times thicker than wall-1, 25% of $\rho_{\max}$. (Top left) Organization of masses. (Top middle) 3D-plot of RMS amplification of vertical displacement magnitude. (Top right) Mass properties. (Bottom left) RMS amplificiation of vertical displacement magnitude along x-axis. (Bottom middle) RMS amplificiation of vertical displacement magnitude along y-axis, 100 meters from the load application point. (Bottom right) Vertical displacement magnitude response at $x = 100m$, $y = 0m$.*

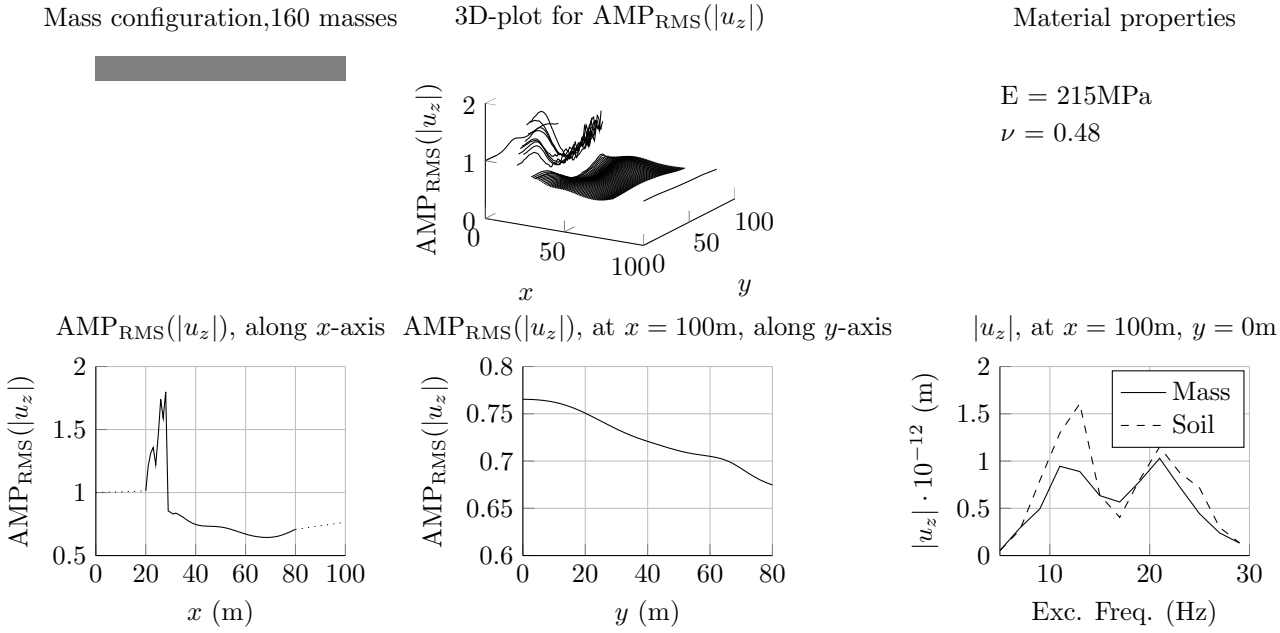

Figure A.4: *3D results for wall-6, four times thicker than wall-1, 50% of $\rho_{\max}$. (Top left) Organization of masses. (Top middle) 3D-plot of RMS amplification of vertical displacement magnitude. (Top right) Mass properties. (Bottom left) RMS amplificiation of vertical displacement magnitude along x-axis. (Bottom middle) RMS amplificiation of vertical displacement magnitude along y-axis, 100 meters from the load application point. (Bottom right) Vertical displacement magnitude response at $x = 100m$, $y = 0m$.*

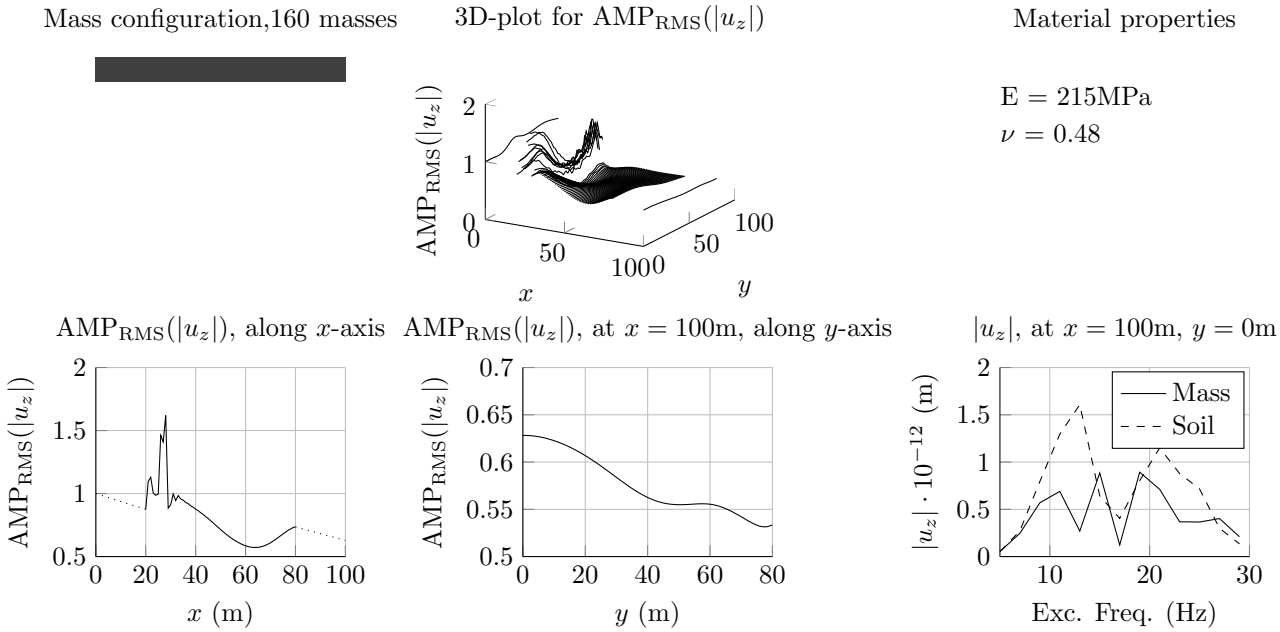

Figure A.5: *3D results for wall-7, four times thicker than wall-1, 75% of $\rho_{\max}$. (Top left) Organization of masses. (Top middle) 3D-plot of RMS amplification of vertical displacement magnitude. (Top right) Mass properties. (Bottom left) RMS amplificiation of vertical displacement magnitude along x-axis. (Bottom middle) RMS amplificiation of vertical displacement magnitude along y-axis, 100 meters from the load application point. (Bottom right) Vertical displacement magnitude response at $x = 100m$, $y = 0m$.*

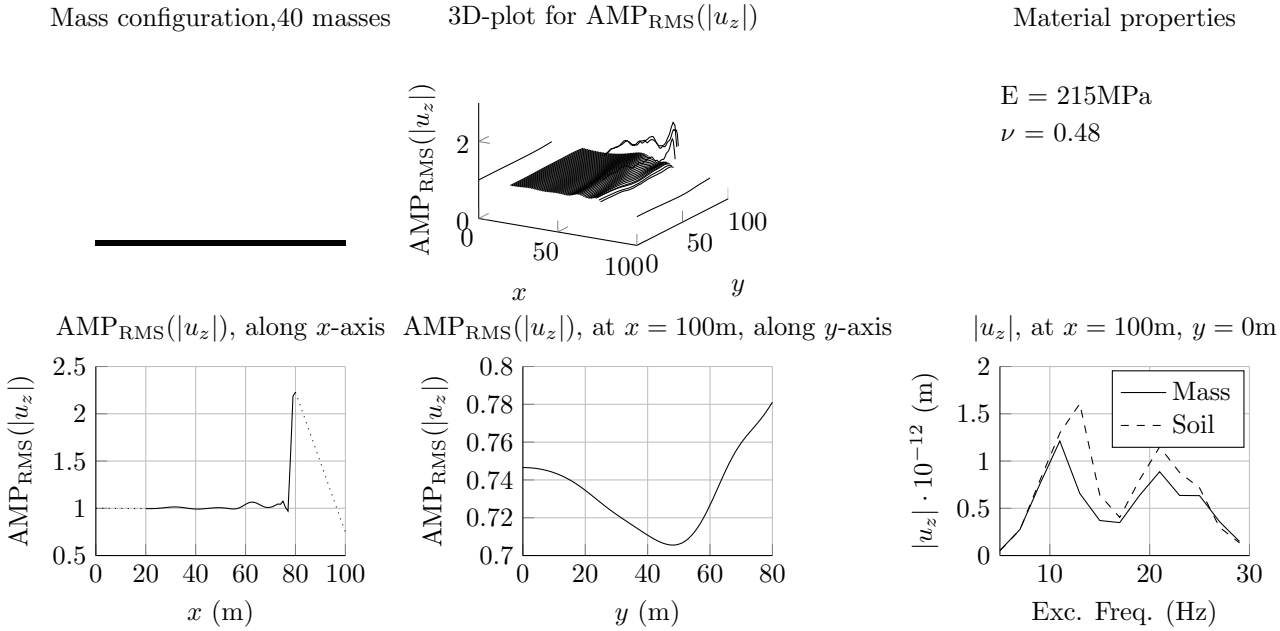

Figure A.6: *3D results for wall-10, similar to wall-1, but placed furthest from the load. (Top left) Organization of masses. (Top middle) 3D-plot of RMS amplification of vertical displacement magnitude. (Top right) Mass properties. (Bottom left) RMS amplificiation of vertical displacement magnitude along x-axis. (Bottom middle) RMS amplificiation of vertical displacement magnitude along y-axis, 100 meters from the load application point. (Bottom right) Vertical displacement magnitude response at $x = 100m$, $y = 0m$.*

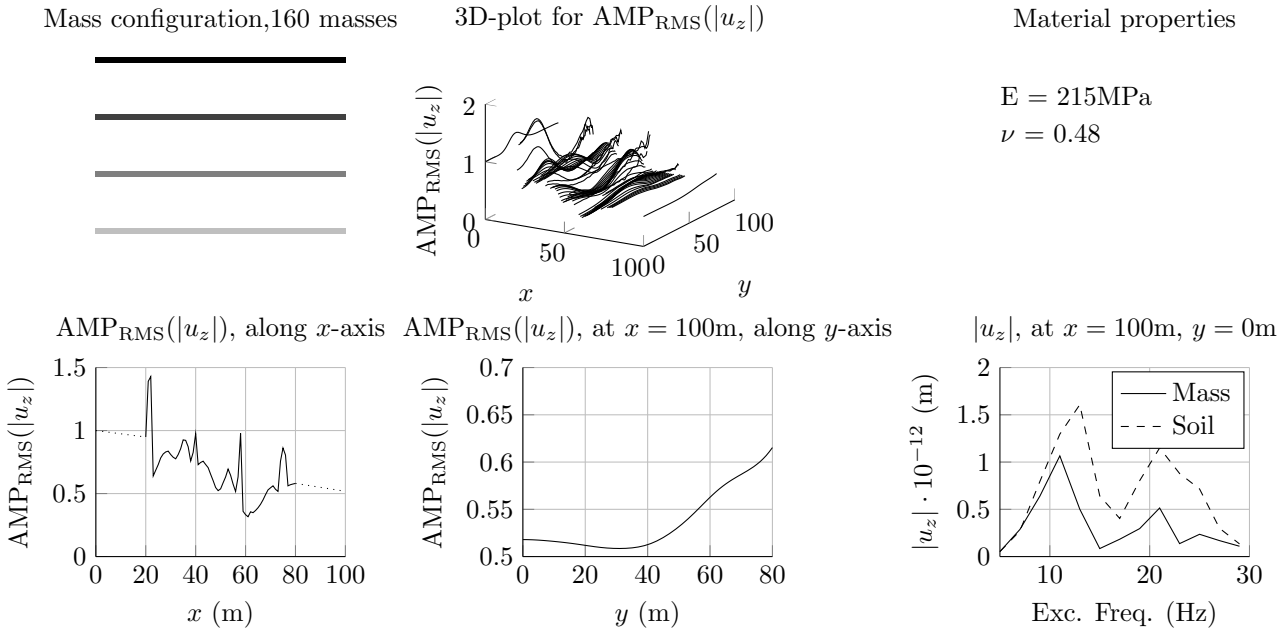

Figure A.7: *3D results for wall-8, four walls, 100%, 75%, 59%, 25% of $\rho_{\max}$ respectively. (Top left) Organization of masses. (Top middle) 3D-plot of RMS amplification of vertical displacement magnitude. (Top right) Mass properties. (Bottom left) RMS amplificiation of vertical displacement magnitude along x-axis. (Bottom middle) RMS amplificiation of vertical displacement magnitude along y-axis, 100 meters from the load application point. (Bottom right) Vertical displacement magnitude response at $x = 100m$, $y = 0m$.*

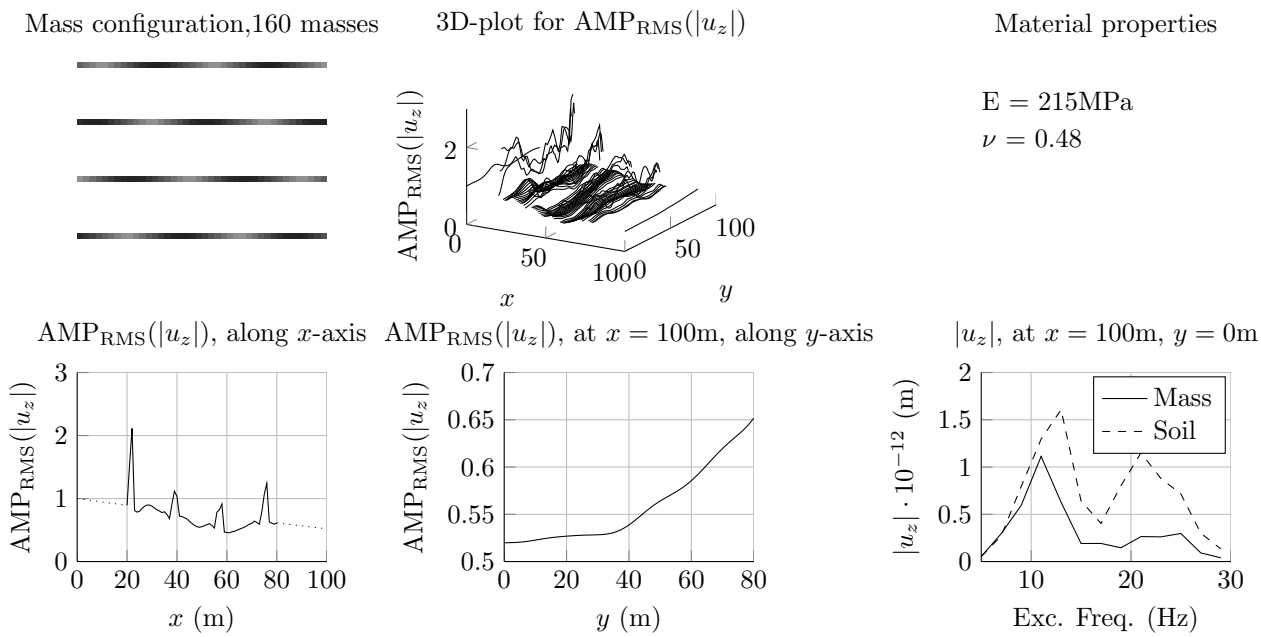

Figure A.8: *3D results for wall-9, four walls with densities that vary with sinusoidal shapes. (Top left) Organization of masses. (Top middle) 3D-plot of RMS amplification of vertical displacement magnitude. (Top right) Mass properties. (Bottom left) RMS amplificiation of vertical displacement magnitude along x-axis. (Bottom middle) RMS amplificiation of vertical displacement magnitude along y-axis, 100 meters from the load application point. (Bottom right) Vertical displacement magnitude response at $x = 100m$, $y = 0m$.*

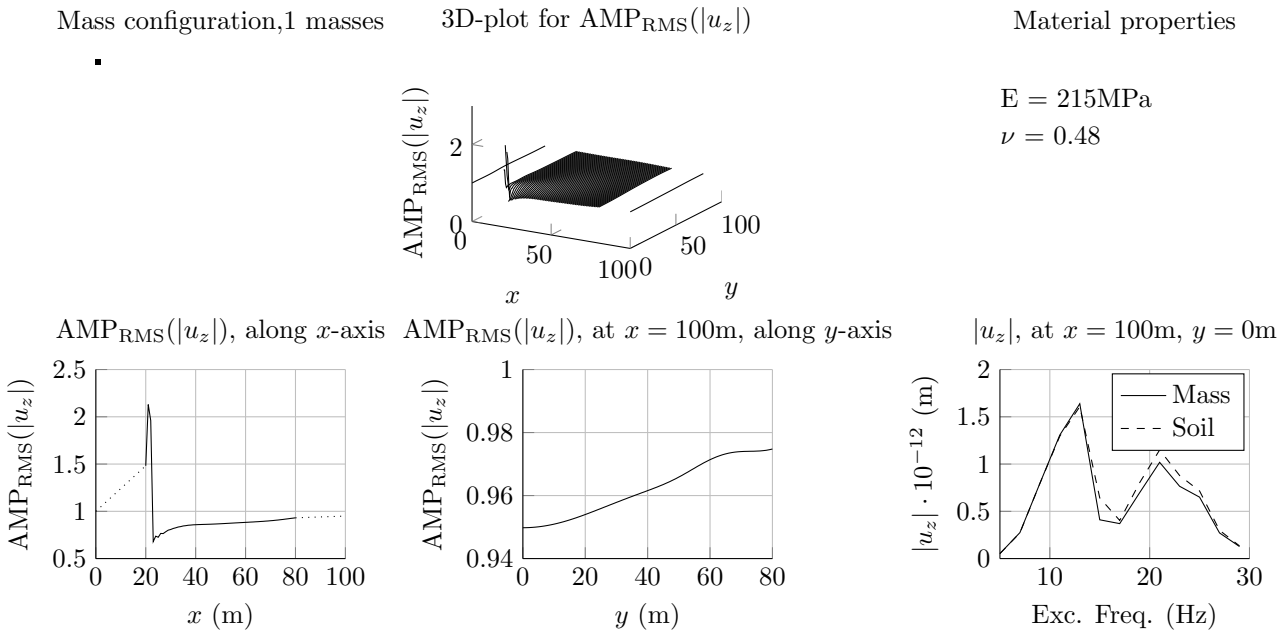

Figure A.9: *3D results for mass-1, a single mass placed at the point closest to the load. (Top left) Organization of masses. (Top middle) 3D-plot of RMS amplification of vertical displacement magnitude. (Top right) Mass properties. (Bottom left) RMS amplificiation of vertical displacement magnitude along x-axis. (Bottom middle) RMS amplificiation of vertical displacement magnitude along y-axis, 100 meters from the load application point. (Bottom right) Vertical displacement magnitude response at $x = 100m$, $y = 0m$.*

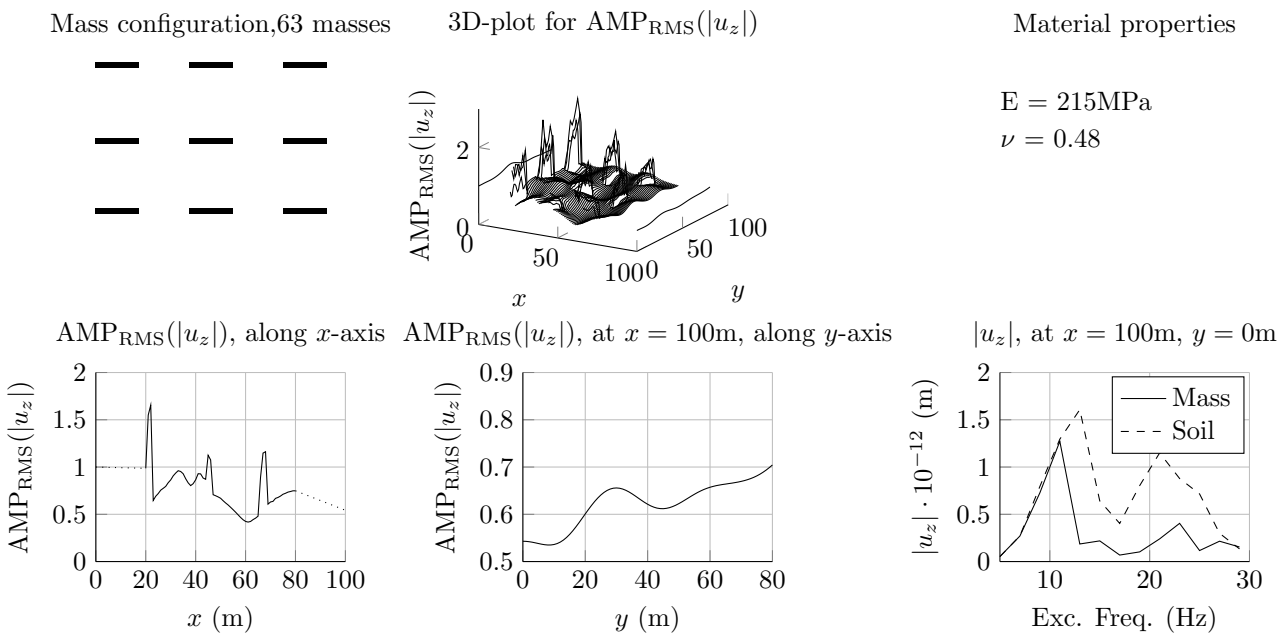

Figure A.10: *3D results for line-1, consisting of 3 rows of lines. (Top left) Organization of masses. (Top middle) 3D-plot of RMS amplification of vertical displacement magnitude. (Top right) Mass properties. (Bottom left) RMS amplificiation of vertical displacement magnitude along x-axis. (Bottom middle) RMS amplificiation of vertical displacement magnitude along y-axis, 100 meters from the load application point. (Bottom right) Vertical displacement magnitude response at* $x = 100m$, $y = 0m$.

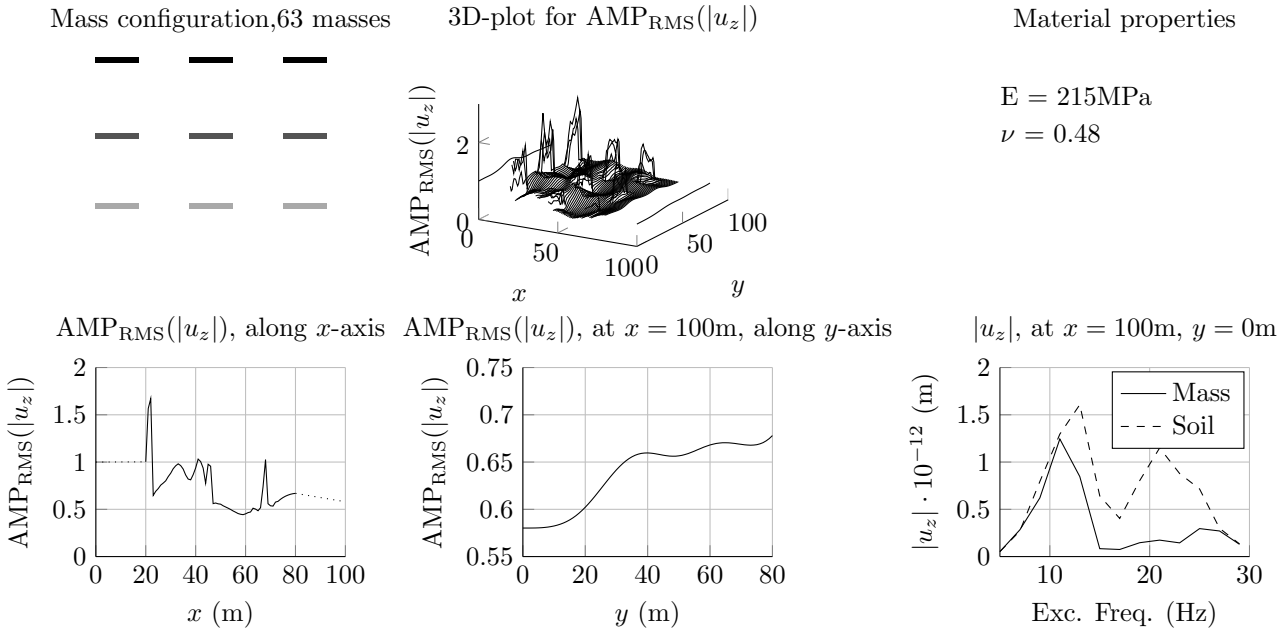

Figure A.11: *3D results for line-2, consisting of 3 rows of lines, with 100%, 66%, 33%, of* $\rho_{\max}$ *respectively. (Top left) Organization of masses. (Top middle) 3D-plot of RMS amplification of vertical displacement magnitude. (Top right) Mass properties. (Bottom left) RMS amplificiation of vertical displacement magnitude along x-axis. (Bottom middle) RMS amplificiation of vertical displacement magnitude along y-axis, 100 meters from the load application point. (Bottom right) Vertical displacement magnitude response at* $x = 100m$, $y = 0m$.

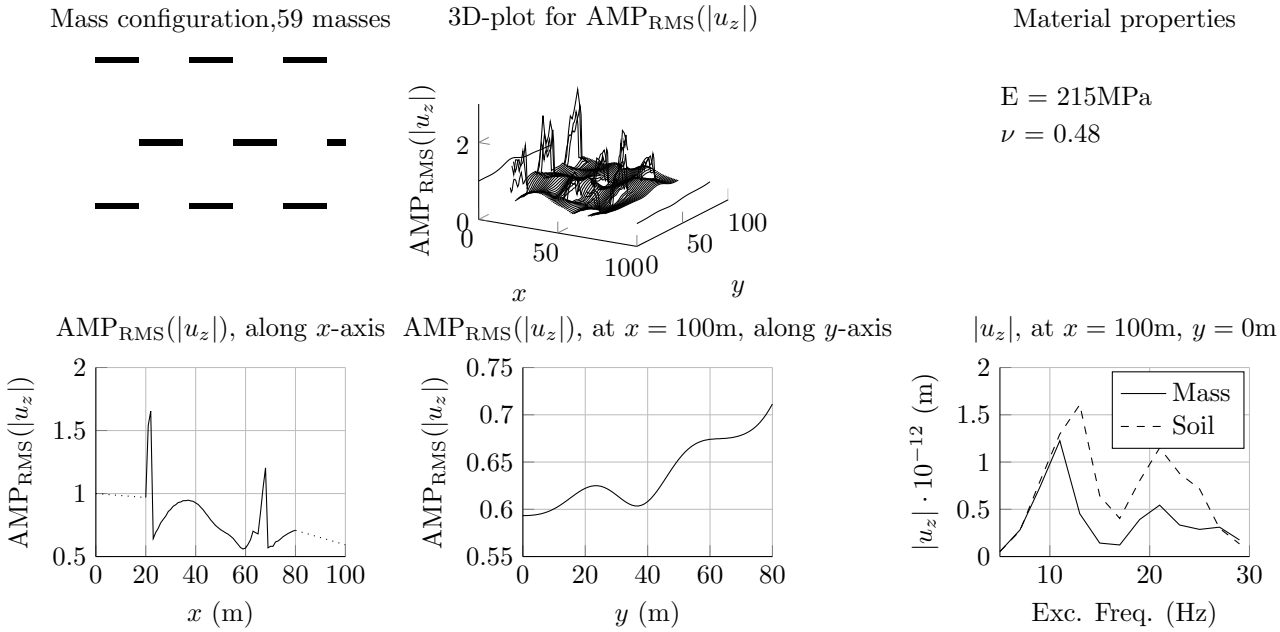

Figure A.12: *3D results for line-5,consisting of 3 rows of lines, with second row offset. (Top left) Organization of masses. (Top middle) 3D-plot of RMS amplification of vertical displacement magnitude. (Top right) Mass properties. (Bottom left) RMS amplificiation of vertical displacement magnitude along x-axis. (Bottom middle) RMS amplificiation of vertical displacement magnitude along y-axis, 100 meters from the load application point. (Bottom right) Vertical displacement magnitude response at $x = 100m$, $y = 0m$.*

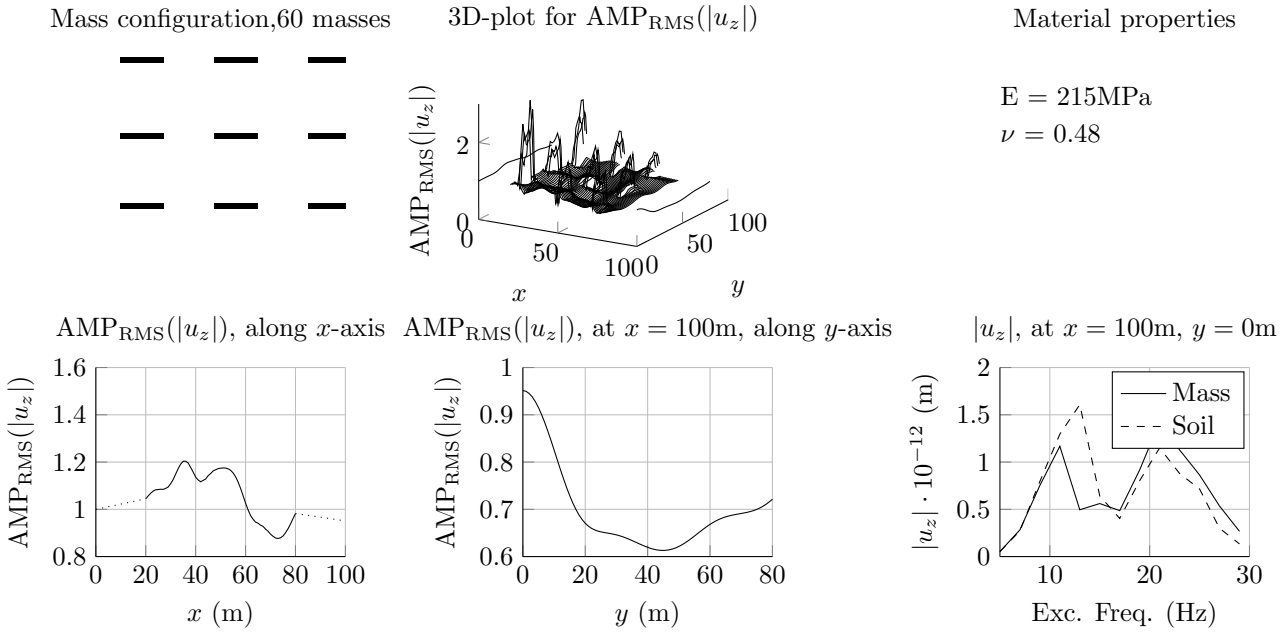

Figure A.13: *3D results for line-9, consisting of 3 rows of lines, offset 8m y-direction compared to Figure A.10. (Top left) Organization of masses. (Top middle) 3D-plot of RMS amplification of vertical displacement magnitude. (Top right) Mass properties. (Bottom left) RMS amplificiation of vertical displacement magnitude along x-axis. (Bottom middle) RMS amplificiation of vertical displacement magnitude along y-axis, 100 meters from the load application point. (Bottom right) Vertical displacement magnitude response at $x = 100m$, $y = 0m$.*

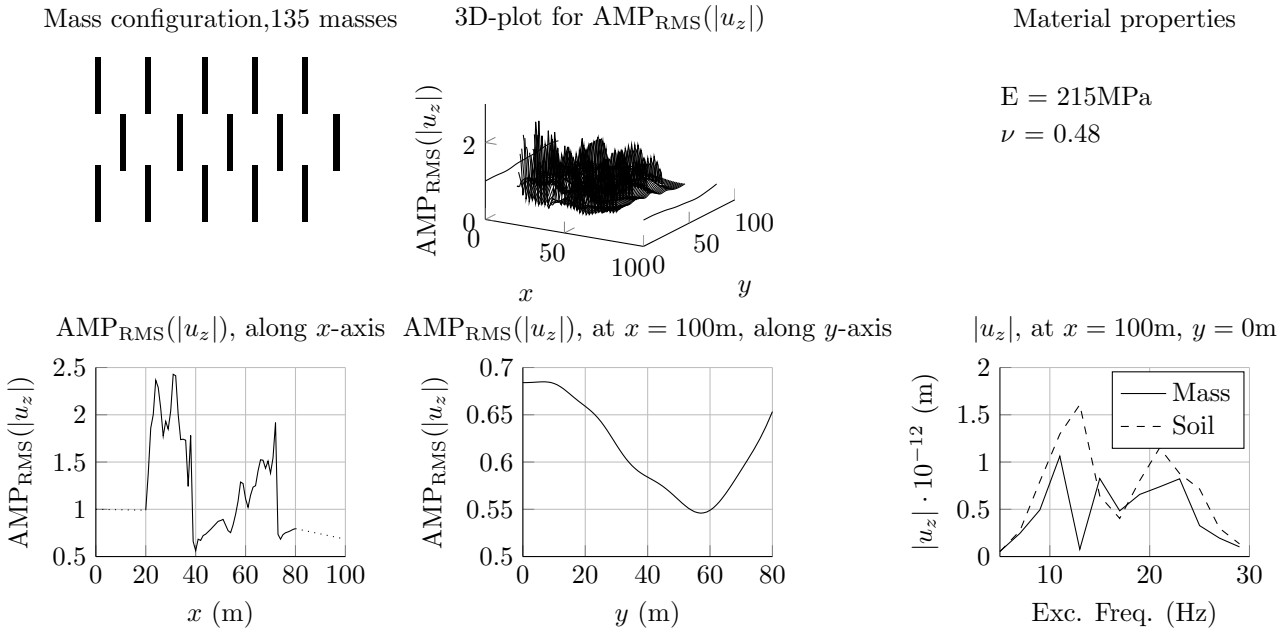

Figure A.14: *3D results for perpendicular-1, consisting of perpendicular rows of lines, with every other row offset. (Top left) Organization of masses. (Top middle) 3D-plot of RMS amplification of vertical displacement magnitude. (Top right) Mass properties. (Bottom left) RMS amplificiation of vertical displacement magnitude along x-axis. (Bottom middle) RMS amplificiation of vertical displacement magnitude along y-axis, 100 meters from the load application point. (Bottom right) Vertical displacement magnitude response at $x = 100m$, $y = 0m$.*

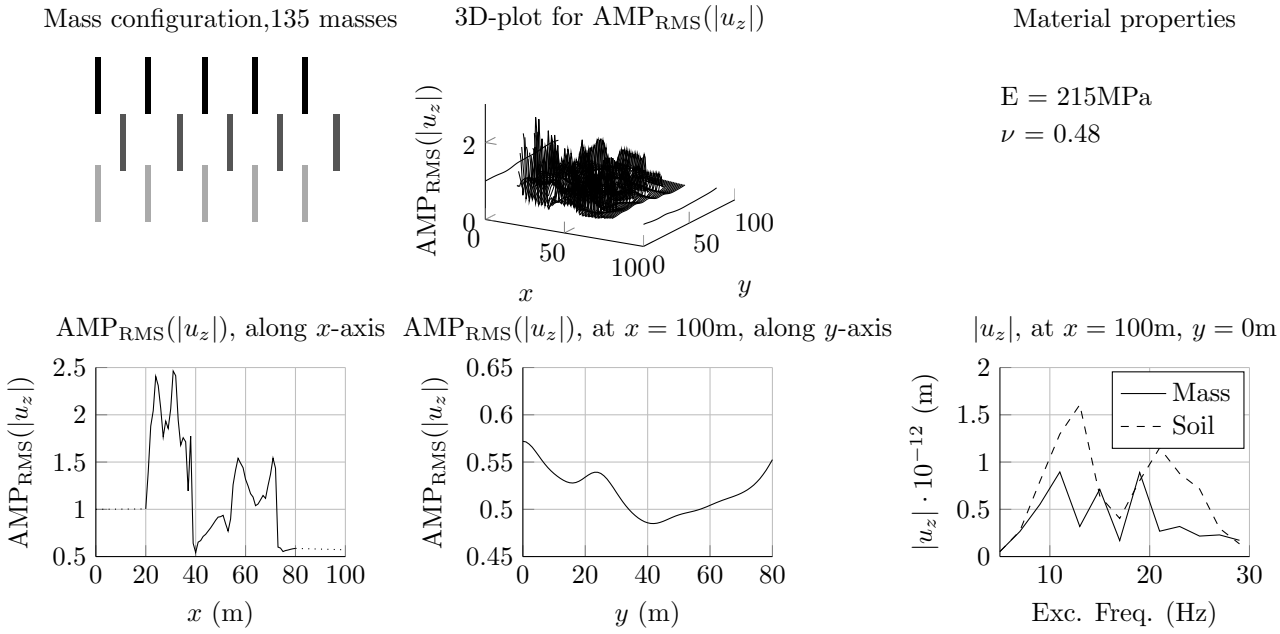

Figure A.15: *3D results for perpendicular-2, with 100%, 66%, 33%, of $\rho_{\max}$ respectively. (Top left) Organization of masses. (Top middle) 3D-plot of RMS amplification of vertical displacement magnitude. (Top right) Mass properties. (Bottom left) RMS amplificiation of vertical displacement magnitude along x-axis. (Bottom middle) RMS amplificiation of vertical displacement magnitude along y-axis, 100 meters from the load application point. (Bottom right) Vertical displacement magnitude response at $x = 100m$, $y = 0m$.*

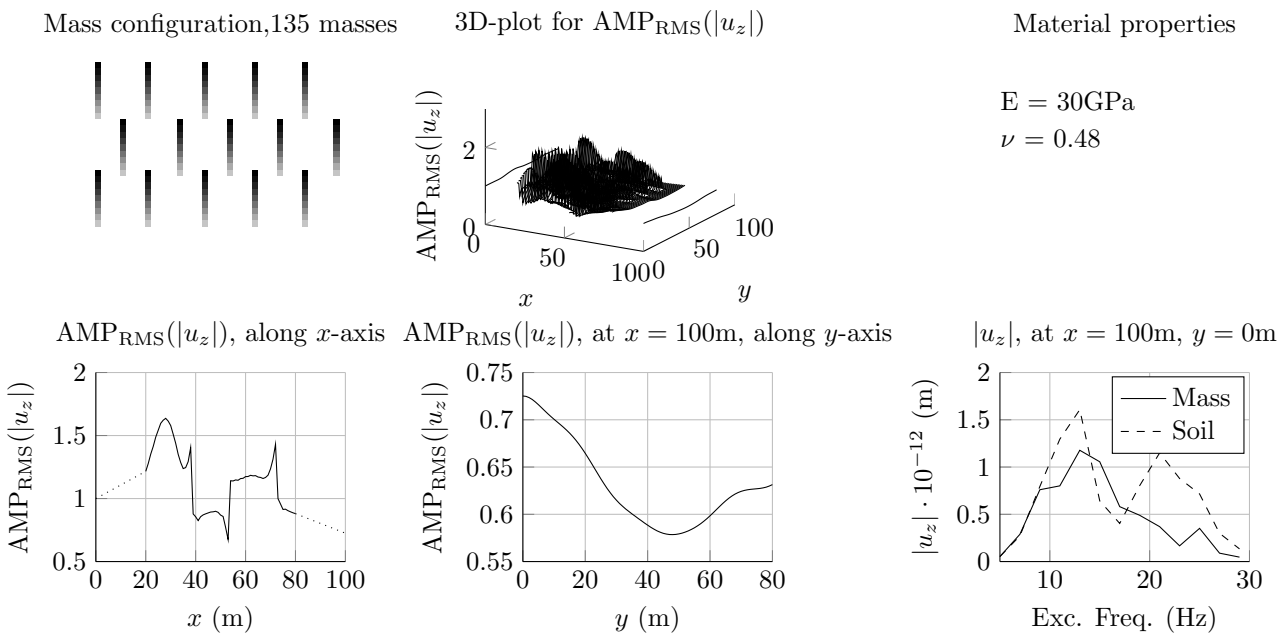

Figure A.16: *3D results for perpendicular-6, stiff version of perpendicular-3. (Top left) Organization of masses. (Top middle) 3D-plot of RMS amplification of vertical displacement magnitude. (Top right) Mass properties. (Bottom left) RMS amplificiation of vertical displacement magnitude along x-axis. (Bottom middle) RMS amplificiation of vertical displacement magnitude along y-axis, 100 meters from the load application point. (Bottom right) Vertical displacement magnitude response at* $x = 100m$, $y = 0m$.

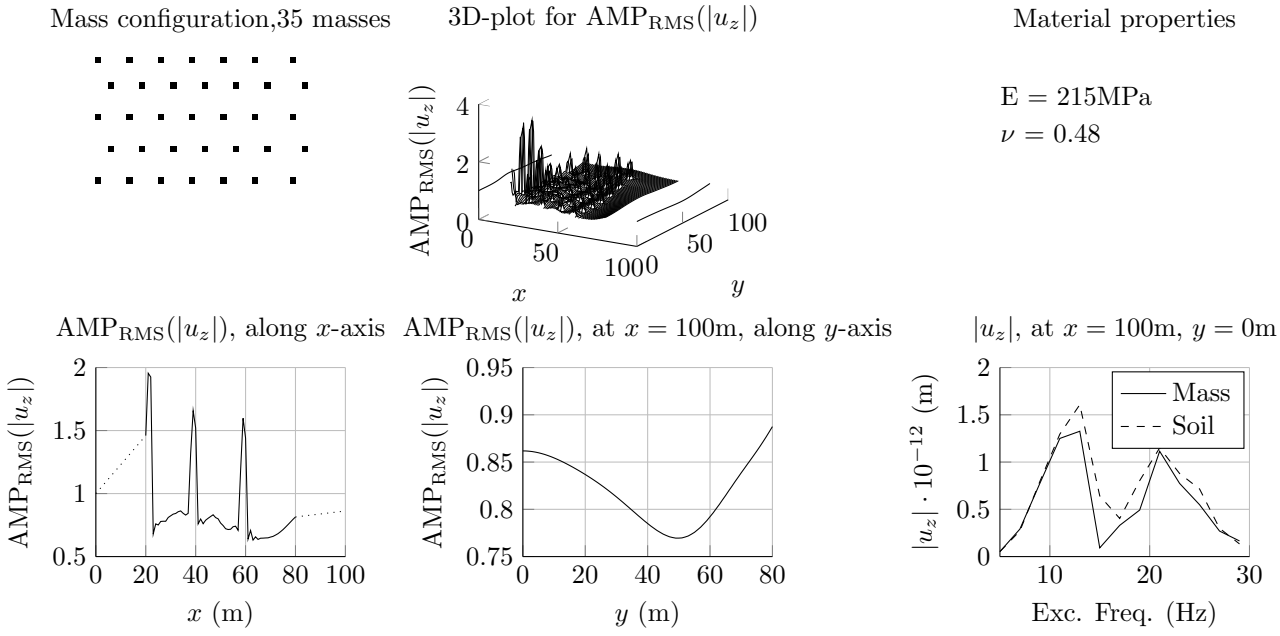

Figure A.17: *3D results for dots-2, consisting of single masses in arrays, every other row is offset. (Top left) Organization of masses. (Top middle) 3D-plot of RMS amplification of vertical displacement magnitude. (Top right) Mass properties. (Bottom left) RMS amplificiation of vertical displacement magnitude along x-axis. (Bottom middle) RMS amplificiation of vertical displacement magnitude along y-axis, 100 meters from the load application point. (Bottom right) Vertical displacement magnitude response at* $x = 100m$, $y = 0m$.

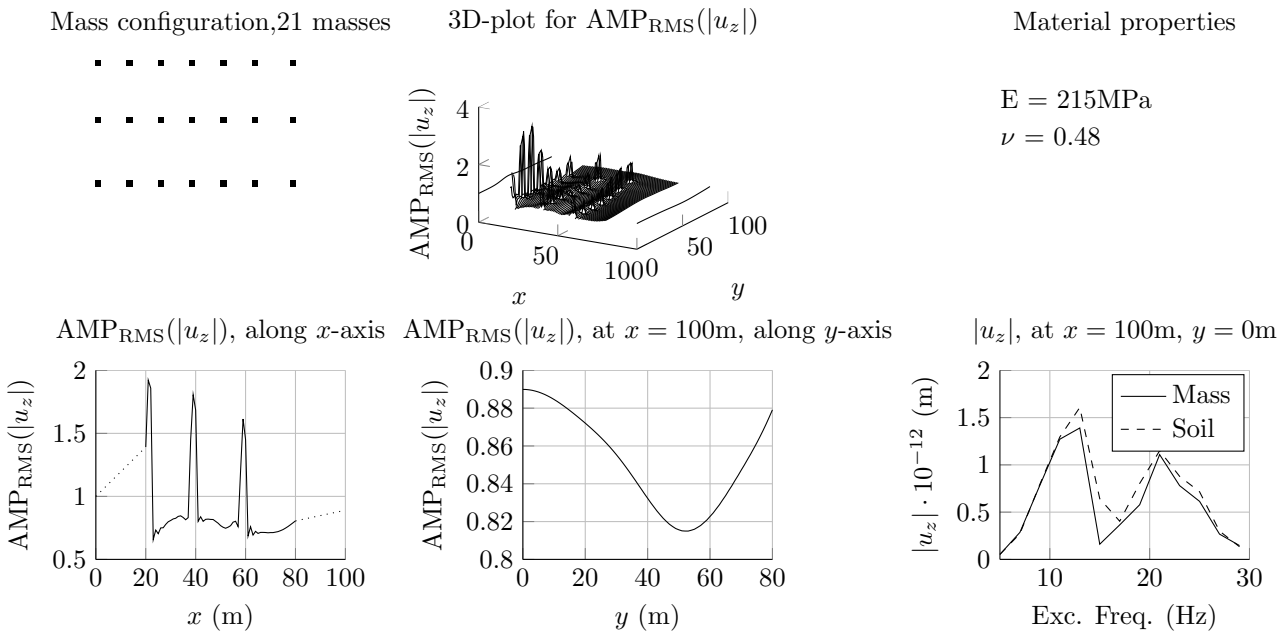

Figure A.18: *3D results for dots-3, consisting of single masses in arrays. (Top left) Organization of masses. (Top middle) 3D-plot of RMS amplification of vertical displacement magnitude. (Top right) Mass properties. (Bottom left) RMS amplificiation of vertical displacement magnitude along x-axis. (Bottom middle) RMS amplificiation of vertical displacement magnitude along y-axis, 100 meters from the load application point. (Bottom right) Vertical displacement magnitude response at $x = 100m$, $y = 0m$.*

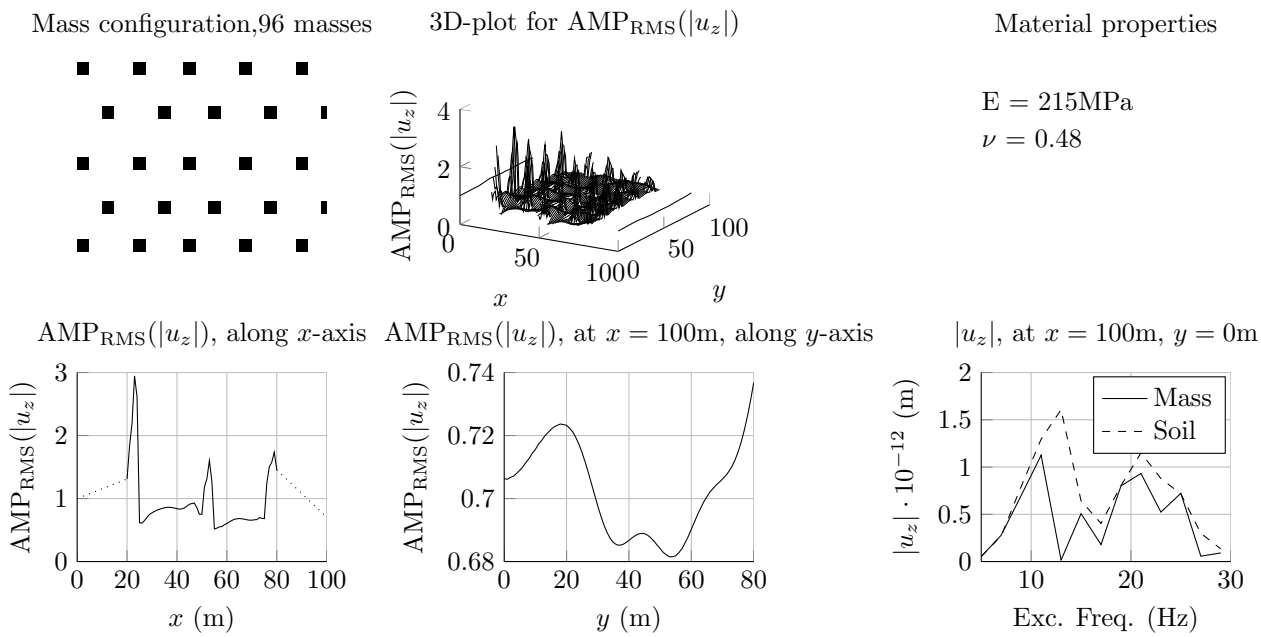

Figure A.19: *3D results for dots-4, consisting of larger(4 by 4) masses in arrays. (Top left) Organization of masses. (Top middle) 3D-plot of RMS amplification of vertical displacement magnitude. (Top right) Mass properties. (Bottom left) RMS amplificiation of vertical displacement magnitude along x-axis. (Bottom middle) RMS amplificiation of vertical displacement magnitude along y-axis, 100 meters from the load application point. (Bottom right) Vertical displacement magnitude response at $x = 100m$, $y = 0m$.*

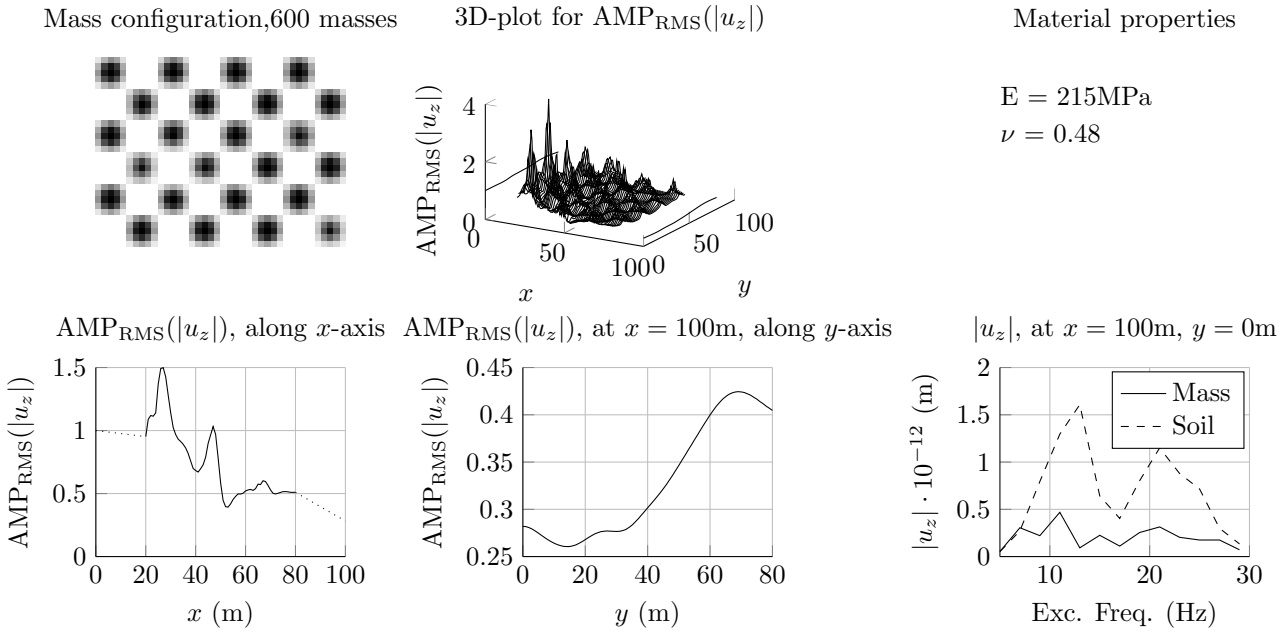

Figure A.20: *3D results for checkered-2. (Top left) Organization of masses. (Top middle) 3D-plot of RMS amplification of vertical displacement magnitude. (Top right) Mass properties. (Bottom left) RMS amplificiation of vertical displacement magnitude along x-axis. (Bottom middle) RMS amplificiation of vertical displacement magnitude along y-axis, 100 meters from the load application point. (Bottom right) Vertical displacement magnitude response at $x = 100m$, $y = 0m$.*

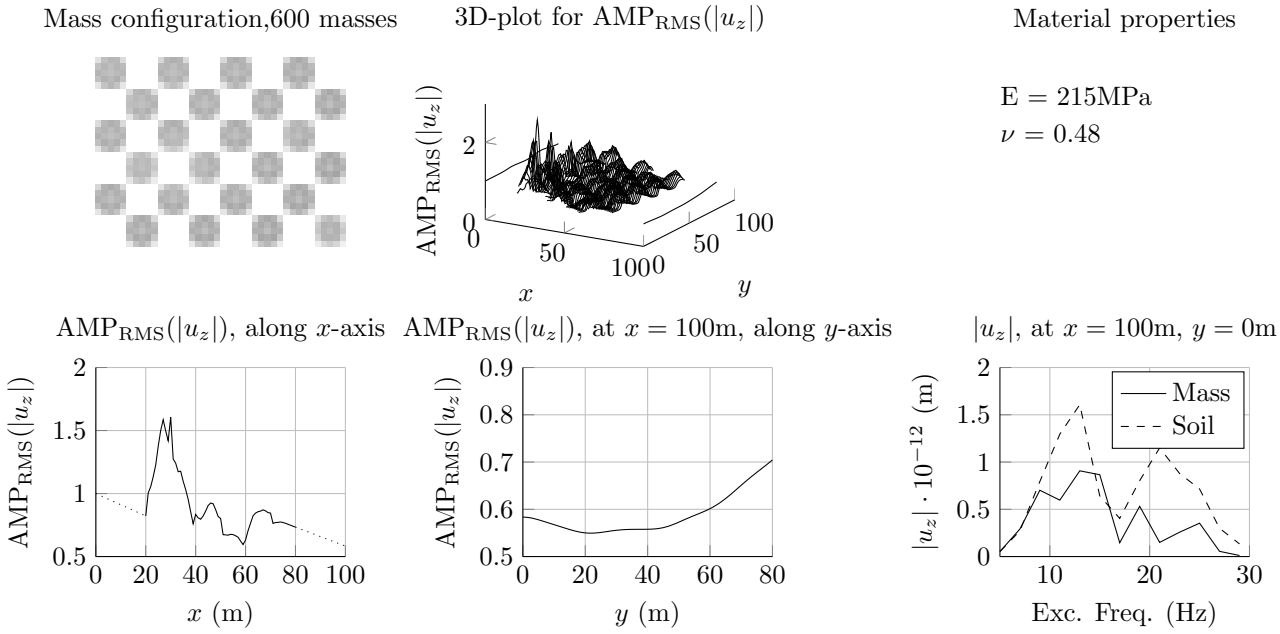

Figure A.21: *3D results for checkered-3. (Top left) Organization of masses. (Top middle) 3D-plot of RMS amplification of vertical displacement magnitude. (Top right) Mass properties. (Bottom left) RMS amplificiation of vertical displacement magnitude along x-axis. (Bottom middle) RMS amplificiation of vertical displacement magnitude along y-axis, 100 meters from the load application point. (Bottom right) Vertical displacement magnitude response at $x = 100m$, $y = 0m$.*

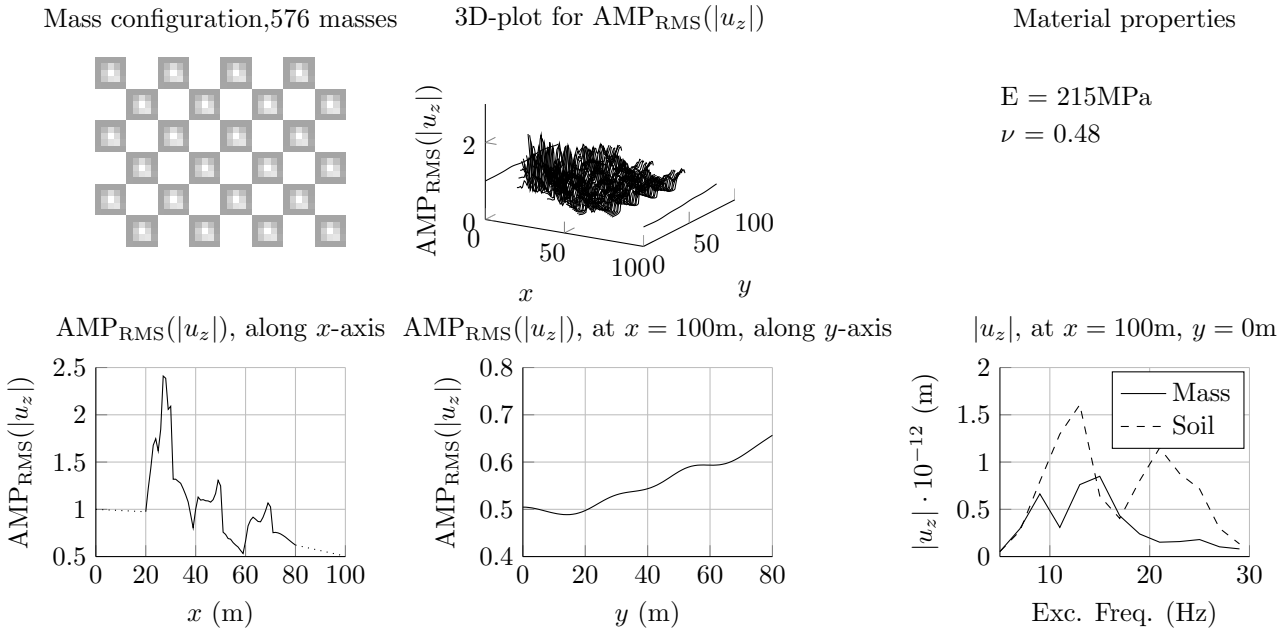

Figure A.22: *3D results for checkered-7. (Top left) Organization of masses. (Top middle) 3D-plot of RMS amplification of vertical displacement magnitude. (Top right) Mass properties. (Bottom left) RMS amplificiation of vertical displacement magnitude along x-axis. (Bottom middle) RMS amplificiation of vertical displacement magnitude along y-axis, 100 meters from the load application point. (Bottom right) Vertical displacement magnitude response at $x = 100m$, $y = 0m$.*

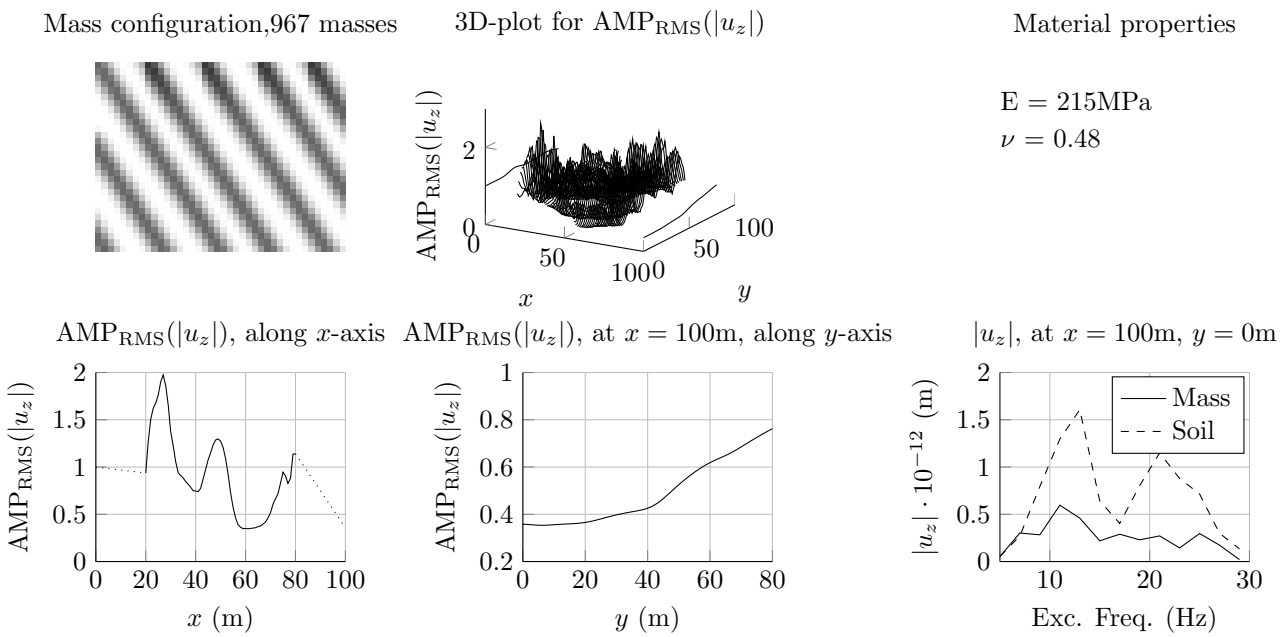

Figure A.23: *3D results for diagonal-1. (Top left) Organization of masses. (Top middle) 3D-plot of RMS amplification of vertical displacement magnitude. (Top right) Mass properties. (Bottom left) RMS amplificiation of vertical displacement magnitude along x-axis. (Bottom middle) RMS amplificiation of vertical displacement magnitude along y-axis, 100 meters from the load application point. (Bottom right) Vertical displacement magnitude response at $x = 100m$, $y = 0m$.*

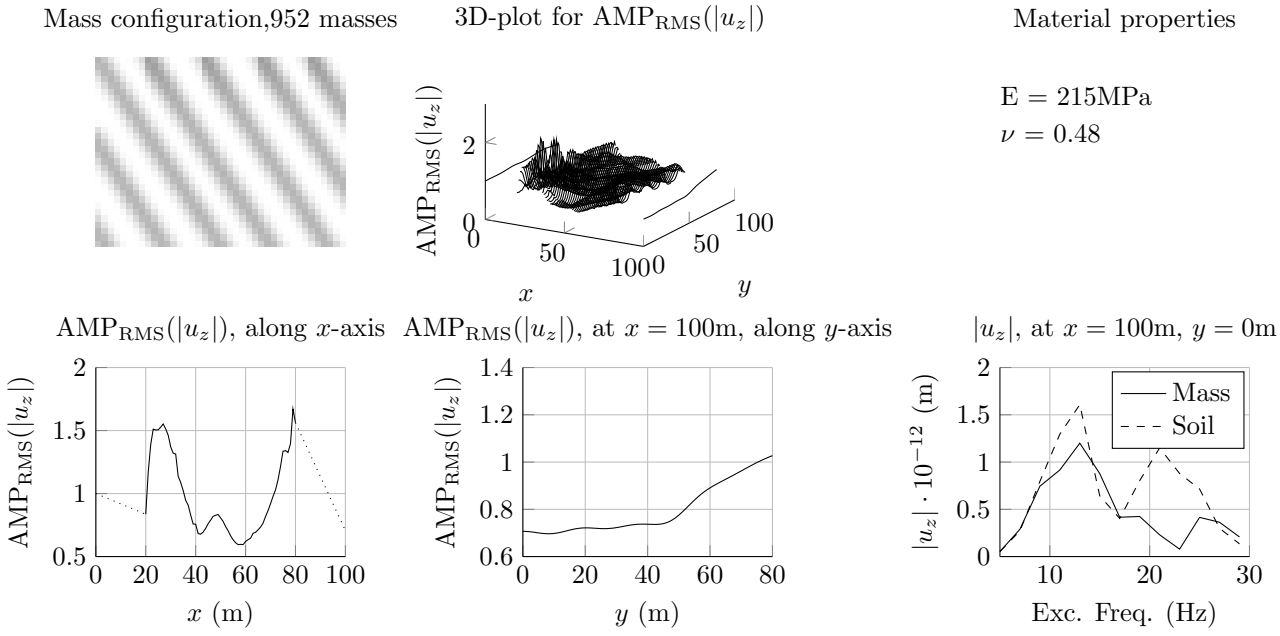

Figure A.24: *3D results for diagonal-2. (Top left) Organization of masses. (Top middle) 3D-plot of RMS amplification of vertical displacement magnitude. (Top right) Mass properties. (Bottom left) RMS amplificiation of vertical displacement magnitude along x-axis. (Bottom middle) RMS amplificiation of vertical displacement magnitude along y-axis, 100 meters from the load application point. (Bottom right) Vertical displacement magnitude response at $x = 100m$, $y = 0m$.*

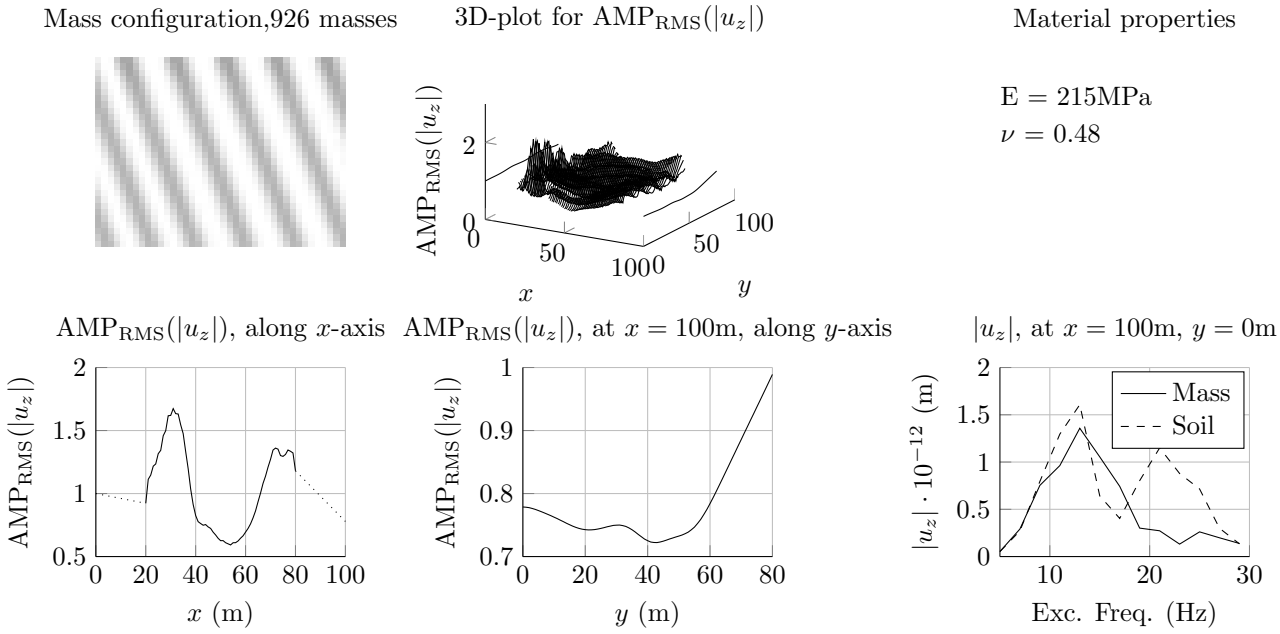

Figure A.25: *3D results for diagonal-5. (Top left) Organization of masses. (Top middle) 3D-plot of RMS amplification of vertical displacement magnitude. (Top right) Mass properties. (Bottom left) RMS amplificiation of vertical displacement magnitude along x-axis. (Bottom middle) RMS amplificiation of vertical displacement magnitude along y-axis, 100 meters from the load application point. (Bottom right) Vertical displacement magnitude response at $x = 100m$, $y = 0m$.*

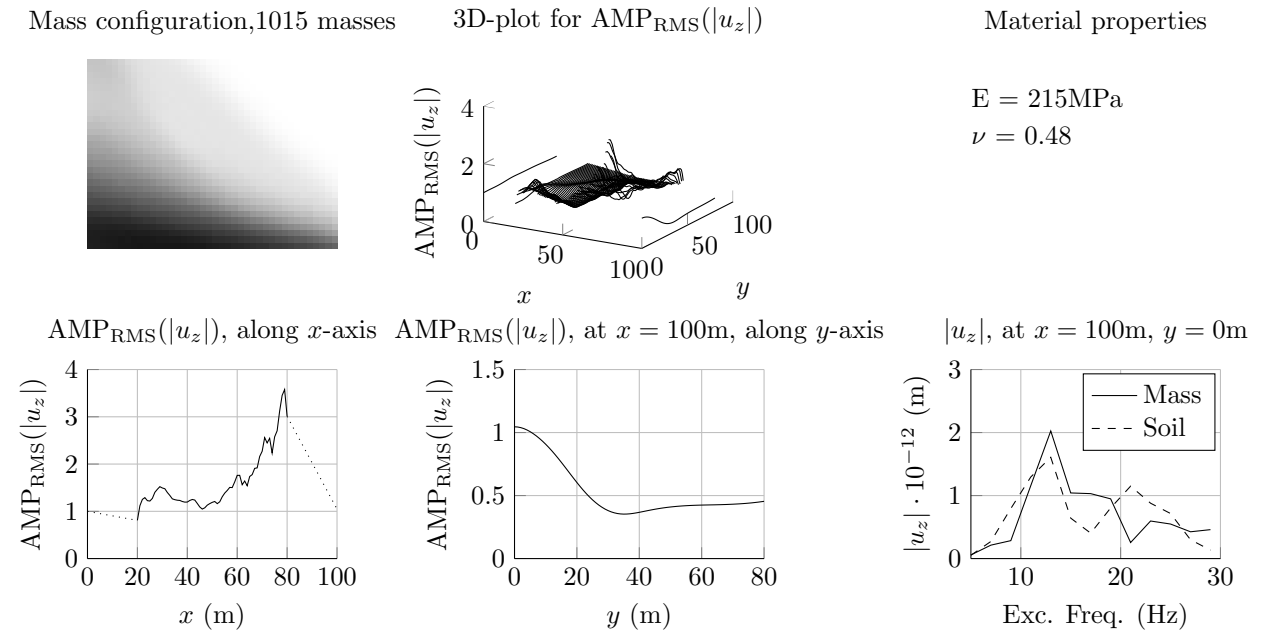

Figure A.26: *3D results for free-1. (Top left) Organization of masses. (Top middle) 3D-plot of RMS amplification of vertical displacement magnitude. (Top right) Mass properties. (Bottom left) RMS amplificiation of vertical displacement magnitude along x-axis. (Bottom middle) RMS amplificiation of vertical displacement magnitude along y-axis, 100 meters from the load application point. (Bottom right) Vertical displacement magnitude response at $x = 100m$, $y = 0m$.*

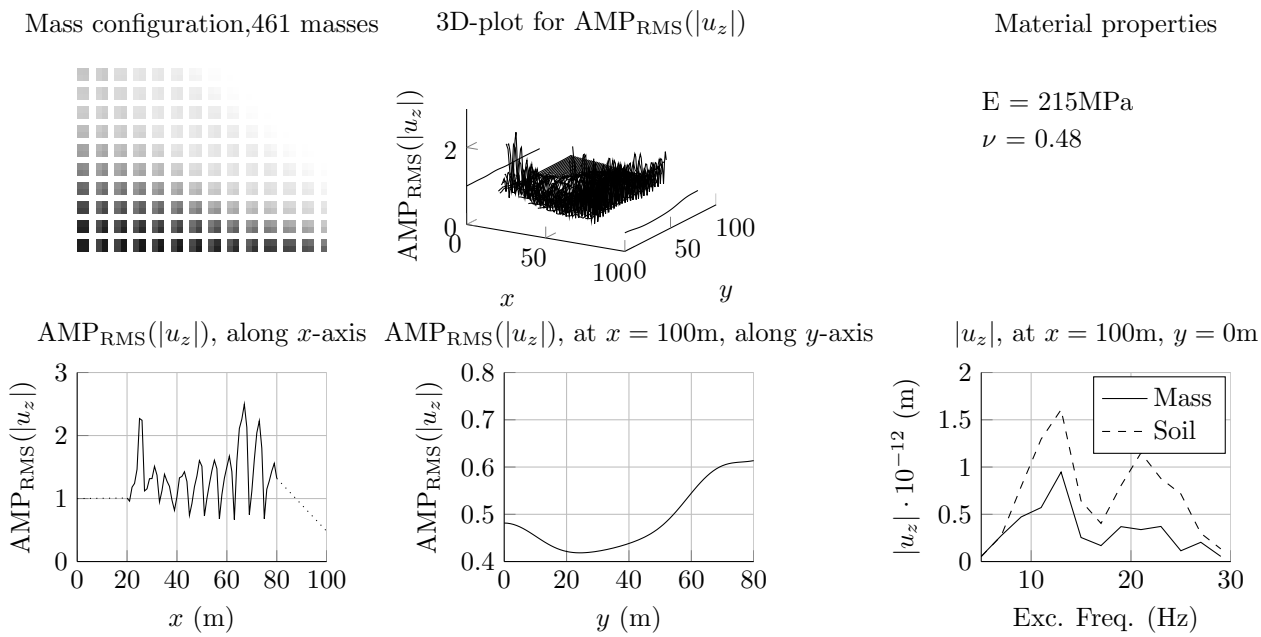

Figure A.27: *3D results for free-2, version of free-1 with discrete masses. (Top left) Organization of masses. (Top middle) 3D-plot of RMS amplification of vertical displacement magnitude. (Top right) Mass properties. (Bottom left) RMS amplificiation of vertical displacement magnitude along x-axis. (Bottom middle) RMS amplificiation of vertical displacement magnitude along y-axis, 100 meters from the load application point. (Bottom right) Vertical displacement magnitude response at $x = 100m$, $y = 0m$.*

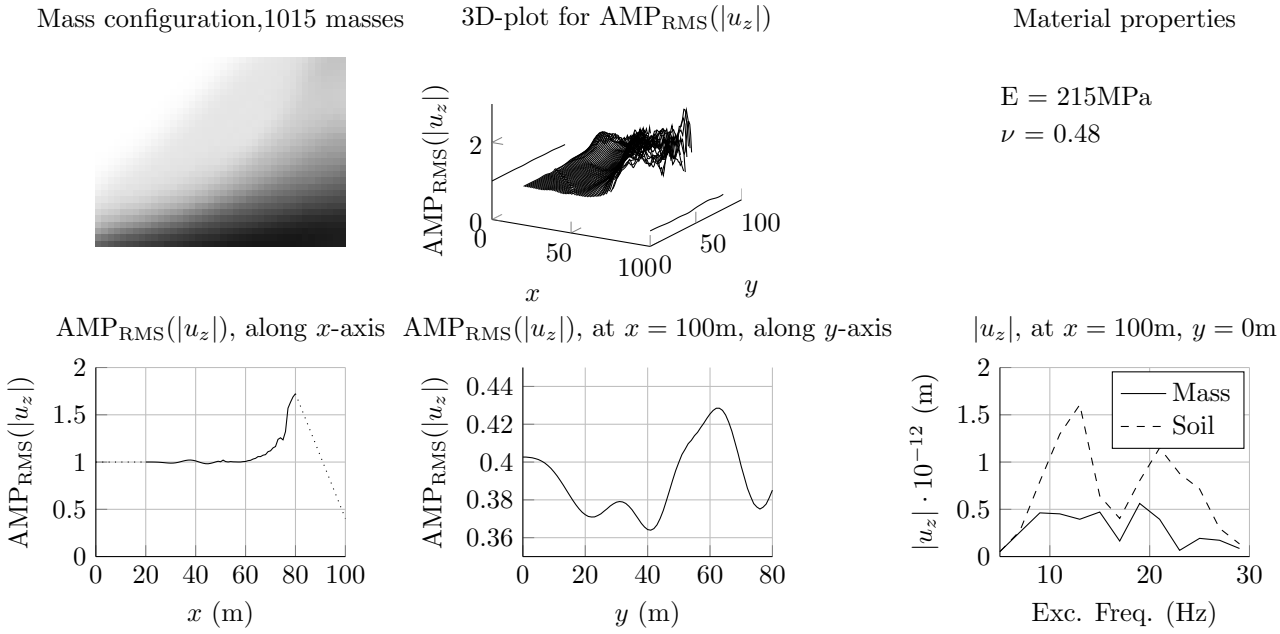

Figure A.28: *3D results for free-8, mirror along line parallel to x-axis of free-1. (Top left) Organization of masses. (Top middle) 3D-plot of RMS amplification of vertical displacement magnitude. (Top right) Mass properties. (Bottom left) RMS amplificiation of vertical displacement magnitude along x-axis. (Bottom middle) RMS amplificiation of vertical displacement magnitude along y-axis, 100 meters from the load application point. (Bottom right) Vertical displacement magnitude response at $x = 100m$, $y = 0m$.*

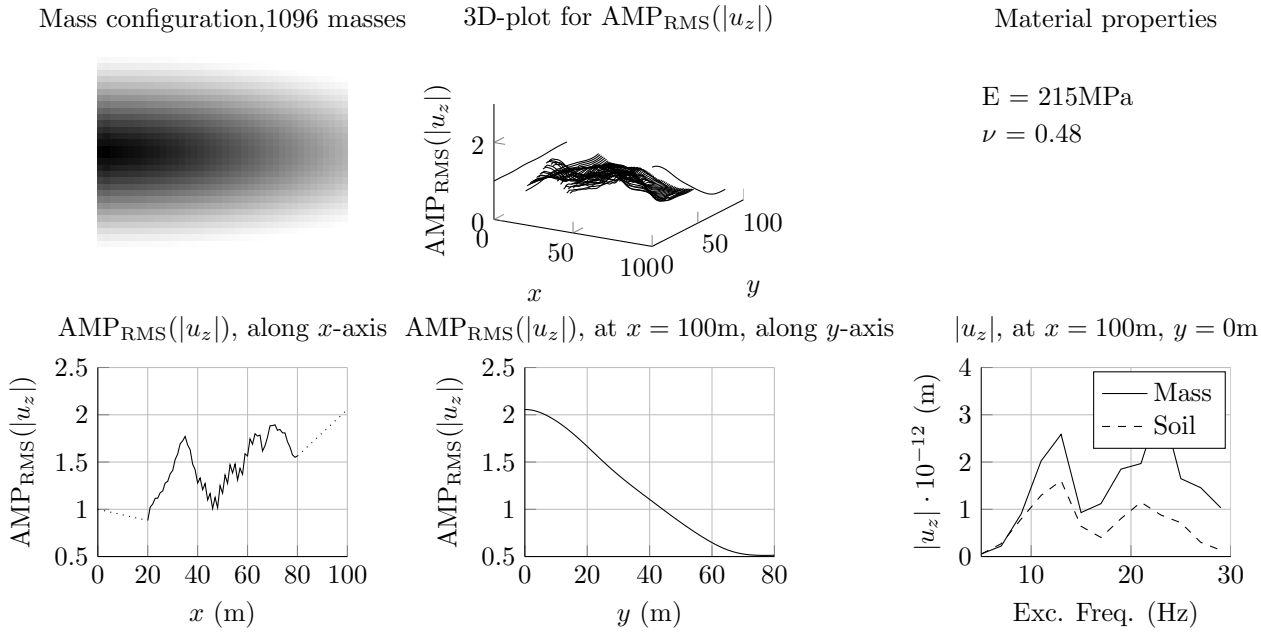

Figure A.29: *3D results for free-15. (Top left) Organization of masses. (Top middle) 3D-plot of RMS amplification of vertical displacement magnitude. (Top right) Mass properties. (Bottom left) RMS amplificiation of vertical displacement magnitude along x-axis. (Bottom middle) RMS amplificiation of vertical displacement magnitude along y-axis, 100 meters from the load application point. (Bottom right) Vertical displacement magnitude response at $x = 100m$, $y = 0m$.*

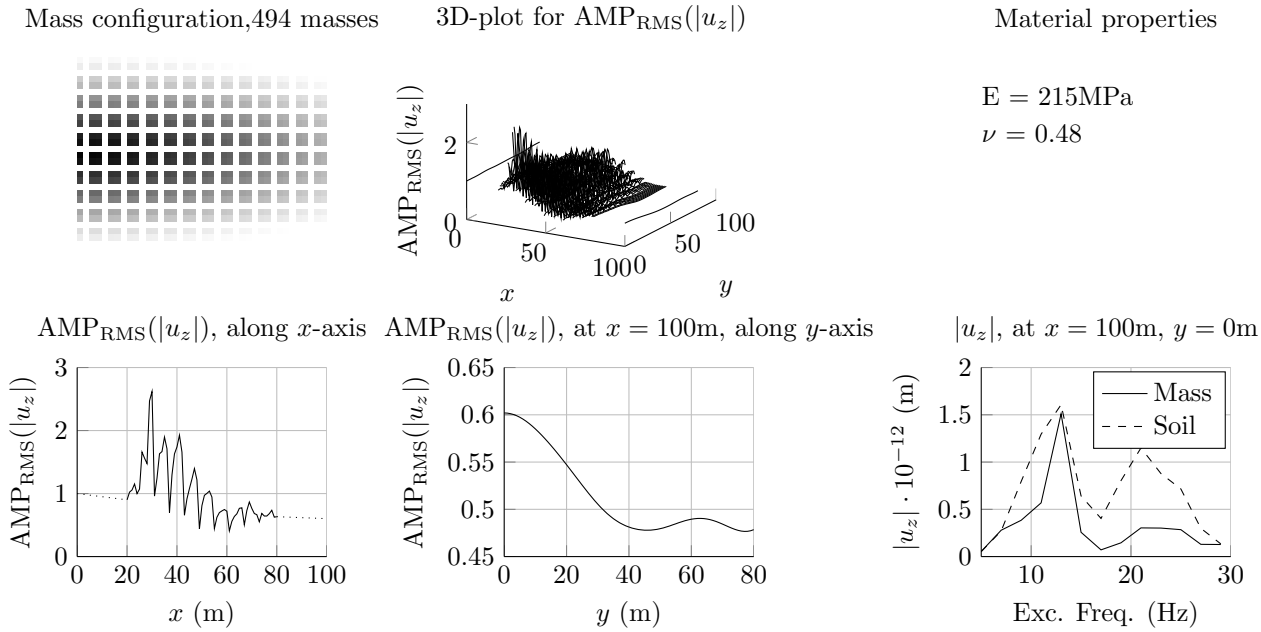

Figure A.30: *3D results for free-17, discrete version of free-15. (Top left) Organization of masses. (Top middle) 3D-plot of RMS amplification of vertical displacement magnitude. (Top right) Mass properties. (Bottom left) RMS amplificiation of vertical displacement magnitude along x-axis. (Bottom middle) RMS amplificiation of vertical displacement magnitude along y-axis, 100 meters from the load application point. (Bottom right) Vertical displacement magnitude response at $x = 100m$, $y = 0m$.*

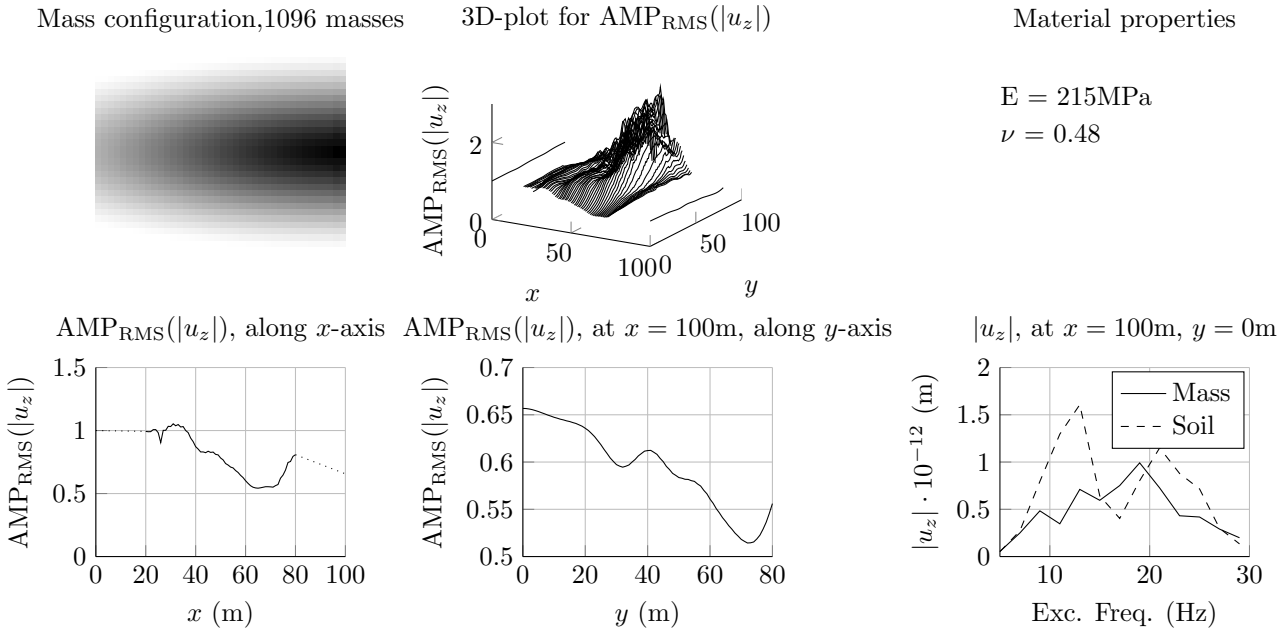

Figure A.31: *3D results for free-18, mirror along line parallel to y-axis of free-15. (Top left) Organization of masses. (Top middle) 3D-plot of RMS amplification of vertical displacement magnitude. (Top right) Mass properties. (Bottom left) RMS amplificiation of vertical displacement magnitude along x-axis. (Bottom middle) RMS amplificiation of vertical displacement magnitude along y-axis, 100 meters from the load application point. (Bottom right) Vertical displacement magnitude response at* $x = 100m$, $y = 0m$.

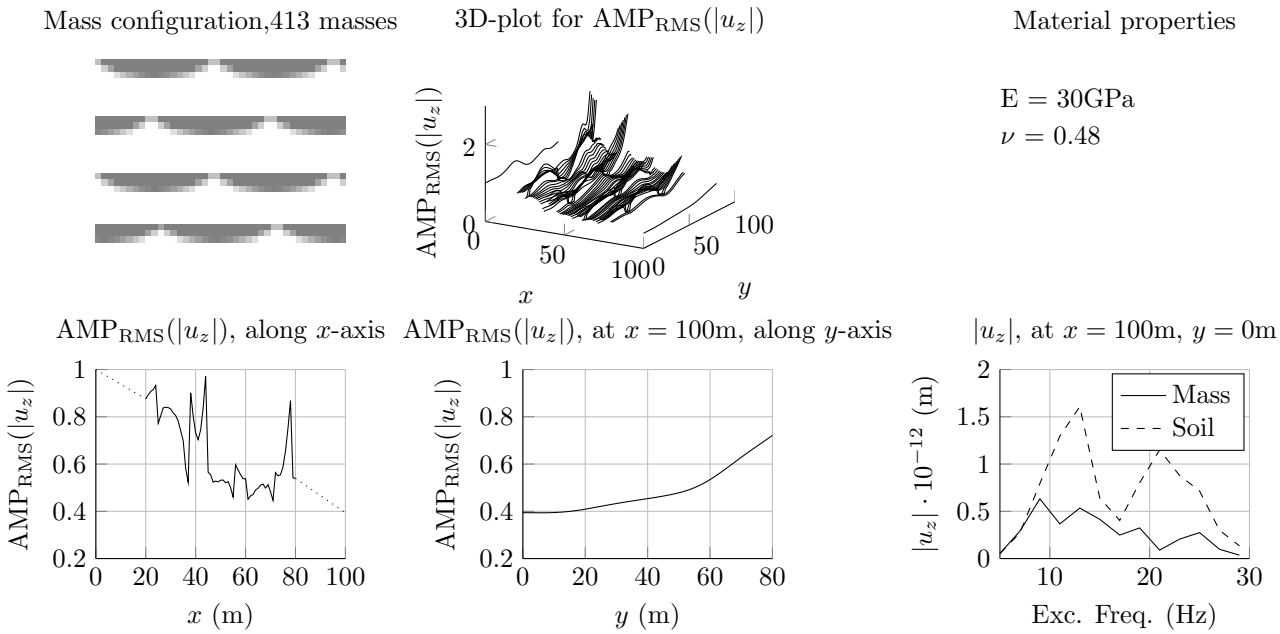

Figure A.32: *3D results for free-19. (Top left) Organization of masses. (Top middle) 3D-plot of RMS amplification of vertical displacement magnitude. (Top right) Mass properties. (Bottom left) RMS amplificiation of vertical displacement magnitude along x-axis. (Bottom middle) RMS amplificiation of vertical displacement magnitude along y-axis, 100 meters from the load application point. (Bottom right) Vertical displacement magnitude response at* $x = 100m$, $y = 0m$.

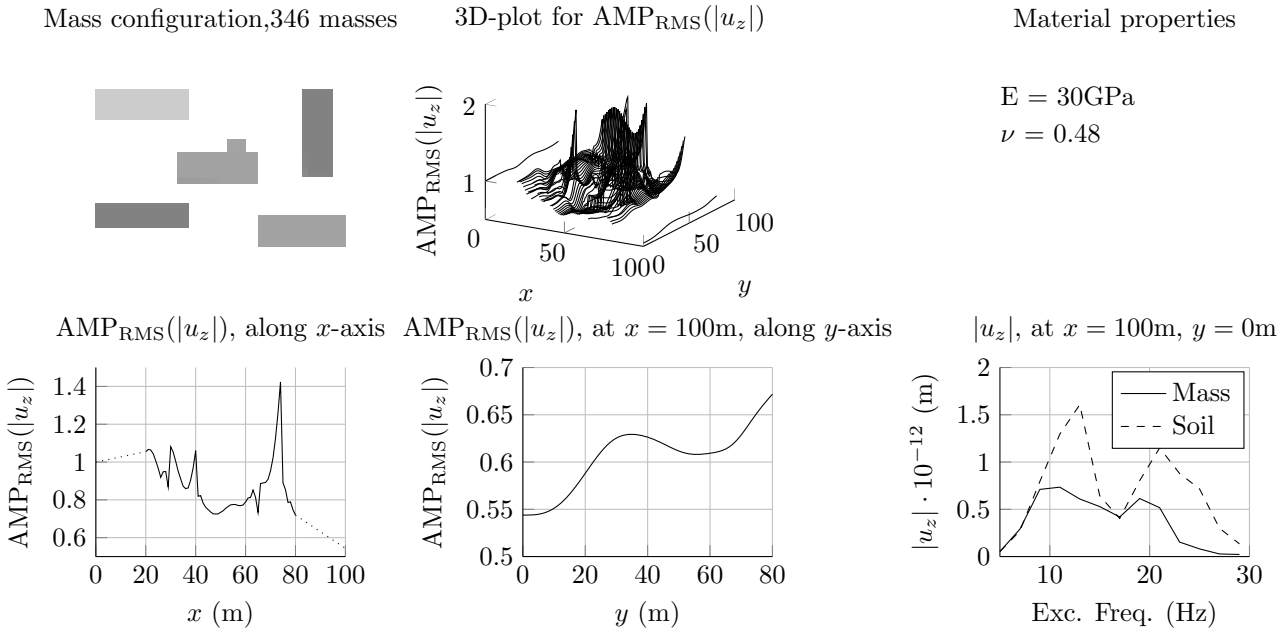

Figure A.33: *3D results for building-1. (Top left) Organization of masses. (Top middle) 3D-plot of RMS amplification of vertical displacement magnitude. (Top right) Mass properties. (Bottom left) RMS amplificiation of vertical displacement magnitude along x-axis. (Bottom middle) RMS amplificiation of vertical displacement magnitude along y-axis, 100 meters from the load application point. (Bottom right) Vertical displacement magnitude response at $x = 100m$, $y = 0m$.*

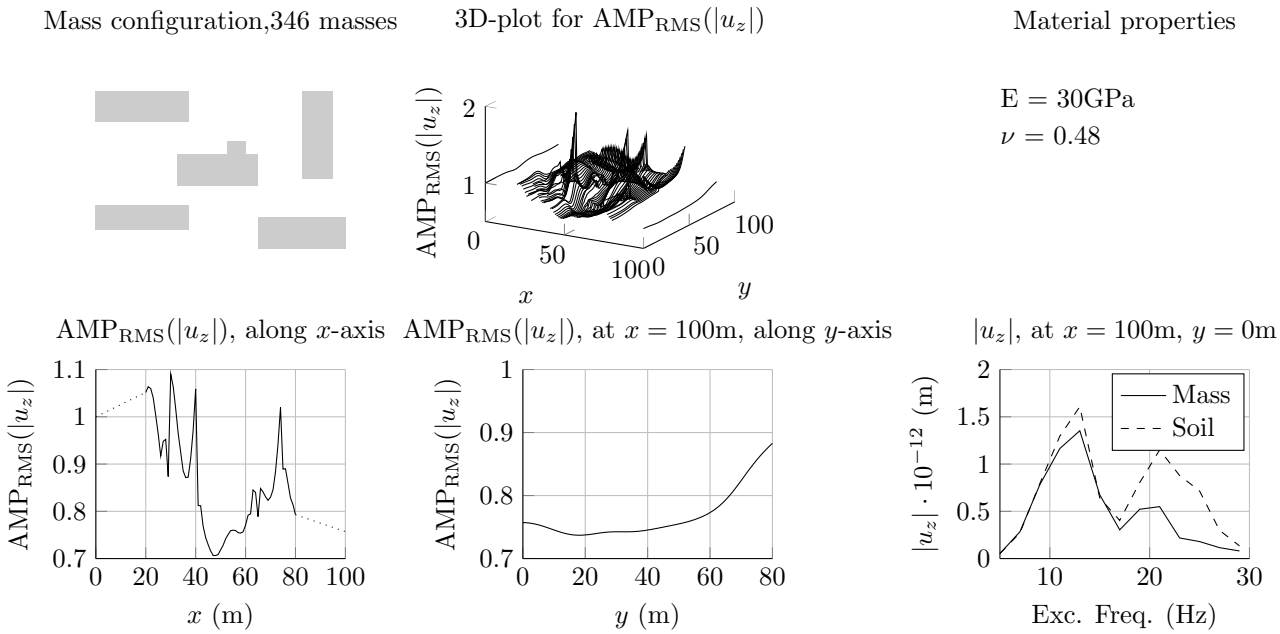

Figure A.34: *3D results for building-2. (Top left) Organization of masses. (Top middle) 3D-plot of RMS amplification of vertical displacement magnitude. (Top right) Mass properties. (Bottom left) RMS amplificiation of vertical displacement magnitude along x-axis. (Bottom middle) RMS amplificiation of vertical displacement magnitude along y-axis, 100 meters from the load application point. (Bottom right) Vertical displacement magnitude response at $x = 100m$, $y = 0m$.*

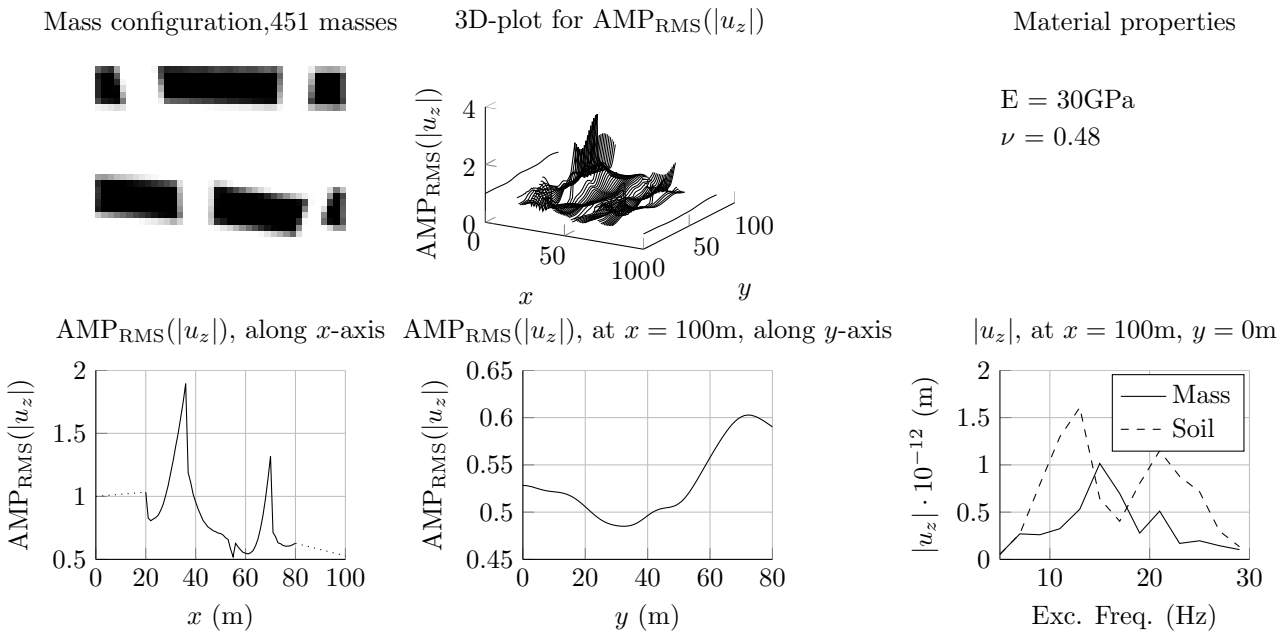

Figure A.35: *3D results for building-3. (Top left) Organization of masses. (Top middle) 3D-plot of RMS amplification of vertical displacement magnitude. (Top right) Mass properties. (Bottom left) RMS amplificiation of vertical displacement magnitude along x-axis. (Bottom middle) RMS amplificiation of vertical displacement magnitude along y-axis, 100 meters from the load application point. (Bottom right) Vertical displacement magnitude response at $x = 100m$, $y = 0m$.*

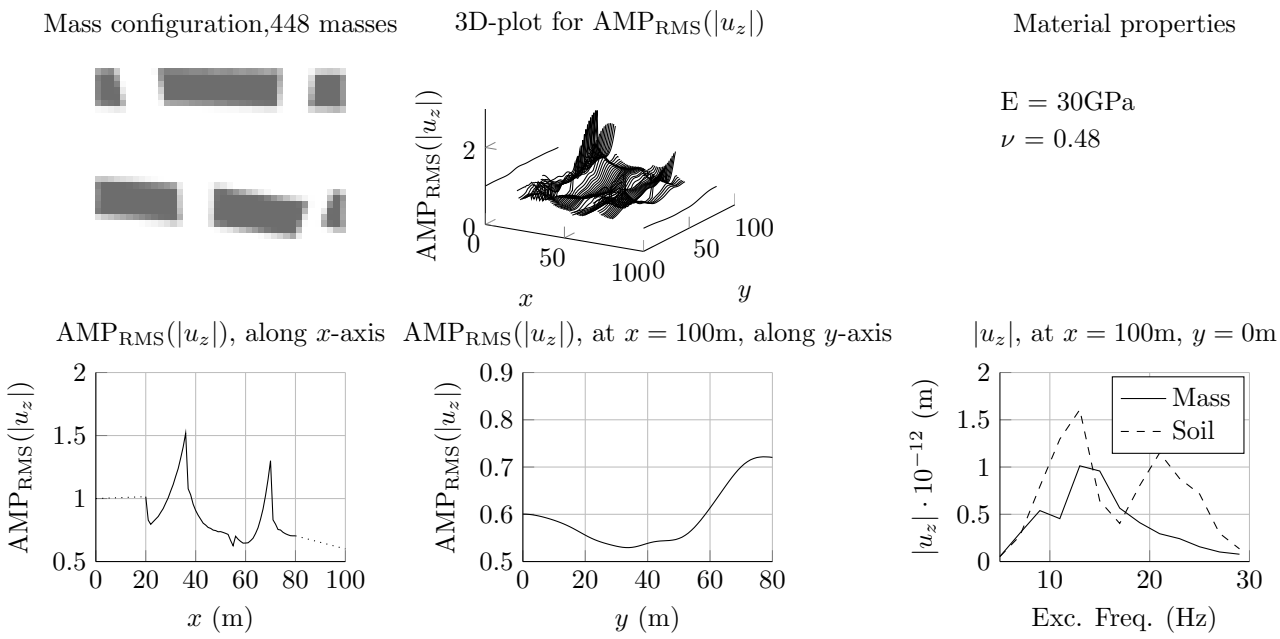

Figure A.36: *3D results for building-5. (Top left) Organization of masses. (Top middle) 3D-plot of RMS amplification of vertical displacement magnitude. (Top right) Mass properties. (Bottom left) RMS amplificiation of vertical displacement magnitude along x-axis. (Bottom middle) RMS amplificiation of vertical displacement magnitude along y-axis, 100 meters from the load application point. (Bottom right) Vertical displacement magnitude response at $x = 100m$, $y = 0m$.*

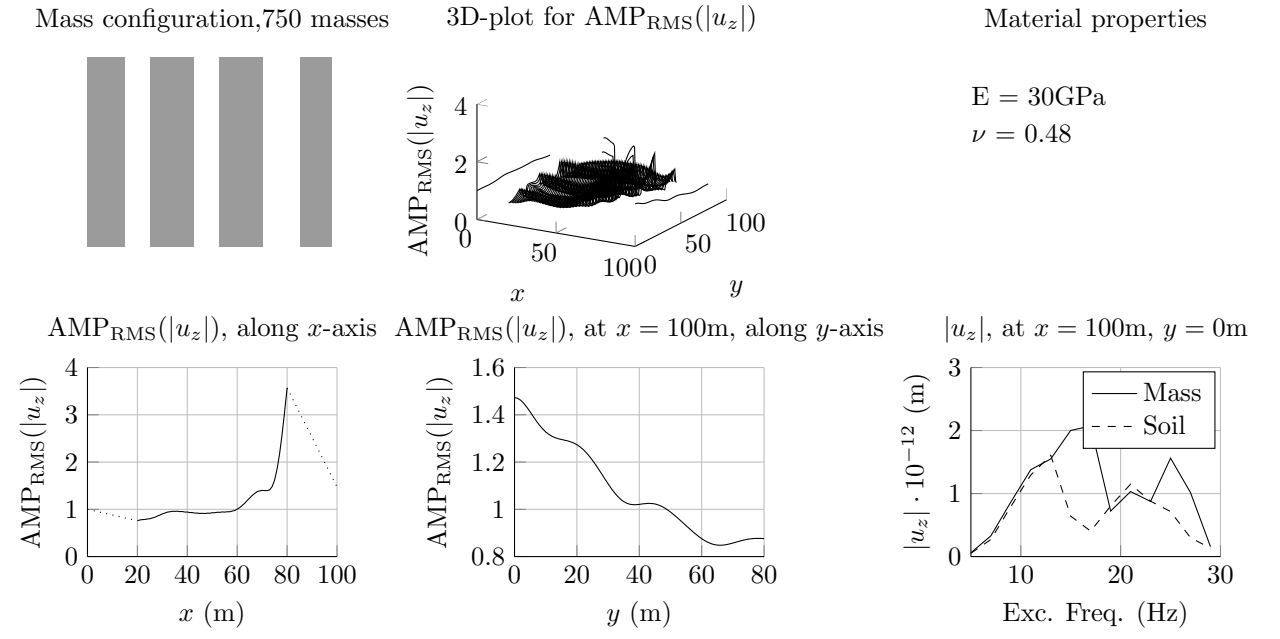

Figure A.37: *3D results for building-7. (Top left) Organization of masses. (Top middle) 3D-plot of RMS amplification of vertical displacement magnitude. (Top right) Mass properties. (Bottom left) RMS amplificiation of vertical displacement magnitude along x-axis. (Bottom middle) RMS amplificiation of vertical displacement magnitude along y-axis, 100 meters from the load application point. (Bottom right) Vertical displacement magnitude response at $x = 100m$, $y = 0m$.*